Sede Amministrativa: Università degli Studi di Padova
Dipartimento di Fisica ed Astronomia "Galileo Galilei"

DOTTORATO DI RICERCA IN FISICA
CICLO XXV

Thermal Characterization of Helical States in RFX-mod with Fast Soft X-Rays Diagnostics

Direttore della scuola: Ch.mo Prof. Andrea Vitturi

Supervisore: Ch.mo Prof. Piero Martin

Co-supervisori: Dott. Paolo Franz

Dott. Marco Gobbin

Dottorando: Alberto Ruzzon

31 Gennaio 2013

Contents

Abstract

In this thesis I describe the work carried on in my three years of PhD course at the Physics Department of the Università degli Studi di Padova. Most of the work presented here has been performed at the Consorzio RFX (Padua). Consorzio houses the RFX-mod experiment (Reversed Field eXperiment), which is the largest toroidal device to study magnetically confined plasmas in the so-called Reversed Field Pinch (RFP) configuration.

The RFP is one of the three main configurations presently used to confine plasmas toroidally. The other two are: the *tokamak*, the most diffused and promising configuration, now adopted in the ITER experiment (at the moment under construction near Marseille), and the *stellarator*, whose most advanced experiment is W7X, under construction in Greifswald. The main purpose of these devices is the study of the conditions that are requested for an energy efficient controlled fusion.

Nuclear fusion has been studied for a long time in various forms since it has been conceived as one of the most interesting alternatives to the traditional sources for energy production. In order to achieve the conditions for an efficient energy production, magnetically confined plasmas have to be sufficiently dense and hot and they must be confined for long intervals. Consequently, the understanding of energy and particle losses is mandatory.

RFP configuration is intrinsically linked to the presence of the magnetic chaos and this makes it naturally prone to energy losses; thanks to operations at high plasma current (the details will be presented in the thesis) new regimes are achieved and the chaos mitigated. The magnetic configurations of these new regimes (briefly called here *helical*) was studied in depth in the past thanks to the powerful system for active control of MHD stability installed in RFX-mod and based on 192 active coils, each independently driven and feedback controlled. Moreover, thermal diagnostics have allowed the detailed study of energy transport features. On the other hand dynamic behavior of *helical* regime have still to be investigated and this is the principal aim of this work.

In order to obtain informations on the dynamics of *helical* regimes fast thermal diagnostics have been developed; such diagnostics are based on the detection of soft x-ray emissions from the plasma. My research activity has been focused on developing new method to elaborate the data coming from these diagnostics and on

analyzing them.

In particular, I was involved in the development of a new tomographic algorithm, devoted to the reconstruction of the plasma emissivity during *helical* transitions. As *helical* regimes give a different magnetic structure when compared to the typical plasma configurations, the new algorithm estimates emissivity taking into account also the magnetic data and hence the magnetic structure of the plasma. Moreover, I also analyzed the temperatures derived from the SXR diagnostics using the two foil technique. These diagnostics are able to follow the time evolution of the temperature during a single transition to *helical* state thanks to their high sampling rate.

This thesis describes the results obtained analyzing not only the data coming from SXR diagnostics but keeping into account also the magnetic measurements, although this happens indirectly. My research activity can be summarized as follows:
SXR tomography. My personal contribution concerns the developing of a new method to estimate the emissivity of the plasma, especially during the *helical* regimes. Such a new method is based on the hypothesis that the topology of emissivity is strictly connected to the magnetic one. In a schematic way this algorithm utilizes magnetic and emissivity data together.
Two foil diagnostics. The aim of my activity is to analyze temperatures coming from the two foil diagnostics in order to characterize *helical* regimes. The target of the study is to find out the behavior of the temperature in the core of the plasma; in particular I have looked for correlations between the amplitudes of thermal barriers and the magnitudes of magnetic perturbations during *helical* regimes. Two different analysis have been done. In the first, I have performed a statistical analysis on a wide database of raw temperature gradients. In the second a new database has been built up, this time temperature profiles have been modified in order to consider the different magnetic conditions of the plasma.

During the PhD period, I was also involved in the collaboration between Consorzio RFX and the University of Wisconsin, Madison, where the Madison Symmetric Torus (MST) RFP experiment is located. My activity was focused on the development and adaptation of the analysis method realized for RFX-mod devices. In particular, the algorithm devoted to estimate the emissivity profile has been adapted to elaborate the data of a different diagnostic; its output was no more the emissivity of the plasma but its temperature. Finally another algorithm has been developed; it is dedicated to obtain temperature data from the tomography device using a different and simpler method.

The first two chapters give a general overview introducing concepts on the fusion plasma, RFP configuration and of SXR diagnostics in order to help the reader to better understand the context. In particular, chapters are organized as follow:

- *Chapter 1* is a brief introduction to thermonuclear fusion and magnetic confinement approaches. It briefly describes the physics of the magnetically confined plasma and introduces the concept of Reversed Field Pinch configuration, moreover the subject of energy losses is highlighted. The reasons of this work are explained.

- *Chapter 2* describes the Padua experiment called Reversed Field eXperiment. This chapter reports also the characteristics of the SXR diagnostics.

- *Chapter 3* shows how the data coming from the two foil diagnostic have been used to investigate the presence and the dimensions of energy transport barriers inside the plasma. Investigations are focused on the correlation between barriers dimension and plasma magnetic configuration, precisely on the dependence of temperature gradients on the magnitude of the magnetic perturbations.

- In *chapter 4* a method to determine the plasma emissivity, keeping into account its magnetic topology, is developed. It is show how, the knowledge of the magnetic topology improves the interpretation of the temperature profile obtained with two foil diagnostics.

- *chapter 5*. The remapping of the temperature profile and the algorithm to estimate the temperature gradient developed in the previous chapter 4 are used here to investigate the presence and the behavior of thermal transport barriers during the helical regimes. Similarly to the study reported in chapter 3, a database is built up and analyzed. In this case a different and more powerful diagnostic has been used; moreover, the integration with magnetic data improves significantly the temperature profiles.

- *Chapter 6* describes how the algorithm previously developed has been applied to the Madison experiment (MST); in fact, as described in the following, tomography devices of MST and RFX-mod have different features and the algorithm must be adapted. For instance, MST experiment did not have two foil diagnostics for the fast temperature analysis; consequently, the aim of the modified algorithm was changed to the estimation of the temperature profile instead of the emissivity one. Besides the conversion of the algorithm, this chapter develops an alternative method to estimate the temperature profile.

- *Chapter 7* closes the work summarizing the previous results and drawing the conclusions.

Prefazione

In questa tesi descrivo il lavoro sviluppato nell'arco dei tre anni di attività di dottorato al dipartimento di Fisica dell'Università degli studi di Padova. Il seguente lavoro è stato eseguito presso il Consorzio RFX (sempre a Padova) dove ha sede l'esperimento RFX (esperimento a campo rovesciato), che è attualmente la più grande macchina per lo studio dei plasmi in configurazione toroidale di tipo Reversed Field Pinch (RFP).

L'RFP è una delle tre principali configurazioni adottate per il confinamento del plasma in geometria toroidale, le altre due sono il *tokamak* e lo *stellarator*. Tra le tre, il *tokamak* è attualmente considerata la più promettente, tanto da essere impiegata nel più grande e costoso esperimento per plasmi toroidali: ITER (International Thermonuclear Experimental Reactor), in costruzione vicino a Marsiglia. Tuttavia anche lo *stellarator* sta avendo interessanti sviluppi con la costruzione di W7X a Greifswald. Il principale interesse di questi tre tipi di esperimenti è lo studio delle condizioni per ottenere la fusione nucleare controllata.

La fusione nucleare è stata studiata a lungo con vari interessi, compreso quello di fonte energetica alternativa. Per arrivare a realizzare una produzione energetica efficiente basata sulla fusione, nel caso dei plasmi confinati magneticamente, è importante che questi siano sufficientemente densi, caldi e sostenuti per periodi lunghi. Un ruolo chiave è pertanto assegnato alla riduzione delle perdite di energia e quindi al loro studio.

L'RFP risulta è soggetto a perdite energetiche relativamente elevate essendo il caos magnetico spesso fondamentale per il sostentamento della configurazione; tuttavia, durante le operazioni ad alta corrente, nuovi regimi con caos mitigato sono ottenibili (per semplicità chiamati *elicoidali*, maggiori dettagli sono riportati nel seguito della tesi). Grazie al sistema di controllo dei modi MHD del plasma in feedback mediante bobine magnetiche implementato in RFX, molti dettagli di questi regimi sono stati già ottenuti. Altri studi hanno permesso di individuare anche le loro caratteristiche termiche, tuttavia la loro dinamica rimane sconosciuta e costituisce l'argomento principale del mio lavoro.

Per ottenere le informazioni sulla dinamica dei regimi *elicoidali* sono necessarie diagnostiche termiche veloci. Queste sono generalmente basate sul rilevamento di raggi x soffici (SXR) emessi dal plasma. La mia attività di ricerca si è concentrata

sullo sviluppo di nuovi metodi di analisi per questi dati.

In particolare, sono stato coinvolto nello sviluppo di un algoritmo per una nuova tecnica tomografica dedicata alla ricostruzione della emissività del plasma durante gli stati *elicoidali*. Questa tecnica deve tenere conto che il plasma in questi regimi ha una diversa topologia rispetto alle configurazioni classiche. Per fare ciò l'algoritmo tiene conto anche dei dati magnetici da cui viene dedotta la topologia del plasma.

Un'altra parte dell'attività si è concentrata sull'analisi delle temperature stimate con le diagnostiche SXR a doppio filtro. Tali diagnostiche, grazie alla loro alta banda passante di campionamento, sono capaci di seguire l'evoluzione della temperatura durante le transizioni del plasma agli stati *elicoidali*.

Questa tesi descrive i risultati ottenuti analizzando non solo i dati provenienti dalle diagnostiche SXR ma anche prendendo in considerazione le misure magnetiche. L'attività può essere riassunta in questa maniera:
Tomografia SXR. Il mio lavoro ha riguardato lo sviluppo di un nuovo metodo per stimare l'emissività del plasma, specialmente durante i regimi *elicoidali*. Questo nuovo metodo si basa sull'ipotesi che la topologia dell'emissività sia sovrapponibile a quella magnetica. In sintesi l'algoritmo sviluppato usa i dati magnetici e quelli di emissività assieme.
Diagnostiche doppio filtro. Lo scopo di questa attività è l'analisi delle temperature provenienti dalle diagnostiche a doppio filtro per individuare il comportamento termico all'interno del plasma. In particolare ho cercato le possibili correlazioni tra i modi magnetici e l'ampiezza delle barriere di trasporto termico. Sono state fatte due analisi distinte. La prima è un'analisi statistica su un ampio database di dati grezzi sui gradienti. La seconda si basa su un nuovo database e su una nuova stima del gradiente, questa volta tenendo conto delle condizioni magnetiche del plasma.

Durante l'attività di dottorato sono stato coinvolto in un progetto di collaborazione tra il Consorzio RFX e la University of Wisconsin, Madison, dove è situato l'esperimento Madison Simmetric Torus (MST). La mia attività, in questa circostanza, è stata l'adattamento e lo sviluppo ulteriore degli algoritmi sviluppati per RFX. L'algoritmo dedicato alla ricostruzione della emissività del plasma è stato adattato alle diagnostiche di MST; l'adattamento ha consentito, inoltre, che il suo output sia stato evoluto dall'emissività alla temperatura. In aggiunta, è stato ideato un altro algoritmo, il cui scopo è quello di stimare la temperatura del plasma con un approccio più semplice.

I capitoli sono organizzati come segue:

- Il *capitolo 1* introduce la fusione nucleare mediante confinamento magnetico di plasmi. Si descrivono i concetti fisici alla base della configurazione RFP dando, inoltre, una panoramica sulle sue caratteristiche nel trasporto energetico. Infine, si spiegano le motivazioni di questo lavoro di tesi.

- Nel *capitolo 2* viene descritto l'esperimento RFX di Padova. Quindi vengono illustrate le caratteristiche delle diagnostiche SXR impiegate nelle analisi successive.

- Il *capitolo 3* mostra come i dati ottenuti dalla diagnostica a doppio filtro sono stati usati per indagare la presenza e le dimensioni di barriere di trasporto energetico all'interno del plasma. Le indagini si sono concentrate sulle correlazioni tra la dimensione delle barriere e la configurazione magnetica e più precisamente sulla dipendenza del gradiente di temperatura dall'ampiezza delle perturbazioni magnetiche.

- Nel *capitolo 4* è sviluppato un algoritmo per determinare l'emissività del plasma considerando anche la topologia magnetica. Inoltre, la topologia magnetica viene sfruttata per migliorare la ricostruzione del profio di temperatura, dedotto dalle diagnostiche SXR a doppio filtro, e viene studiato un metodo per stimarne il massimo gradiente.

- Nel *capitolo 5* vengono descritte le analisi di un database costruito con i gradienti di temperatura dedotti col metodo sviluppato nel precedente captiolo. Da questo database è dedotto il comportamento delle barriere di trasporto termico durante i regimi QSH. In questa analisi, rispetto a quella riportata nel capitolo *capitolo 3*, è stata usata una diagnostica più performante i cui dati, in aggiunta, sono stati elaborati con una tecnica più evoluta.

- Il *capitolo 6* illustra l'attività svolta a Madison. Questa riguarda l'adattamento degli algoritmi sviluppati per RFX, tenendo conto delle caratteristiche dell'esperimento e delle diagnostiche di MST. In particolare, MST manca di una diagnostica SXR a doppio filtro per lo studio della dinamica del plasma, pertanto l'algoritmo per la ricostruzione della emissività del plasma, sviluppato nel capitolo 4, è stato modificato per stimarne la temperatura. Oltre a questa conversione, un nuovo algoritmo è stato sviluppato il quale permette il calcolo della temperatura dai dati della tomografia SXR in una maniera più diretta.

- Nel *capitolo 7* vengono tirate le conclusioni del lavoro svolto.

CHAPTER 1

An introduction to plasma physics in nuclear fusion

This introductory chapter gives an overview of nuclear fusion, explains magnetically confined toroidal plasma and its basic concepts for confinement. It introduces the concept of Reversed Field Pinch configuration in toroidal geometry highlighting also the features of heat transport. The concepts discussed here constitute the motivation of my study whose outline is given at the end of the chapter.

1.1 Nuclear fusion and plasmas

Nuclear fusion is the process occurring in the core of the stars and it is able to produce a large amount of power for very long periods. The challenge that has involved a lot of scientists for several years has been to reproduce this process on the earth under controlled conditions and has begun with the 1958 Geneva Conference "Atoms for peace". The purpose is to find a new source of energy: in fact, conventional energy sources, based on fossils, have a lot of disadvantages, such as involvement in political crises and pollution. On the other hand, nuclear fission has security problems, overall for the radioactive scoria storage.

in particular the most easily obtainable fusion reaction, hence the one believed to be feasible in laboratory, is based on two isotopes of hydrogen, i.e. deuterium and tritium. Their reaction is:

$$\begin{array}{ccccccccc} {}^{3}_{1}\mathrm{D} & + & {}^{3}_{1}\mathrm{T} & \Longrightarrow & {}^{4}_{2}\mathrm{He} & + & \mathrm{n} & & \\ & & & & 3.5\mathrm{MeV} & + & 14.1\mathrm{MeV} & = & 17.6\mathrm{MeV} \end{array} \tag{1.1}$$

The mass defect of the products is converted into energy responding to Einstein law $E = m \cdot c^2$. Also the fission reaction exploits the same principle but in this case the fissile heavy nuclei (Uranium) release energy when they are split (the fusion reaction is sketched in figure 1.1). Various solutions were proposed to get a con-

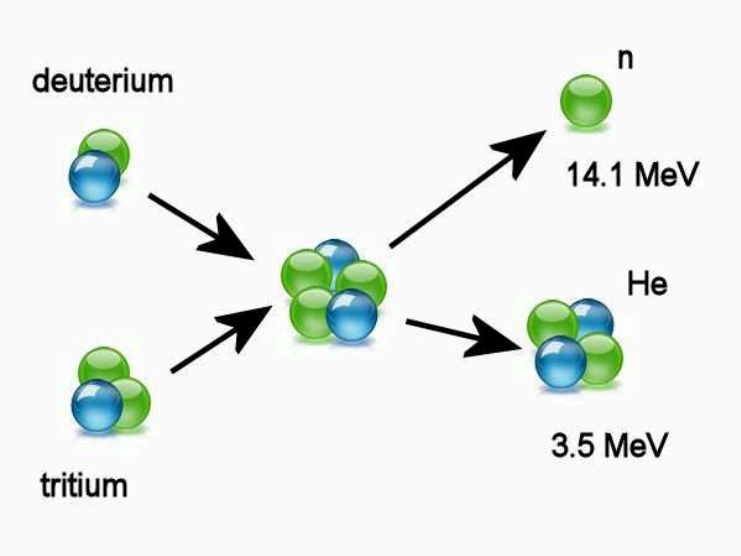

Figure 1.1: Scheme of the fusion reaction between Deuterium and Tritium.

trolled fusion reaction and the most promising is to exploit the thermal energy of the particles itself. In fact, two nuclei can fuse together if they are brought sufficiently close for the short-range attractive nuclear force to overcome the Coulomb repulsion among them. This is possible if the two reactants collide with high enough kinetic energy, which means at high temperatures. In these conditions atoms are ionized and a gas of charged particles is created. High energy charged particles can be confined by strong magnetic fields. Natural examples of ionized gases in magnetic fields are the Sun's photosphere or the Earth's ionosphere. The ionized gases of these example are called *plasmas*, which is considered to be the fourth state of matter.

More generally plasma can be defined as a collection of a large number of charged particles which on a certain scale is called Debye length (defined in the following) quasi neutral. It behaves in a very different way from a neutral gas, in fact the interactions in a plasma are governed by the Coulomb potential, which falls off with the inverse of distance ($V(r) \approx 1/r$).

In absence of a magnetic field, collisions in a plasma are mainly due to the Coulomb force which has a cross-section given by:

$$\sigma_{coul} \approx \frac{e^4}{4\pi\epsilon_0^2 m_e^2 \mathbf{v_0}^4} \tag{1.2}$$

where $\mathbf{v}_0$ is the velocity of an incident electron for a deviation angle $\pi/2$ [1]. Consequently, the mean free path is given by:

$$\mathrm{l_{mfp}} = \frac{1}{n\sigma} \propto \frac{T^2}{ne^4} \tag{1.3}$$

in which it has been considered that the temperature is proportional to the mean kinetic energy. The mean free path is proportional to the square of the temperature. The frequency of collisions (ν_c) is given by the ratio between the thermal energy and the mean free path and thus it is equal to:

$$\nu_c = \frac{v_{th}}{\lambda_{mfp}} \approx \frac{ne^4}{m_e^{1/2} T^{3/2}} \tag{1.4}$$

Therefore, collisions frequency decreases with the temperature, namely with $T^{-3/2}$ [2]; also other basic plasma quantities related to the collision frequency show the same dependence. The main consequence is that if the plasmas has a high temperature (for instance $T \gtrsim 1$keV, some examples are: all main astrophysical plasmas, solar photosphere, Earth's ionosphere, laboratory plasmas, laser-plasmas, etc.) collisions are almost negligible, namely the time associated with collisions is the largest of all characteristic times. Moreover, since diffusion is inversely proportional to collisions, and thus proportional to the temperature, hot plasmas are able to cancel temperature and density inhomogeneities rapidly (if the plasmas is magnetized this is true only in the direction parallel to the magnetic field).

Coulomb force and its long-range interaction implies the presence of collective oscillations in the plasma; its frequency, called *electron plasma frequency* ($\omega = \omega_{pe}$), is given by:

$$\omega_{pe}^2 = \frac{ne^2}{\epsilon_0 m_e} \tag{1.5}$$

(a simple derivation can be found in [3]). These oscillations can be considered as a global behavior that is induced by perturbations in the charge density. In most cases, the ratio between collision and plasma frequency is very small:

$$\frac{\nu_c^2}{\omega_{pe}^2} \approx \frac{ne^6}{t^3} \ll 1 \tag{1.6}$$

Another issue deriving from a long-range interaction is that the Coulomb potential at small distances is screened as:

$$V(r) = q \cdot \frac{e^{-r/\lambda_D}}{r} \tag{1.7}$$

Collective motions are the origins of this result, as discussed in detail in [4]. λ_D is called Debye length and it defines the maximum distance for independent electron motion (i.e. the possibility of each electron to move independently from the others). At distance further than λ_D (Debye sphere) collective effects take place and electron motions can be considered coupled. Debye length is defined as the ratio between individual velocity and collective frequency:

$$\lambda_D = \frac{v_{th}}{\omega_{pe}} \approx \frac{T^{1/2}}{n^{1/2} e} \tag{1.8}$$

Plasma type	n m^{-3}	T eV	B tesla	a m	λ_D m	ℓ_{mfp} m	ω_{pe} s^{-1}	ν_c s^{-1}	g
inter-stellar gas	10^6	1		10^{19}	7	$4 \cdot 10^9$	$6 \cdot 10^4$	10^{-4}	$2 \cdot 10^{-9}$
solar wind	10^7	10	10^{-8}	10^{11}	10	$7 \cdot 10^9$	10^5	10^{-4}	10^{-9}
solar corona	10^{12}	10^2	10^{-2}	10^7	$7 \cdot 10^{-2}$	$4 \cdot 10^7$	$6 \cdot 10^7$	10^{-1}	$2 \cdot 10^{-9}$
solar core	10^{32}	10^3		$7 \cdot 10^8$	$3 \cdot 10^{-11}$	$6 \cdot 10^{-11}$	$6 \cdot 10^{17}$	$3 \cdot 10^{17}$	0.5
thermo-nuclear plasma	10^{21}	10^4	10	10	$2 \cdot 10^{-5}$	$4 \cdot 10^2$	$2 \cdot 10^{12}$	10^5	$5 \cdot 10^{-8}$

Table 1.1: Characteristic parametrs for different types of plasmas: a is the system size. Parameters of the solar wind are taken at one astronomical unit from the sun.

If physical constants are inserted and temperature is expressed in electronvolts, the definition 1.8 becomes [5]:

$$\lambda_D = 7430 \sqrt{\frac{T[\text{eV}]}{n[\text{m}^{-3}]}} \tag{1.9}$$

In thermonuclear plasmas λ_D is in the order of tenth of micrometers, and thus the ratio between mean free path and Debye length is very large:

$$\frac{\lambda_{mfp}}{\lambda_D} = \frac{\omega_{pe}}{\nu_c} \tag{1.10}$$

Consequently, dynamical effects are faster than relaxation effects, and the screening distance smaller than the mean free path. This leads to the definition of the following quantity, which represents the inverse of the number of particles in the Debye sphere:

$$g = \frac{\nu_c}{\omega_{pe}} = \frac{n^{1/2} e^3}{T^{3/2}} = \frac{1}{n\lambda_D^3} \tag{1.11}$$

In most cases of interest (see table 1.1) g is very small keeping the system quite easy to study: in weakly coupled plasmas, g becomes an ordering parameter for all relevant scales and, when g is small, the scaling relation sketched in figure 1.2 holds. The same hierarchy is resumed as follows: $r_0 \sim e^2/4\pi\epsilon_0 T < r_n \sim n^{-1/3} < \lambda_D < \lambda_{mfp} < a$.

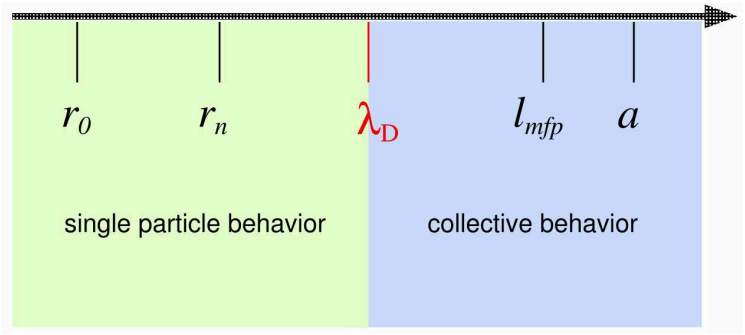

Figure 1.2: Ordering of the main plasma parameters for a weakly coupled plasma.

1.2 Burning criteria for a thermo nuclear plasma

The most easily obtainable reaction in a laboratory is the one between D and T reported in equation 1.1. From figure 1.3 we see that the D-T cross section reaches a maximum for temperatures of the order of 80keV. Nevertheless, the optimal temperature of fusing nuclei is of $\sim$ 10keV because of the alpha production rate and stability limits. In fact the power given by alpha particles (which are confined by magnetic fields) can be great enough to sustain the reaction, with no external heating. The alpha production rate is given by:

$$\frac{\partial n_\alpha}{\partial t} = n_D n_T \langle \sigma_F v \rangle \tag{1.12}$$

where n_D and n_T are the deuterium and tritium densities, $\langle \sigma_F v \rangle$ is the fusion reaction rate, averaged over some velocity distribution (maxwellian in general). Assuming that the densities of the two hydrogen isotopes are the same, the power on the alpha particles is proportional to the energy released in every single fusion reaction, $\mathscr{E}_\alpha$ (3.5 MeV as stated in equation 1.1) through:

$$P_\alpha = \frac{1}{4} n^2 \langle \sigma_F v \rangle \mathscr{E}_\alpha \tag{1.13}$$

We will introduce now a fundamental parameter in nuclear fusion: we define

$$\beta = \frac{p}{B^2/2\mu_0} = \frac{2nT}{B^2/2\mu_0} \tag{1.14}$$

as the ratio between kinetic and magnetic pressure [5]. For MHD stability requirements [6] the value of β cannot exceed a few percent. Besides, there is a technological limitation on the applied magnetic field. As a consequence, introducing β in equation 1.13 we obtain:

$$P_\alpha = \left(\frac{1}{8\mu_0}\right)^2 \beta^2 B^4 \left[\frac{\langle \sigma_F v \rangle}{T^2}\right] \tag{1.15}$$

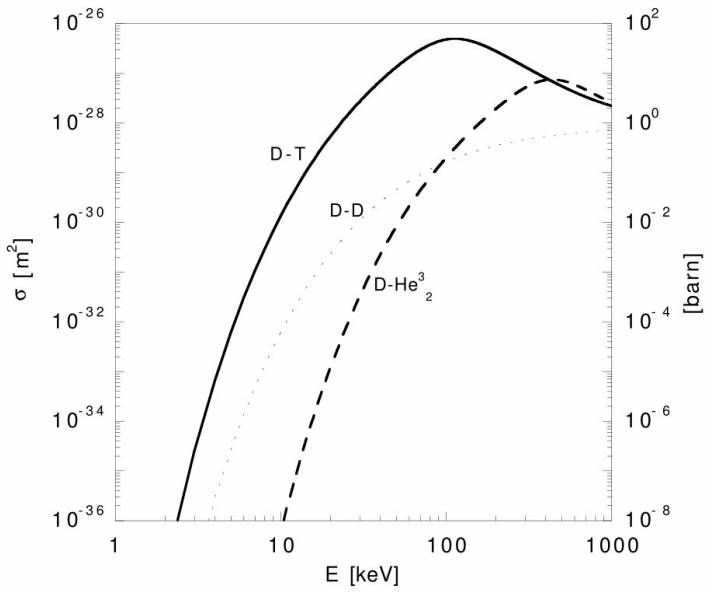

Figure 1.3: Cross section of fusion reactions as a function of the relative kinetic energy. Reactants are labeled as: D=Deuterium, T=Tritium and He^3_2=Helium isotope with three nucleons.

We can see that in the right-hand side the term in square brackets is a function of temperature only. Since $\langle\sigma_F v\rangle \sim T^2$ for temperatures between 8 and 18keV, P_α has a pronounced, flat maximum around 10keV. In a fusion reactor the balance between heating and losses is given by:

$$\frac{\partial W}{\partial t} = P_{heat} + P_\alpha - P_{loss} \tag{1.16}$$

where $W \sim 3nT$ is the plasma energy density. In the absence of heating, there will be an approximately exponential decay of energy, $\partial W/\partial t = -W/\tau_E$, where τ_E is an empirical, energy half life time, known as energy confinement time. We want to underline that this is an empirical definition, given completely unaware of the rather complex physical processes governing heat and particle transport in a plasma. Ignition ($P_\alpha > P_{loss}$) requires:

$$\frac{1}{4}n^2\langle\sigma_F v\rangle\mathscr{E}_\alpha > \frac{3nT}{\tau_E} \rightarrow n\tau_E > \frac{12T}{\mathscr{E}_\alpha}\frac{1}{\langle\sigma_F v\rangle} \tag{1.17}$$

The product $n\tau_E$ must consequently be greater than a quantity which is a function of the temperature only. This relation is known as the ignition criterion [5], and fixes a limit for self-sustained reactors. A plot of the required $n\tau_E$ against T is shown in figure 1.4. It has a minimum value close to 20keV and the requirement for ignition at this temperature is

$$n\tau_E > 1.5 \cdot 10^{20}\mathrm{m}^{-3}\mathrm{s} \tag{1.18}$$

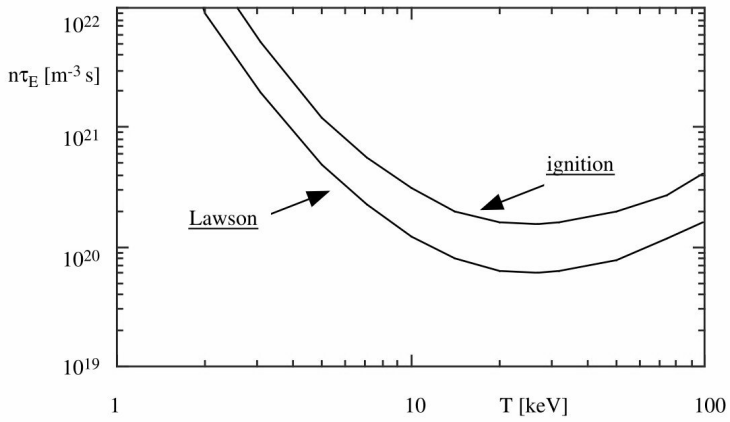

Figure 1.4: $n\tau_e$ as a function of temperature T. Higher curve shows the dependence at the ignition condition, lower one reports the Lawson condition.

In figure 1.4 the lower curve refers to a necessary criterion for reaction sustainment, known as Lawson's criterion, which assumes a constant heating (P_{heat})with an efficiency of 1/3. Since in real reactors alpha particles would probably compensate losses at a substantially lower rate, Lawson's criterion is important merely from a historical point of view; it was thanks to it that the feasibility of a fusion reactor could be proved. The parabolic behavior of figure 1.4 is obtained because at high temperatures losses increase (linearly with temperature) more than fusion processes, while the latter are rare at low temperatures. Since in equation 1.17, $\langle\sigma_F v\rangle/T^2$ is nearly constant for temperatures between 8 and 18keV, an useful way to summarize all these considerations is to use the so-called *fusion triple product*, thus yielding:

$$n\tau_E T > 4 \cdot 10^{21} \mathrm{m}^{-3}\mathrm{s\ keV} \tag{1.19}$$

This requirement is tighter than one could expect at a first glance: if temperature is in the range of 8÷18 keV, the beta limit fixes the density range around $10^{19}\mathrm{m}^{-3}$, therefore τ_E must be in the range from 1 to 10s. In present most advanced experiments (JET, TFTR, JT-60U, DIII-D) it is possible to obtain separately such values of temperature, density and energy confinement time, but it is still not possible to ignition. Indeed, JET [7] and TFTR [8] have achieved conditions near ignition (see figure 1.5) in the '90s. During the recent years no new records was reached since the experimental purposes have been focused on the physical problems which limit the plasma performances (like ELMs and disruptions) and on the design of future operations in new experiments. A particular attention is pointed to the experiment called ITER (International Thermonuclear Experimental Reactor) that will operate at ignition conditions. Such an experiment is under construction near Marseille, France, and the first plasma is planned in 2020. Other important projects for a the study of thermonuclear fusion are W7-X (Germany) [9] and Ignitor (Italy-Russia) [10].

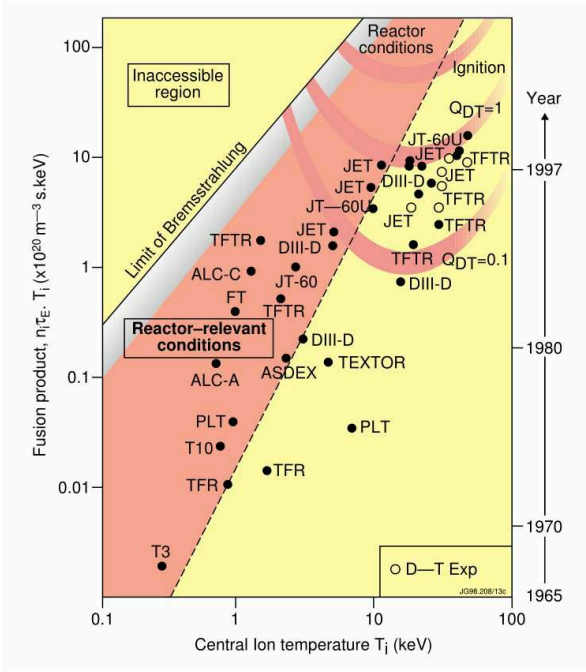

Figure 1.5: Triple product $n\tau_e T$ for the existing Tokamak experiments as a function of the central plasma temperature of the ions. The plot reports also the ignition and the Lawson criterion boundary.

1.3 Magnetic confinement for fusion plasma

Plasma magnetic confinement is based on the properties of charged particle motion in the presence of magnetic fields: due to the Lorentz force, ions and electrons are bent into a circular path by the component of magnetic field perpendicular to the velocity, with a gyration radius defined as the Larmor radius $r_L = mv_\perp/|q|B$ (m is the mass, q the charge and $v_\perp$ the velocity perpendicular to the magnetic field B). Since particles are subject to the effects of the magnetic field only perpendicular to their velocity, in absence of a electric field E, for uniform B, they move along an helical path. Several magnetic field geometries have been investigated to determine the best conditions for plasma confinement, reaching the conclusion that, since particles are free to move along field lines, non-periodic or open magnetic configurations will exhibit poor confinement properties [1, 11]. In linear configurations the losses at the end of the domain are too large to reach the necessary energy confinement; these end losses can be completely avoided in a toroidal system [12].

Such a system can be geometrically described by the set of coordinates (r, θ, ϕ) defined in figure 1.6: r is called the radial coordinate, θ and ϕ are respectively the poloidal and toroidal angles, R_0 and a the major and minor radius of the torus.

In a simple toroidal system with a purely toroidal magnetic field, the magnetic field curvature and gradient produce a vertical drift which is in opposite directions

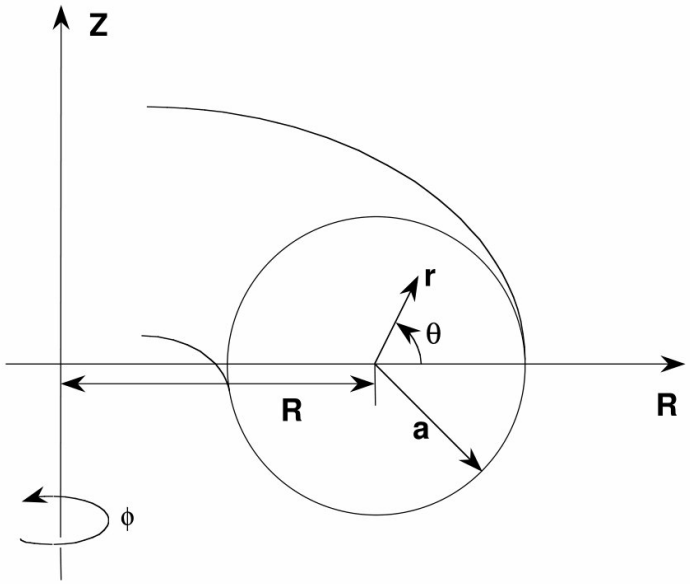

Figure 1.6: Definition of the toroidal coordinates (r,θ,ϕ). Definitions of the experiment parameters R_0 and a are also reported.

for ions and electrons. An electric field is then generated because of the charge separation: such an electric field causes an outward $E \times B$ drift of the whole plasma, and therefore such a simple magnetic field configuration would not be feasible. It is necessary to twist the magnetic field lines by additional magnetic field components; hence, in toroidal experiments there are both a poloidal component B_θ and a toroidal component B_ϕ. The magnetic field can be produced either by external coils or by currents flowing in the plasma, depending on the particular magnetic configuration. Magnetic field lines are thus helixes, which are wound around the torus lying over toroidal surfaces called magnetic surfaces. Helical magnetic field lines are described by the so called safety factor q, which is defined as a function of radius as follows:

$$q(r) = \frac{rB_\phi(r)}{R_0 B_\theta(r)} \tag{1.20}$$

The inverse of this quantity represents the number of poloidal turns done by a helical field per one toroidal turn [13].

1.3.1. MHD model

The theoretical description of a plasma system may be undertaken using different approaches, depending on the level of accuracy required in the description, and on the level of complexity desired in the analysis: one method consists in assuming the plasma as an electrically conducting fluid. This allows the use of the relatively

simple equations of hydrodynamics, adding the effects specific to an electrically charged current-carrying fluid, such as electric and magnetic forces [1].

Let's consider here for simplicity a hydrogen plasma (it would be trivially possible to extend the present description also to multiple species plasmas). Plasma will be considered as a fluid containing positively charged particles (ions) of mass m_i and charge $+e$, distributed with density n_i, and negatively charged ones (electrons), with mass m_e, charge $-e$ and density n_e. We will moreover assume that charge neutrality will be at least approximately satisfied on macroscopic scales, so that $n_i \approx n_e \approx n$. Since we want to describe the plasma as a single neutrally charged fluid, we need to define the mass density $\rho = n_i m_i + n_e m_e \approx n m_i$, the charge density $\sigma = (n_i - n_e)e$, the mass velocity, $\mathbf{u} = (n_i m_i \mathbf{u}_i + n_e m_e \mathbf{u}_e)/\rho \approx \mathbf{u}_i + (m_e/m_i)\mathbf{u}_e$ and the electrical current density $\mathbf{j} = e(n_i \mathbf{u}_i - n_e \mathbf{u}_e)$. Equations are then derived starting from the usual mass and momentum continuity equations, involving quantities just described and connecting them to electric and magnetic fields. The calculation requires some approximations. The gyration radius of particles around field lines can be neglected if compared with the characteristic length of fluid motion. Also σ is usually very small, allowing some terms involving charge density to be neglected. Hence MHD equations are as follows:

$$\frac{\partial \rho}{\partial t} + \nabla(\rho \mathbf{u}) = 0 \qquad \textit{mass continuity} \tag{1.21}$$

$$\nabla \mathbf{j} = 0 \qquad \textit{charge continuity} \tag{1.22}$$

$$\rho\left(\frac{\partial \mathbf{u}}{\partial t} + \mathbf{u} \cdot \nabla \mathbf{u}\right) = \mathbf{j} \times \mathbf{B} - \nabla p \qquad \textit{momentum continuity} \tag{1.23}$$

$$\mathbf{E} + \mathbf{u} \times \mathbf{B} = \eta \mathbf{j} \qquad \textit{Ohm's law} \tag{1.24}$$

We must add to this system of equations, the Maxwell equations:

$$\nabla \times \mathbf{B} = \mu_0 \mathbf{j} \tag{1.25}$$

$$\nabla \times \mathbf{E} = -\frac{\partial \mathbf{B}}{\partial t} \cdot \mathbf{B} = 0 \tag{1.26}$$

where the displacement current $\epsilon_0 \mu_0 \partial \mathbf{E}/\partial t$ can be neglected in most cases of interest. The pressure p should be considered as a tensor, since it describes the momentum flux in a generalized direction in space; anyway, in the MHD model, pressure is often considered a scalar. The needed closure in order to obtain a complete and coherent ensemble of equations can be provided by an equation of state for p. To this purpose, an equation of state for pressure is often used of the form $p \propto n^\gamma$, where $\gamma = 1$ represents isothermal compression and $\gamma = 5/3$ adiabatic compression. A different closure scheme can be provided by introducing a continuity equation for energy.

By combining Faraday's and Ohm's law, it is simple to derive the following equation, which describes the coupled dynamics of the magnetic and fluid velocity

fields in the resistive MHD framework:

$$\frac{\partial \mathbf{B}}{\partial t} = \nabla \times (\mathbf{u} \times \mathbf{B}) + \frac{\eta}{\mu_0} \nabla^2 \mathbf{B} \tag{1.27}$$

The first term on the r.h.s. in equation 1.27 describes the convection of the magnetic field with the plasma, and its change due to motions perpendicular to the magnetic field. Starting from this equation, it is possible to show that, in the ideal MHD limit, i.e. in the case where the resistivity η is negligible, the magnetic field lines move as if they were ``frozen ´´in the plasma [14]. The second term describes instead the resistive diffusion of the field across the plasma.

The steady state condition is described by zeroing time derivatives (stationary, $\partial/\partial t = 0$) and considering zero flow (static, $\mathbf{u} = 0$). The MHD equilibrium equation becomes the so called *force-balance equation*:

$$\mathbf{j} \times \mathbf{B} = \nabla p \tag{1.28}$$

that describes the balance between the magnetic force and the thermal expansion force in a plasma. In the equilibrium condition, the force exerted on the fluid element, by a current flowing perpendicular to the magnetic field, balances the plasma kinetic pressure, so that everywhere in the plasma the local pressure gradient is balanced by the Lorentz force. Note that, since ∇p is perpendicular to both magnetic field and current density, surfaces of constant magnetic flux are also isobaric surfaces. The balance described in equation 1.28 is even more explicit if we introduce an expression for $\mathbf{j}$ using Ampere's law, so obtaining the *pressure balance condition*:

$$\nabla \left(p + \frac{B^2}{2\mu_0} \right) = \frac{1}{\mu_0} (\mathbf{B} \cdot \nabla) \mathbf{B} \tag{1.29}$$

On the r.h.s. of the equation, a term coming from both bending and parallel compression of the magnetic field (i.e., respectively, coming from the changes of the direction of $\mathbf{B}$ and of its magnitude along the field line) is balanced by the gradient of the sum of kinetic pressure p and magnetic pressure $B^2/2\mu_0$ which corresponds to the parameter β, defined in equation 1.14. β measures the economic efficiency of the confinement because the fusion power output roughly scales as p^2, while B is the magnetic field which has to be externally provided. Since poloidal or toroidal magnetic field components alone could be used in the above definition, the β parameter is also called poloidal β_θ or toroidal β_ϕ, respectively. Usually, β is limited by the occurrence of MHD instabilities and laboratory plasmas tends to have values of about 10% at most [12].

For an axisymmetric system, it is convenient to re-write the force balance equation, providing a useful analytical tool for equilibria calculation in the case of toroidal configuration. Using the coordinates (R, ϕ, Z) (see figure 1.6), the axisymmetric equilibria can be described by a two-dimensional nonlinear elliptic partial

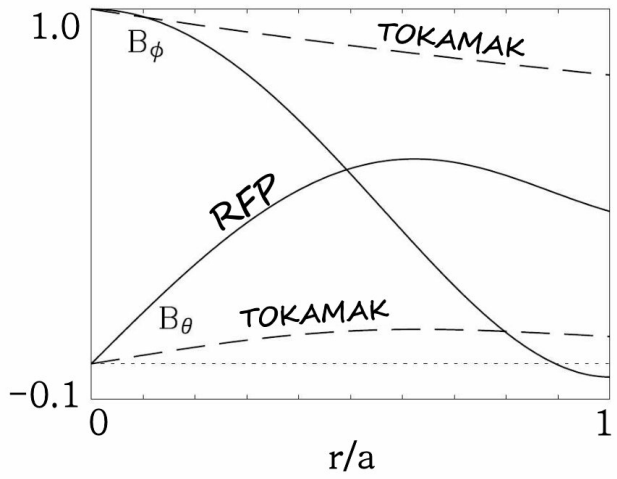

Figure 1.7: Typical radial profiles of the toroidal B_ϕ and poloidal B_θ components of the equilibrium magnetic field in a tokamak (dashed lines) and a RFP (continuous lines). The profiles are normalized to the value of toroidal magnetic field in the plasma center.

differential equation, called *Grad-Shafranov equation* (GSE) [14–16]. The GSE can be written as:

$$\Delta^* \psi_p = -2\pi \left(F \frac{\mathrm{d}F}{\mathrm{d}\psi_p} + \mu_0 R^2 \frac{\mathrm{d}p}{\mathrm{d}\psi_p} \right) \tag{1.30}$$

where A is an elliptic operator defined as

$$\Delta^* = R \frac{\partial}{\partial R} \left(\frac{1}{R} \frac{\partial}{\partial R} \right) + \frac{\partial^2}{\partial z^2} \tag{1.31}$$

Equation 1.30 specifies the toroidal equilibrium (magnetic field and flux, current density, and pressure profiles) when the two free functions $F(\psi_p) = RB_\phi(\psi_p)$ and $p = p(\psi_p)$ are given. Here ψ_p is the poloidal magnetic flux, which is used to label the magnetic flux surfaces in a toroidal system.

1.3.2. Tokamak and RFP configurations

Different toroidal configurations are characterized by different magnetic field and safety factor profiles, instability behavior and maximum attainable β values at comparable input power. We will focus here on two configurations, the Tokamak and the RFP; the latter will be extensively treated in this thesis. These have similar features in particular in both of them a toroidal current is inductively driven by an external circuit, and generates a poloidal magnetic field that confines and compresses the plasma. On the other hand, a part of the toroidal field is generated by external coils [17].

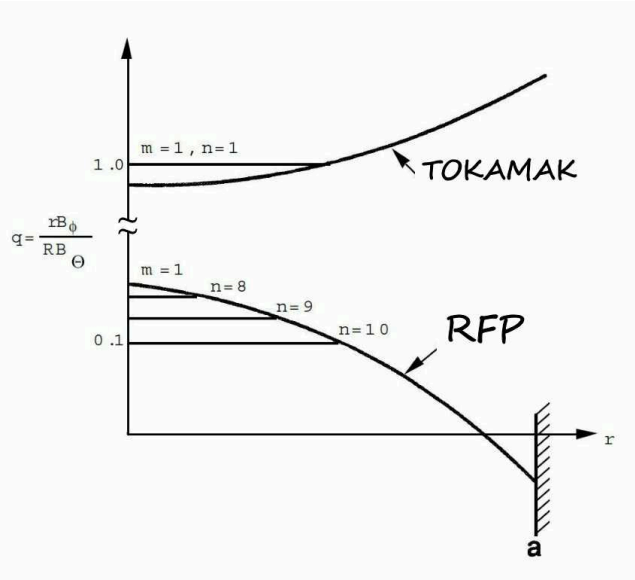

Figure 1.8: Typical safety factor profiles for a tokamak (above) and a RFP (below). Horizontal lines show the positions of resonances (m = 1,n).

Tokamak and RFP configuration present also some important differences, both in the basic physics processes and in some technological aspects. Typical magnetic field and safety factor profiles in the tokamak and in the RFP are compared in figure 1.7. The tokamak is characterized by a relatively high toroidal field, that can reach values of several T in high field machines, and a much weaker poloidal magnetic field. On the other side, in RFP the strength of the poloidal and toroidal components is comparable; a point to underline is that the toroidal field at the edge is much lower for RFP, and hence this kind of configuration has less demanding technological issues. Moreover, the condition $q > 1$ limits in tokamaks the toroidal current and the related Ohmic heating of the plasma. To reach thermonuclear conditions it is hence necessary to adopt additional heating systems such as neutral beam injection or radio frequency heating, with the result of increasing the cost and complexity of the machines.

Here we introduce two dimensionless parameters that are often used to describe pinch equilibria like the tokamak and the RFP. These are the so called *pinch parameter* Θ and the *reversal parameter* F, and are defined as follows:

$$\Theta = \frac{B_\theta(a)}{\langle B_\phi \rangle}, \; F = \frac{B_\phi(a)}{\langle B_\phi \rangle} \tag{1.32}$$

where the brackets indicate the average over the plasma poloidal section. In terms of these quantities, the tokamak is typically a low-Θ device with $F > 0$, while RFP is a relatively high-Θ configuration, with $F < 0$.

Tokamaks and RFPs are characterized by very different safety factor profiles, as shown in figure 1.8. For stability requirements, tokamak operation is possible at

$q > 1$. The condition $q \approx 1$ is called *Kruskal-Shafmnov limit* and is related to the possibility for a strong ($m = 1$, $n = 1$) kink instability to become unstable. This can bring in some cases to violent current disruptions, with possible damages in the vessel components. In its standard operation, the tokamak safety profile increases monotonically with the radial coordinate r and it reaches typically values $q(a) \approx 3$ at the edge. Other types of safety factor profiles have been studied in advanced tokamak operation, e.g non monotonic dependencies [18].

The RFP is intrinsically a low safety factor device, $q << 1$, due to its toroidal magnetic reversal. In fact in the RFP the current is driven well above the *Kruskal-Shafranov limit* [19, 20]; this fact has many consequences on its stability features. In its standard operation, the RFP is in fact characterized by a broad spectrum of resonant MHD instabilities which have great impact both on the dynamics of this configuration and on its transport properties, as explained in the next sections.

1.4 Helical states in the RFP plasma configuration

A perturbed quantity $\mathbf{A}$ in a toroidal plasma can be fourier analysed as follows:

$$\mathbf{A}(r) = \mathbf{A}_0(r) + \sum_k \tilde{\mathbf{A}}_\mathbf{k}(r) e^{i(\mathbf{k}\cdot\mathbf{r} - \omega t)} = \mathbf{A}_0(r) + \sum_k \tilde{\mathbf{A}}_\mathbf{k}(r) e^{i(m\theta + n\phi - \omega t)} \tag{1.33}$$

where $\mathbf{A}_0$ is the unperturbed time dependent component and $\mathbf{k} = (k_r, k_\theta, k_\phi) = (k_r, m/r, n/R)$ for toroidal periodicity, is the wavevector in toroidal coordinates. Each couple (m, n) represents a helical perturbation, or mode. The angular frequency ω is in general a complex quantity $\omega = \omega_R + i\omega_I$, of which the real part describes the propagation velocity and the immaginary part represents a growth ($\omega_I > 0$) or a damping ($\omega_I < 0$) of the perturbation amplitude.

Also magnetic perturbations can be expressed in terms of Fourier component:

$$\mathbf{B} = \mathbf{B_0} + \mathbf{b} = \mathbf{B_0} + \sum_{j=r,\theta,\phi} \mathbf{e}_j \sum_{m,n} b^j_{m,n} e^{i(m\theta + n\phi + \phi_{m,n})} \tag{1.34}$$

where $\mathbf{B}_0$ represents the equilibrium magnetic field and $\mathbf{b}$ the perturbation. It can be shown that the wave vector of the most unstable perturbation is aligned to the magnetic field $\mathbf{k}\cdot\mathbf{B} = 0$; in fact, a perturbation with $\mathbf{k}\cdot\mathbf{B} \neq 0$ would bend the mean magnetic field and thus it would have an energetic cost. It can be shown that perturbations are aligned to the magnetic field when the safety factor assumes rational values:

$$q(r_{res}) = \frac{r_{res}}{R_0}\frac{B_\phi(r_{res})}{B_\theta(r_{res})} = -\frac{m}{n} \tag{1.35}$$

with r_{res} the radial positions (called resonant surfaces) where q assumes rational values. This explains why the safety factor profile behavior is so important when dealing with axisymmetric machines, for example, as reported in subsection 1.3.2,

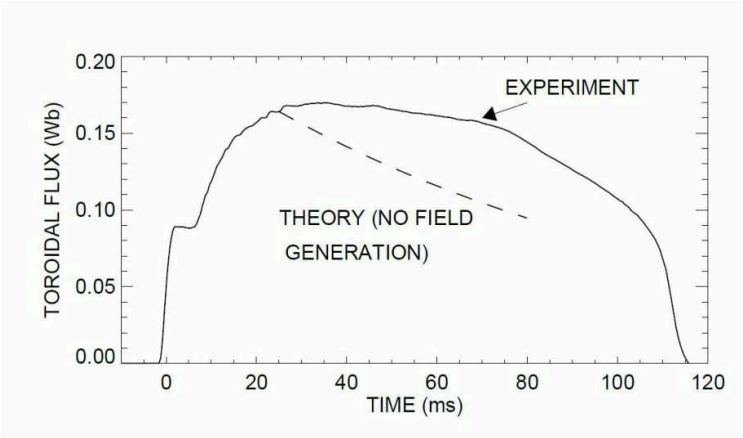

Figure 1.9: Example of the experimental evolution of the toroidal flux sustained by the MHD dynamo effect. Dashed line shows the expected behavior without dynamo.

tokamak machines use a monotonically growing q profile together with the value of safety factor on axis $q(0) > 1$.

Even if a configuration is stable in the ideal limit, other instabilities, characterized by a slower growth rate, occur. In this case (resistive MHD equations), magnetic field lines tear and reconnect during their evolution: the radial magnetic component varies in space due to a current profile with a gradient localized where the poloidal component of the magnetic field changes its sign. When this gradient is sufficiently high, a tearing instability is triggered, which causes the magnetic field lines to bend and reconnect. The resulting magnetic configuration is characterized by the presence of magnetic islands.

1.4.1. Dynamo effect and MH states

If a RFP equilibrium was governed only by resistive diffusion, the characteristic reversal of the toroidal magnetic field would be lost very soon and the discharge terminated. The magnetic field in static cylindric conductor with minor radius a, subject to resistive diffusion, is described by:

$$\frac{\partial \mathbf{B}}{\partial t} = \frac{\eta}{\mu_0} \nabla^2 \mathbf{B} \tag{1.36}$$

The toroidal component of magnetic field is expected to decay exponentially in time with a time constant $\tau_R = \mu_0 a^2/\eta$ (see figure 1.9), where η is the resistivity of the conductor. It is generally observed that the RFP configuration lasts as long as the plasma current is sustained, which is usually longer than the resistive diffusion time. Some mechanisms must be present to regenerate the magnetic field, continuously lost through diffusion; this mechanism is called *dynamo*. Let us consider the parallel

component of the mean-field Ohm's law:

$$E_{\parallel} = \frac{\mathbf{E}\cdot\mathbf{B}}{b} = \frac{E_{\phi}B_{\phi}}{B} = \eta j_{\parallel} \tag{1.37}$$

Since E_{ϕ} and B are always positive throughout the radius, $E_{\parallel}$ at each radial position is proportional to B_{θ}, which changes sign near the edge. Respect to what happens in the experiment, the current appears to be greater in the plasma core and lower at the edge; the discrepancy is accounted precisely by the dynamo effect [21]. The origin of the dynamo is believed to be due to the magnetic activity peculiar of RFP q, defined in formula 1.20, and in particular in the non-linear interaction of $m = 1$ modes, which are continuously excited according to the shape of the safety factor profile. The standard operation in RFP, where many modes resonate in the plasma interior, is commonly referred as Multiple Helicity (MH) regime and the excited $m = 1$ modes as *dynamo modes*. The result of having a wide spectrum of excited tearing modes is the magnetic stochasticity related to the overlap of many small islands, as implied by high values of the Chirikov parameter [22] s^2, as well as to a turbulent plasma magnetic flow. In this situation, it is useful to write the velocity field $\mathbf{V}$ (flow) and the magnetic field as a sum of unperturbed and perturbed terms:

$$\mathbf{B} = \mathbf{B_0} + \tilde{\mathbf{b}};\ \mathbf{V} = \mathbf{V_0} + \tilde{\mathbf{v}} \tag{1.38}$$

The perturbation terms are found to be responsible for the poloidal electric field via a dynamo mechanism [23]; the 0 order quantities sum to zero for symmetry reasons and:

$$\mathbf{E}_D = \mathbf{V}\times\mathbf{B} = (\mathbf{V_0} + \tilde{\mathbf{v}})\times(\mathbf{B_0} + \tilde{\mathbf{b}}) \approx \tilde{\mathbf{v}}\times\tilde{\mathbf{b}} = \sum_n \tilde{\mathbf{v}}_{\mathbf{1,n}}\times\tilde{\mathbf{b}}_{\mathbf{1,n}} \tag{1.39}$$

Since the dynamo mechanism leads to radial stochasticity of the magnetic field, the main contribution to particle and heat transport losses is due to parallel diffusion of electrons along the field lines; actually, transport can be described in the Rechester-Rosenbluth approximation, where the electron diffusivity is related to the magnitude of magnetic perturbations [24]:

$$\chi_e(r) \propto \frac{\tilde{b}_r^2}{B(r)^2} \tag{1.40}$$

The excitation of many magnetic instabilities has other consequences: in MH regime, $m = 1$ modes interaction with one another is responsible to an overall, toroidally localized plasma deformation, due to constructive interference of the $m = 1$ radial components; phase differences tends to zero thanks to viscous torque transfer, and the resulting localized building, commonly referred as locking or slinky pattern [25], causes the field lines to intersect the first wall and there release a huge amount of thermal power. Moreover, non linear interaction of $m = 1$ modes has been proved

to excite the resonance of $m = 0$ modes; according to the shape of the safety profile q, $m = 0$ modes resonate at the reversal; the resulting $m = 0$ islands tend to lock each other and with the $m = 1$ ones, following the relation $\alpha_{0,n} = n\phi_0 - \Delta_0$, being $\Delta_0 = \pm\pi/2$ and ϕ_0 is the toroidal location of the $m = 1$ interference pattern. The presence of the $m = 0$ islands chain influences deeply the confinement features in the edge region [26].

Though the exact reconstruction of the current pattern in RFP should account for the dynamo contributions, for common applications, such as the equilibrium reconstruction, a mean-field approach is used, based on Taylor's modellization of RFP. This modellization is based on the conservation of magnetic helicity in a force free condition ($\nabla \times \mathbf{B} = 2\lambda\mathbf{B} = \mu\mathbf{B}$) for the magnetic field; a spatial solution, in cylindrical geometry, is described by the Bessel functions J_0, J_1:

$$B_z = B_0 J_0(\mu r);\ B_\theta = B_0 J_1(\mu r);\ B_r = 0 \tag{1.41}$$

and known an *Bessel Function Model* (BFM). Practical models based on the BFM, such as the $\mu\&p$ model [27] used for equilibrium reconstructions in RFX-mod, do not consider μ as a constant but as a function of radius, to account for the resistivity increase as one moves toward the chamber wall ($r = a$). $\mu\&p$ accounts also for the presence of pressure gradient, solving:

$$\nabla \times \mathbf{B} = \mu(0)\left[1 - \left(\frac{r}{a}\right)^{\alpha}\right] + \left(\frac{\beta_0}{2B^2}\right)\mathbf{B} \times \nabla P \tag{1.42}$$

β_0 being the value on the axis of β.

1.4.2. SH and QSH states

The classical theory of RFP [28] prescribes the presence of magnetic turbulence to generate the dynamo field; however, recently this paradigm is under review. All the RFP experiments displayed spontaneous transitions to a different regime characterized by the growth of a single $m = 1$ harmonic: the whole plasma column assume an helical MHD equilibrium. These states (QSH, or Quasi Single Helicity) feature a strong reduction in magnetic chaos (no secondary island and hence no island overlapping) and flow turbulence. Such regimes theoretically ([29, 30]) can be stationary, this means that the dynamo field is still present, but it works in laminar fashion. Experimental QSH are different from theoretical SH (Single Helicity), since there exists a residual amplitude of modes with $m = 1$ and $|n| > n_0$ (with n_0 the dominant mode): these modes are dubbed *secondary* modes. Overall, the possibility to obtain stationary QSH regimes is still a matter of investigation, since the dominant harmonic tends to crash as toroidal magnetic flux decreases. These periodical back-transitions to MH may indicate that the poloidal current pattern is not efficiently re-generated and thus the laminar dynamo field, if present, can be insufficient.

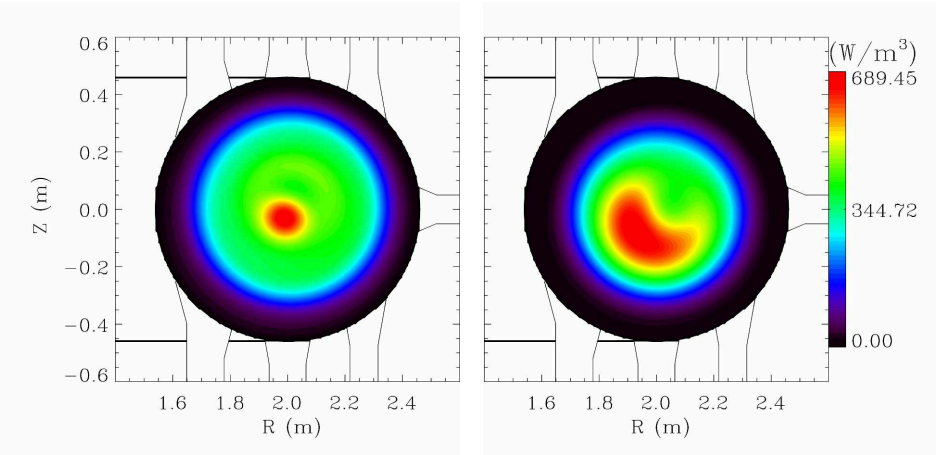

(a) (b)

Figure 1.10: The SXR emissivity reconstruction on a poloidal section of two RFX-mod plasmas. Reconstructions are provided by the SXR tomography. Panel (a) shows a typical MH case, panel (b) reports a SHAx state.

Magnetic chaos in experimental QSH, even if still present, is far lower: chaos due to the overlapping of islands in the core vanishes and conserved helical flux surfaces appear, leaving the peripheral zone still chaotic. An experimental comparison between QSH and MH regimes is shown in figure 1.10. The two contours are obtained with the soft x-rays tomography that is able to reconstruct the emissivity of the plasma on the poloidal section. In panel (a), which reports a MH state, emissivity is axially symmetric and no particular structures are visible. On the contrary, panel (b), reporting a QSH state, shows a bright bean shaped structure out of the axis, this structure is due to closed helical flux surfaces.

Another comparison between MH and QSH configurations is given in figure 1.11. The four panels show the Poincaré plots obtained with the Hamiltonian code ORBIT [31], in poloidal and toroidal sections. While in MH regimes the plasma is characterized by magnetic chaos, in QSH a conserved region with periodicity (1,±7) is visible (red region in panel (b)). During QSH intervals, the presence of secondary modes implies that chaos is still present together to conserved regions. Poincaré plots in panel (b) shows clearly this effect.

QSH regimes do not present a unique onset. Depending on many factors, mainly on the normalized mode amplitude and on the slope of the safety factor profile in the core, the island grows while the plasma center is shifted toward the X-point until it is expelled: this event (separatrix expulsion, see [32]) defines a new state called Single Helical Axis (SHAx) characterized by the presence of a single, near-ideal kink mode and the disappearing of the plasma center and separatrix. QSH states where separatrix and centroid still exist are named Double helical Axis (DAx).

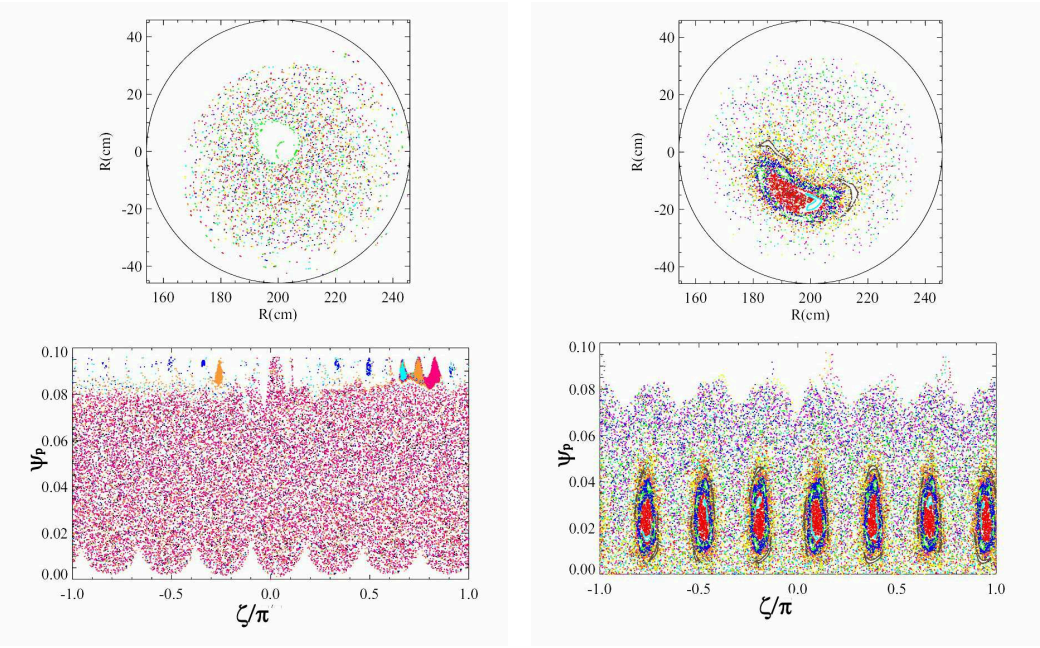

(a) (b)

Figure 1.11: Poincaré plot obtained with ORBIT code. Panel (a) shows a MH case while panel (b) shows a QSH one. Poincaré plots are in the poloidal section on top and toroidal section in bottom.

Resuming: in the various dynamical regimes, the equilibrium axysimmetric part of the RFP fields are similar. The main difference between MH and SH regimes is that in the MH case many $m = 1$ harmonics are excited. QSH regimes represents a midway between SH and MH, in which one $m = 1$ mode peaks over the others, dominating the equilibrium configuration, though residual chaos is still present. Single Helicity equilibrium is preferable from the point of view of plasma confinement.

1.5 Energy loss and transport in the RFP plasma configuration

The toroidal current, which in RFPs sustains the magnetic configuration, also provides energy to the plasma by Ohmic heating. This power source is the most important and often the only heating power in RFP configurations. After a starting transient phase, where the plasma temperature increases, the equilibrium between the source and losses of energy is established. During this period temperature and density are almost constant and the plasma maintains its internal energy, defined in equation 1.43.

$$W_{th} = \int_V \frac{3}{2} \left(n_e \cdot T_e + n_i \cdot T_i \right) \mathrm{d}V \tag{1.43}$$

In the last formula n_e and T_e are the electron density and temperature, respectively, while n_i and T_i are the corresponding values for ions, finally V identifies the entire volume of the plasma.

The losses power are composed of three different contributions:

- The power lost by *radiation*. It is due to line, recombination and bremsstrahlung radiations. Its contribution is about 10% of total losses.
- The power lost by *charge exchange*. It is an atomic process that takes place in the external regions of the plasma: a proton catches an electron from an atom, which is characterized by a lower kinetic energy, becoming neutral. Hence, this new hydrogen atom is not affected by the magnetic field and it is lost, together with its energy.
- The power lost by *transport*. This is the most important contribution to energy losses and it has several sources, the main mechanisms involved will be described in the following.

To better describe transport losses we introduce the parameter χ, called *transport coefficient*. It is defined as follows:

$$Q = -\chi \cdot n \cdot \nabla T \tag{1.44}$$

where Q is the energy flow, n is the density and ∇T is the temperature gradient. Generally, ions and electrons in plasmas have different properties concerning thermal transport, consequently ion (χ_i) and electron coefficients (χ_e) are defined separately; this is because Larmor radius is much higher for ions than electrons while the ions thermal velocity is far lower. Usually analysis are focused on the χ_e profile since, in chaotic regime, electron diffusion along stochastic field lines is the main source of transport.

When a strong magnetic field is present, like in RFP plasmas, transport properties depend on the direction respect to B: the coefficient parallel to the field lines ($\chi_\parallel$) is very high whereas that perpendicular ($\chi_\perp$) is expected to be smaller. Our interest is focused on the perpendicular component, responsible for losses across surfaces to the outer regions, since $\chi_\parallel$ acts to make uniform the temperature on the magnetic flux surfaces.

In RFP plasmas, $\chi_\perp$ depends on various factors: *classical* and *neoclassical* transport; *stochastic* transport and *microinstabilities*.

Without magnetic perturbations, the two main contributions are *classical* and *neoclassical* transport: the term *classical* refers to a regime where the toroidal topology of the magnetic field is neglected and thus the only mechanism able to bring the energy out the plasma are the particle-particle collisions. In fact until they are lost, collisions allow to transfer hot particles from a magnetic field line to another, to the wall. On the other hand, transport is defined neoclassical when toroidal effects become important (low aspect ratio, low collisionality): in this regime, particles can

be subjected to trapping mechanisms due to the magnetic field non-homogeneity along plasma radius. The typical form of the trapped orbit is a banana shape whose width represents the displacement from the original magnetic surface [5].

Nevertheless, in RFP plasmas magnetic perturbations can not be neglected since they are the source of the dynamo effect, fundamental to sustain the configuration. Unfortunately, these perturbations involve the presence of magnetic stochasticity: it means that the magnetic field lines can wander chaotically from the hot plasma core to the colder edge and particles have no more barriers. This kind of transport, also called *anomalous transport*, is widely considered the most important and it has severely limited the confinement performances of RFP configurations for a long time. An example of estimation of $\chi_{e\perp}$ in MH regimes (stochasticity transport) in RFX-mod is reported in [33] where its value resulted of about $500\mathrm{m}^2/\mathrm{s}$.

For high current discharges, dynamo effect can be provided (at least partially) by a single perturbative mode whose amplitude exceeds the others, as reported in paragraph 1.4. In these regimes, called Quasi Single Helicity (QSH), the magnetic order is partially restored and the chaotic plasma core is surrounded by a Cantori layer, usually named Internal Transport Barrier (ITB) [30]. Numerical simulations show that Cantori act as a limit to the field-line wander and make them able to act as a barrier for the energy transport, sustaining temperature gradients [34]. Since power-balance evaluations suggest that heat conductivity value on ITBs exceeds the collisional level, either the cantori gaps allow enough energy to leak through or other instabilities should be considered (e.g. the electrostatic and electromagnetic microinstabilities). Principals microinstabilities are: Ion Temperature Gradient (ITG) [35, 36], Trapped Electron Modes (TEM) [37, 38] and microtearing modes [39, 40]. These transport mechanisms are well studied in Tokamak configurations, since they trigger the most important energy losses, but in RFPs there is not yet clear evaluation of them. Preliminary studies reported that RFP configuration is less subject to microinstabilities [41], but later ones reported that the effects are present and they may be considered as the next limit on energy confinement [30].

The energy loss can be quantified by the confinement time, defined in paragraph 1.2:

$$\tau_e = \frac{W_{th}}{P_{out}} = \frac{W_{th}}{P_{out}} \tag{1.45}$$

In this equation W_{th} is given by formula 1.43 while P_{in} and P_{out} are the power going in and out of the plasma; the second part of the equation hold only if the plasma is in equilibrium. In other words, τ_e is the time required to the plasma to lose its internal energy if the energy losses are constant. A scaling law to determine τ_e for RFP machines is published in [42].

1.6 Scopes and objectives for this thesis

The nuclear fusion pursued by plasmas confinement requires particular conditions, according to paragraph 1.2 these are high density and sufficient high temperature. The latter can be obtained either increasing the power injected in the plasma, which implies a lower efficiency and eventually technological problems, or reducing the power leaving the plasma. In the laster case, the most performant experiments exploit a magnetic confinement field with a toroidal shape. Differences on the magnetic field features (like intensity, shape and origin) distinguish the three most exploited configurations: tokamak, stallarator and RFP.

The study presented in this thesis is focused on the RFP configuration in which the best performance in the limiting energy losses are achieved with high current discharges. The improvement obtained during these discharges is due to the reducing of the plasma chaos in concomitance to a change of plasma topology that becomes helical (achieving the so-called *helical* regimes). Transitions to these *helical* regimes are either spontaneous, more and more frequent when the plasma current grows, or driven by the external feedback control, which is a unique feature of RFX-mod experiment. In both cases, *helical* states have transient nature and their dynamics must be investigated.

Actually, the topic of my thesis is the analysis of the thermal dynamics in *helical* regimes. The study is based on the data coming from fast soft x-rays diagnostics, but also magnetic measurements are kept into account. In fact they are used to improve the plasma topology interpretation available with the soft x-rays detection.

After the brief introduction on thermonuclear fusion and magnetic confinement (with a particular attention on the RFP configuration) given above the thesis is structure as follow.

Chapter 2 gives a general description of the RFX-mod experiment presenting the main SXR diagnostics exploited in the analysis of this thesis.

The first analysis performed during my PhD activity is described in chapter 3. The analysis exploit the temperature measured with the SXR diagnostic and the two foil method. It is focused on the identification of energy transport barriers in the core of the plasma column. In particular, the correlation between the modes amplitudes of magnetic perturbations and the magnitude of transport barriers is investigated.

Chapter 4 describes an outcome of the integration between SXR data and the magnetic ones: it is developed an alternative method to reconstruct the SXR emissivity of the plasma during the *helical* state of the plasma. This method is based on the hypothesis that the topology of the plasma is determined by the magnetic equilibrium defined by the main magnetic field and the dominant perturbation. Moreover, once a new and more powerful two foil diagnostic was available another analysis, similar to the one described in chapter 3, can be performed; in this case, in order to achieve a more correct understanding of thermal profiles, the emissivity data must be integrated by the magnetic ones. The algorithm to combine magnetic and thermal data coming from the new diagnostic is described in chapter 4 too.

The results of the new analysis are reported in chapter 5. These results are focused on the dynamics of the temperature barrier in the core of the plasma during a *helical* interval. The main topic of this analysis is the correlations between the electron temperature profile gradient and the amplitude of the perturbative magnetic modes.

During my PhD activity I had the possibility to adapt the algorithm for the analysis of SXR data, developed for RFX-mod diagnostics, to another experiment, i.e. the Madison Symmetric Torus. Chapter 6 describes how the algorithm has been converted to the Madison experiment. As described in the following, tomography devices of MST and RFX-mod have different features; for instance, MST experiment did not have two foil diagnostics for the fast temperature analysis. Consequently, the aim of the converted algorithm has changed in the estimation of the temperature profile instead of the emissivity one. Besides the conversion of the algorithm, this chapter develops an alternative method to estimate the temperature profile.

Finally, chapter 7 summarizes the results and it draws the conclusions.

CHAPTER 2

The RFX-mod experiment

In order to allow a better understanding of the thesis, this chapter highlights the main features of diagnostics such as SXR tomography and multifilter devices.

In particular the chapter is organized as follow. Paragraph 2.1 describes the RFX-mod experiment. Paragraph 2.2 describes the diagnostics for the Soft X-Rays (SXR) detection. Finally, paragraph 2.3 explains the features of the two foil technique for the temperature estimation with SXR diagnostics.

2.1 Main features of RFX-mod experiment

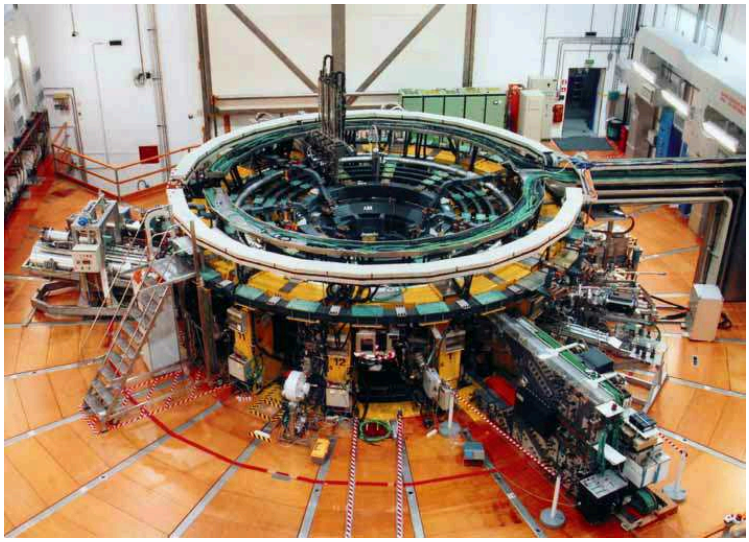

Figure 2.1: Picture of the RFX-mod Experiment

Most of the work presented in this thesis has been done on the RFX-mod machine. RFX-mod experiment is the largest RFP machine in the world: it is based on

a previous machine called RFX [43]; taking advantage of a long machine shut down required to repair the damage of an accidental fire RFX device has been modified (RFX-mod, R_0 = 2m, a = 0.459m) by replacing a thick passive *Al* shell (65mm thickness with 450ms vertical field penetration time) with a thinner *Cu* shell (3mm thickness and 50ms vertical field penetration time) and by installing a set of 192 (4 poloidally×48 toroidally) feedback controlled saddle coils with independent power supplies [44, 45]. The presence of this active feedback control on the magnetic instabilities allow mimicking an ideally conducting wall by locally canceling the radial error field (*Virtual Shell*, VS), or to actively control individual magneto-hydrodynamic modes.

The coils surround the thin copper shell, and, under each of them, a saddle radial field sensor of the same area is mounted on the internal part of the shell, in such a way that the flux at the sensor can be exactly balanced by a suitable current in the active coil. Each coil is individually fed with a maximum current of 400A, with a maximum radial field generated at the plasma edge of 50mT dc that decreases to 3.5mT at 100Hz. They can generate magnetic field harmonics with m=0, n=0÷24 and m=1, n=-23÷24. A digital feedback system controls toroidal and poloidal circuits, toroidal equilibrium and the saddle coils. For MHD control it performs the two-dimensional FFT of B_r and/or B_ϕ measurements, compares it with the preset waveforms and computes via inverse FFT the required references. This allows controlling the MHD modes selectively and has been used for several control schemes.

The toroidal field winding system consists of 48 coils evenly distributed around the torus. The maximum toroidal bias magnetic field it can produce is $B_\phi \sim 0.7T$ at the beginning of the discharge, and a reversed field at the wall of $B_\phi(a) = 0.5T$ during the current flat-top. The poloidal flux swing, which induces the plasma current, is provided in RFX-mod by the so called magnetizing winding, or transformer winding. No iron core has been adopted, even though it would have reduced the coil dimensions and costs. The idea was to avoid magnetic field saturation and asymmetries and to improve the accessibility. The first wall of the RFX-mod machine is composed of 2016 rectangular graphite tiles, which cover the entire inner surface of the toroidal vacuum vessel. Graphite was chosen because it is a low-Z material, which should keep the plasma Z_{eff} value low.

2.2 Soft x-rays diagnostics in RFX-mod

In this section we shall describe the general features of the Soft X-Rays (SXR) diagnostics implemented in RFX-mod.

Typically, SXR diagnostics use arrays of Silicon detectors covered by Beryllium filters whose thickness determine the detectable energy interval. In figure 2.2 a scheme of the structure for the typical SXR diagnostic is reported. The view area of these detectors is limited by a pinhole to a very narrow cone and in RFX-mod it

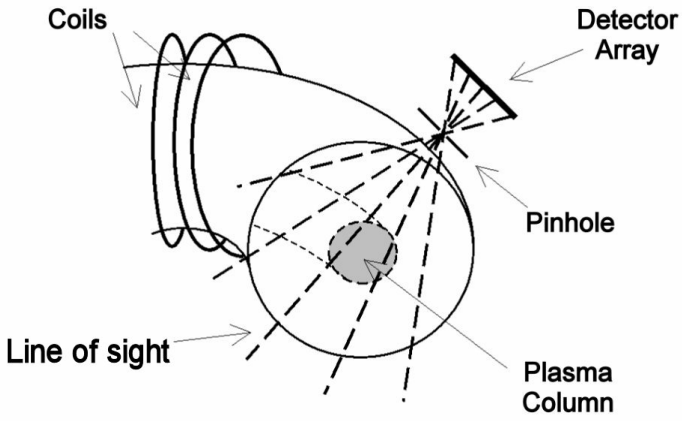

Figure 2.2: Sketch of a generic SXR diagnostic for a toroidal plasma experiment. The anatomy is reported.

is always possible to approximate it with a line [46].

SXR diagnostics provide brightness data f relative to the plasma SXR emission; brightness is defined as the integration of the plasma emissivity ϵ over the line of sight defined by the detector-pinhole geometry and it is mathematically expressed by the Radon equation, reported here:

$$f = \int_L \mathrm{d}l \int \mathrm{d}E \epsilon(E, l) \mathrm{T}_{Be}(E)\, \mathrm{A}_{Si}(E) \tag{2.1}$$

where L is the geometry of the sight line and $\mathrm{d}l$ is its infinitesimal element; E is the emission energy; $\mathrm{T}_{Be}(E)$ is the transmission function of the Beryllium filter and $\mathrm{A}_{Si}(E)$ is the absorption function of the Silicon detector.

Up to now these diagnostics have been used for two main applications: the tomographic inversion and the temperature measurements with the two foil technique.

- Tomography is a very powerful and non perturbative tool to obtain a description of the plasma emissivity over a poloidal section with a high time resolution; it is based on tens of lines of sight displaced on the same poloidal section and with the same filter thickness. To solve equation 2.1 and obtain the tomographic inversion three methods can be used: the Cormack technique [47], [48]; the maximum entropy constrained finite element algorithm [49], [50] and, finally, a hybrid method [51], [46]. Up to now all these methods have been implemented but the Cormack one gives the best results. Since analytical solutions of Radon equation are exploited, Cormack method is also addressed as analytical.

- Two foil technique on SXR diagnostics allows the determination of electron temperature T_e from the ratio R of two brightnesses from lines of sight with

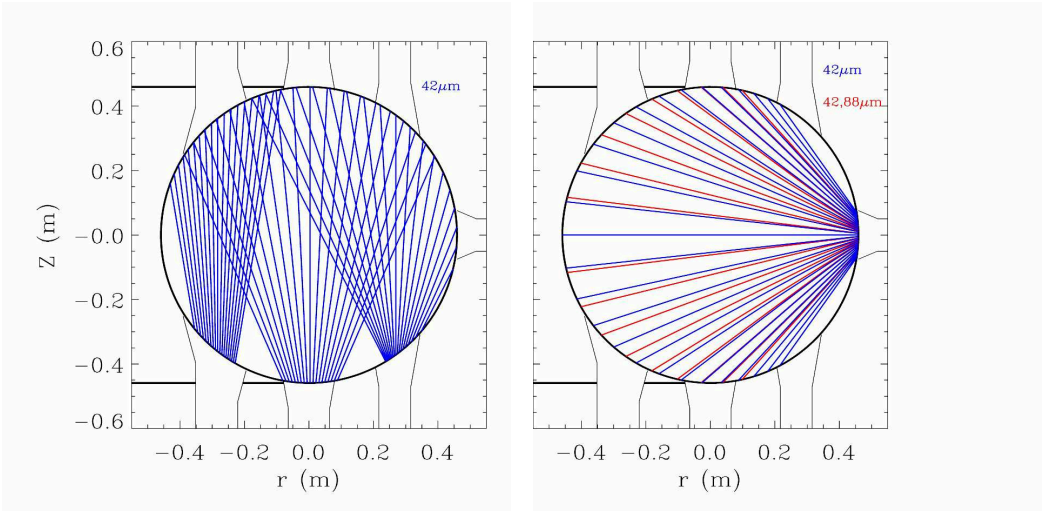

(a) (b)

Figure 2.3: Scheme of SXR lines of sight at the tomography toroidal angle. Panel (a) shows the vertical lines of sight; panel (b) depicts the horizontal lines of sight belonging to both tomography and DSX3 diagnostics (blue chords employ *Be* filters of 42μm, red chords employ 42μm and 88μm filters).

the same position and geometry but different filter thicknesses. In fact, the ratio R of the two brightnesses depends mainly on the highest electron temperature along the sight lines [52, 53].

In RFX-mod there are four SXR diagnostics identified as: Diagnostic Soft X-rays Multifilter (DSXM) [54], Diagnostic Soft X-rays Tomography (DSXT), Diagnostic Soft X-rays multiChannel (DSXC) [55] and Diagnostic Soft X-rays 3-arrays (DSX3); table 2.1 resumes their features.

Diagnostic	Position ϕ_{tor}	Function	Filter (μm) [lines N°]
DSXM	7.5°	T_e	37[1]; 75[1]; 150[1]; 300[1]
DSXT	202.5°	Tomography	42 [57+46]
DSXC	262.5°	T_e	47[5]/96[5]; 36[5]/72[5]
DSX3	202.5°	T_e & tomography	42 [46]; 88 [19]

Table 2.1: Resume of the principal characteristics of the SXR diagnostics implemented in RFX-mod.

DSXM diagnostic reveals T_e along one line of sight passing through the center of the chamber; it is characterized by: three couples of filters (37/75μm, 75/150μm and 150/300μm); toroidal angle ϕ_{tor} = 7.5°and a sampling rate up to 5kHz.

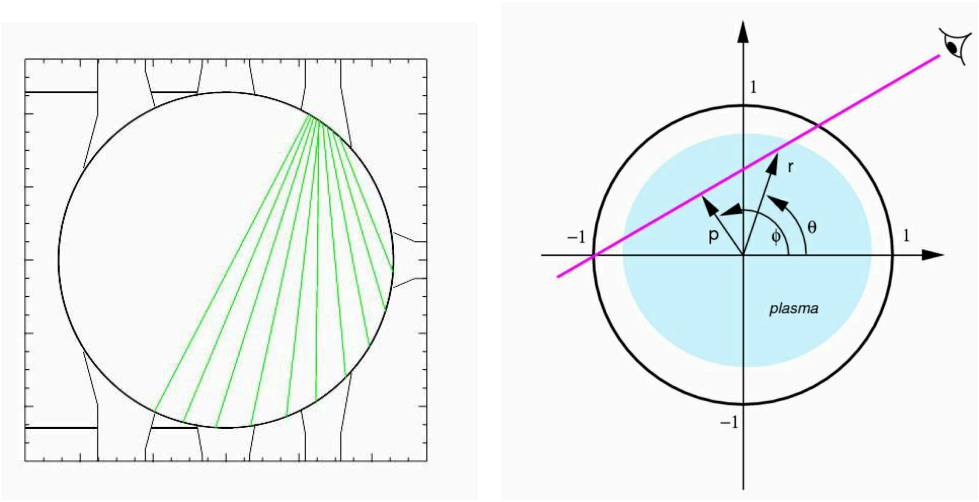

(a) (b)

Figure 2.4: (a) DSXC diagnostic: scheme of the lines of sight in the poloidal section. (b) Graphic display of the parameters (p, ϕ) for the definition of a line of sight in the poloidal section.

DSXT has 103 lines of sight, 46 of which are in a horizontal probe (they are shared with the DSX3) and 57 in three vertical ones; all of them have *Be* filter with thickness equal to 42μm. Its toroidal position is ϕ_{tor}= 202.5°. The geometrical scheme of the DSXT lines of sight is shown in figure 2.3: panel (a) reports the lines of sight belonging to the three vertical probes and (b) shows those of the horizontal probe; lines of sight in blue have only a filter thickness (42μm) while red chords have two filters thicknesses (42μm and 88μm).

DSXC determines the T_e along 10 lines of sight which cover about half of the poloidal section of the chamber at the toroidal angle ϕ_{tor} = 262.5°. The five most internal lines of sight have a filters couple of 47/96μm while the remaining five, the external ones, use the filter couple 36/72μm. Figure 2.4(a) shows the sketch of the ten lines of sight.

Finally, DSX3 is at the same time an upgrade of tomography and a new multi-chords diagnostic for fast temperature determination. It adds 46 lines of sight with horizontal geometry to DSXT and, on the other hand, 19 of them can also read T_e with the two foil technique. The geometry of its lines of sight is shown in figure 2.3(b).

Geometry of each chord on the poloidal section of the chamber can be uniquely identified by two parameters which generally are the impact parameter p (defined as the perpendicular distance from the origin to the line of sight) and the chord angle ϕ (defined as the angle between the normal to the line of sight and the equatorial plane in counterclockwise direction). Figure 2.4(b) illustrates the (p, ϕ) coordinates

for a generic chord on the poloidal section.

2.3 Details concerning the two foil technique

The discussions in the following chapters make frequent use of the two foil technique, for this reason a more detailed description is reported in this subsection.

The theory involving temperature estimation with the two foil technique can be understood considering the spectrum of plasma emissivity due exclusively to the bremsstrahlung effect (the plasma considered has not impurities):

$$j(E) = \mathrm{n_e n_i} Z^2 \left(\frac{\mathrm{e}^2}{4\pi\epsilon_0}\right)^3 \frac{4}{3\sqrt{3} m_e^2 \mathrm{c}^3 \hbar} \left(\frac{2m_e}{\pi T_e}\right)^{1/2} \exp\left(-E/T_e \bar{g}\right) \tag{2.2}$$

In this last equation $j(E)$ is the power emitted by a unit of plasma volume at the frequency E/h; $\mathrm{n_e}$ and $\mathrm{n_i}$ are the densities of electrons and ions, respectively; Z is the atomic number of the ions; m_e is the mass of electron; c is the speed of light; T_e is the electron temperature and $\bar{g}$ is the Gaunt factor. The derivation of formula 2.2 can be found in [56].

The brightness on a line of sight for an experimental plasma can be estimated inserting the emissivity spectrum defined in formula 2.2 in the Radon equation (formula 2.1). Note that, in RFX-mod, plasma is composed of completely stripped hydrogen or helium atoms and thus $\mathrm{n_e}$ and $\mathrm{n_i}$ have a fixed ratio.

The exponential dependency on T_e of emissivity implies that the ratio R of two measured brightness values, on the same line of sight, will depend mainly on the highest temperature along the chord.

The above model is over simplified, since impurities in the plasma often cannot be ignored. Other contributions to emissivity, mainly due to the recombination effect, must be kept into account and thus formula 2.2 becomes:

$$j(E) = \alpha \sum_i \mathrm{n_e n_i} \frac{\mathrm{e}^{E/T_e}}{\sqrt{T_e}} \left[Z_i^2 g_{ff} + {Z'}_i^2 g_{fb} \beta({Z'}_i)\right] \tag{2.3}$$

$$\beta(Z') = \frac{\xi}{n^3} \frac{\chi_n}{T_e} \mathrm{e}^{\chi_n/T_e} + \sum_{\nu=1}^{\infty} \frac{2\chi_H}{T_e} \frac{{Z'}^2}{(n+\nu)^3} \exp\left(\frac{{Z'}^2 \chi_H}{(n+\nu)^2 T_e}\right) \tag{2.4}$$

The summation in formula 2.3 runs over all the species of ions considered, which are labeled by i [57]; moreover, the factor α is equal to $1.22 \cdot 10^{-39}$ $\mathrm{eV}^{3/2}\mathrm{m}^3$ in case temperature and energy are expressed in eV; $\mathrm{n_e}$ and $\mathrm{n_i}$ are the densities of electrons and of the ions i, respectively; Z_i is the atomic number of the ion i and ${Z'}_i$ is its charge; g_{ff} and g_{fb} are Gaunt factor, finally β is defined in formula 2.4 and it accounts the emission due to the recombination effect. In this last formula n is the shell quantum number, ξ are the vacancies in that shell and χ_n is the ionization

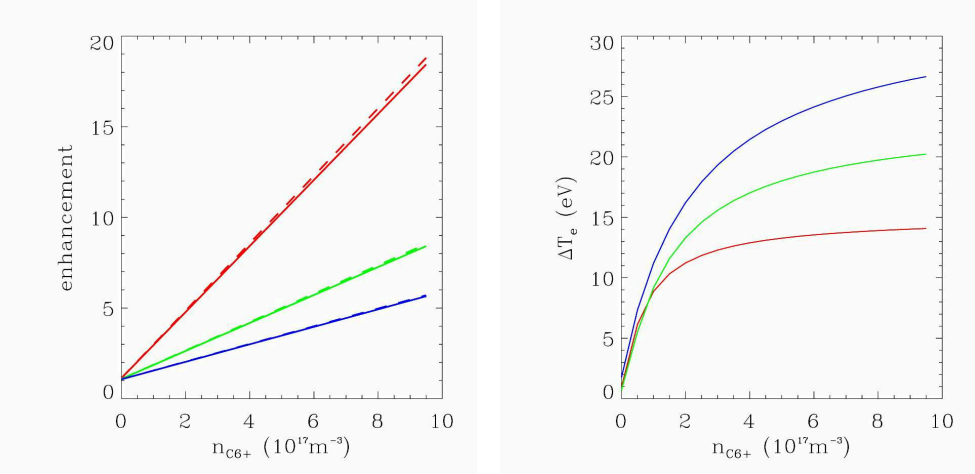

(a) (b)

Figure 2.5: Validity test for the temperature estimation with the two foil method. Panel 2.5(a) shows the enhancement factor as a function of C^{6+} density. Three temperature are reported: 500eV (red line), 750eV(green line) and 1000eV (blue line). Solid line are referred to the 42μm filter while dashed one to 88μm. Panel 2.5(b) shows the estimation error of the temperature due to the bremsstrahlung approximation.

potential; the summation term takes into account those recombinations on shells above the first and χ_H is the hydrogen ionization energy.

Formulae 2.3 and 2.2 have similar dependencies on temperature and thus it is possible to approximate emissivity as pure bremsstrahlung inserting a factor of enhancement K.

This approximation must be verified, therefore the following sensitivity analysis has been performed for a typical plasma of RFX-mod. The emission due to bremsstrahlung and to recombination are computed numerically at various density of impurities and for two filter thicknesses; then the enhancement factor and the temperature with the two foil technique have been estimated. Filters thicknesses used here are equal to those in the DSX3 manipulator, i.e. 42 and 88μm. Such analysis has been performed using three temperature: 500eV, 750eV and 1000eV.

A hydrogen plasma with electrons density equal to $3.6 \cdot 10^{19} m^{-3}$ has been considered. Then higher amounts of Carbon and Oxygen impurities have been added to this plasma. The concentrations of Carbon used (we are considering only C^{6+}) ranged between 0 and 10^{18} particles per cubic meters; the concentrations of Oxygen (namely O^{8+}, O^{7+} and O^{6+}) are equal to $n_{C6+}/5$. These ranges of Carbon and Oxygen densities are chosen keeping into account the typical estimations from spectroscopic measurements [58] in the plasma core for shots of RFX-mod at high current.

The range of the factor K for this analysis has been determined together with

the entities of the errors involved in the temperature estimation with the two foil technique. Such results are shown in figure 2.5. Panel (a) shows the enhancement factors as a function of Carbon density for the three temperatures (500eV is in red, 750eV in green and 1000eV in blue), moreover the two filters thicknesses have been distinguished (solid line for 42μm, dashed one for 88μm). Panel 2.5(b) reports the differences between the original temperatures and those estimated with the two foil technique. From this last plot we can see that the enhancement factor growth does not imply large errors on temperature estimations (2.5%) and thus the approximation highlighted above can be considered good enough.

CHAPTER 3

T_e dynamics during QSH regimes with the DSXC diagnostic

One of the aims of this thesis is to study the behavior of the plasma during the QSH regimes, in particular the attention will be focused on the electron temperature dynamics. This plasma feature is investigated using the DSXC diagnostic which is characterized by an high frequency response and thus it allows a deeper investigation with respect to the past. This chapter shows how the data coming from DSXC have been used to determine the presence and the dimensions of transport barriers inside the plasma.

Transport barriers are identified by the presence of high temperature gradients and two different methods to estimate ∇T_e have been developed in paragraph 3.1. They are the simple incremental ratio between the temperature measurements and the fit based on a step function (the Fermi distribution).

In order to individuate the correlation between the ∇T_e dimension and other quantities during QSH regimes, it has been set up a database. Given the previous studies that demonstrated the QSH to be more probable during the discharges characterized by high current [59], 163 shots have been selected where $I_p \gtrsim 1$MA and, beside the temperature, other plasma quantities have been collected. The modalities adopted for the construction of the database are specified in paragraph 3.2.

Most of the investigations are focused on the link between barrier dimensions and the magnetic configuration of the plasma, precisely on the dependence of ∇T_e on the magnitude of the dominant or secondary modes. The results are reported in paragraph 3.3.

Finally, in 3.4 a simple model which uses the temperature gradient to estimate the thermal diffusion coefficient for the electron χ_e will be discussed. Thanks to the DSXC diagnostic the gradient dataset on which electron thermal diffusivity can be computed is significantly increased with respect to previous estimations; moreover, the correlation between the magnetic modes amplitude and χ_e can be followed within single QSH cycles.

3.1 ∇T_e estimations

This paragraph is dedicated to the computation of the T_e gradient starting from the temperature profiles obtained with the DSXC diagnostic; such gradients are then compared to those estimated with the Thomson Scattering (TS, see [60]) profiles, which is temperature diagnostic with the highest space resolution presently implemented in RFX-mod.

As shown in paragraph 2.2, DSXC can measure the temperature along 10 lines of sight using the two foil technique. The measurements can be considered as the maximum temperature presents in the plasma along each line of sight, even though the exact position is not known. For simplicity we will assume the measured temperature to be localized in the middle of the line of sight, i.e. at the minimum distance from the center of the poloidal cross section. Consequently, each T_e data point can be associated to a radius equal to the impact parameter of its line of sight. This is a good approximation during the Multiple Helicity configuration since the plasma has an almost cylindrical geometry and the typical temperature profile is centrally peaked. For QSH regimes, given their different topology, this approximation is rather poor, nevertheless it is assumed also in the following analysis: in fact the resolution of DSXC, which has ten lines of sight, is not sufficient to distinguish fine difference in the barrier structure. We report an example of such a DSXC profile in figure 3.1.

This temperature profile is the starting point for the computation of ∇T_e, which is intended in the following as the maximum gradient in the profile. The first estimation of ∇T_e is given by the maximum slope computed using the incremental ratio on the measurements. In practice, we have taken the maximum of the difference of two consecutive temperatures divided by the difference of their impact parameters, as reported in equation 3.1:

$$\nabla T_e = \max \left\| \frac{T_e^i - T_e^{i-1}}{p^i - p^{i-1}} \right\|_{i=2\cdots 10} \tag{3.1}$$

In the last equation T_e^i is the temperature measurement for the i^{th} couple of lines of sight and p^i identifies the corresponding impact parameter. Figure 3.1(a) shows an illustration of such a procedure: the red lines represent all the rejected incremental ratios while the red one is considered as ∇T_e. Plot presents with the two vertical dashed line, in the interval in which the gradient typically develops.

This ∇T_eestimation is based only on two measurements and thus it tends to be noisy, especially if the signals are small. In order to avoid this problem another method to estimate ∇T_ehas been developed. To make easier calculations, it should be noted that the steepest slope in the DSXC profile lays typically inside a fixed interval of the radius. This characteristic interval is shown in figure 3.1(b) with the two dashed vertical lines. Consequently, this new estimation of the gradient will be computed focusing the attention on the lines of sight with impact parameters inside that characteristic interval.

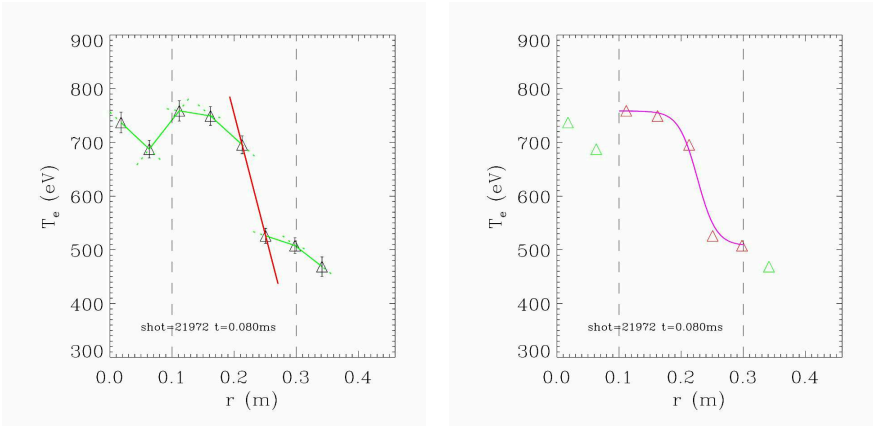

(a) (b)

Figure 3.1: Example of temperature profile obtained with DSXC. (a) Sketch of the ∇T_eestimation: the green lines represent all the rejected incremental ratios while the red one has the highest slope and thus it is considered as ∇T_e. Finally the two dashed lines are indicating the characteristic interval defined as the typical region where ∇T_edevelops and where the five points involved in the fit of the Fermi function are chosen. (b) Example of the fit performed with the Fermi function (magenta curve) on the DSXC profile (red and green triangles). The fitted function is then used to estimate ∇T_e, which is the derivative value in the inflection point. Red triangles are the DSXC data involved in the fit, while green ones are excluded.

Since the temperature profile is expected to have a step shape in correspondence of the transport barrier, we have chosen the Fermi's function to fit the data. Such a function is reported in equation 3.2:

$$T_e(r) = \frac{K_0}{1 + \exp\left(K_1\left(r - K_2\right)\right)} + K_3 \tag{3.2}$$

where K_0, K_1, K_2 and K_3 are four free parameters determined by the fit. The Fermi function has 4 degrees of freedom and thus 5 points are necessary to perform a convergence. When the number of measurements inside the characteristic interval is lower than 5, other chords must be included. In order to maintain the gradient estimation always inside the characteristic interval no more than 2 points can be added; if others points are necessary, the fit is considered wrong. The first measurement added is relative to the couple of lines of sight closest to the characteristic interval with a impact parameter in the inner side, i.e. with a lower impact parameter, while the second one is the closest in the outer side. Once the fit is performed, the analytic derivative in the inflexion point provides the value of the gradient. Moreover, the position of the barrier can be considered as the radius of such a point. An example

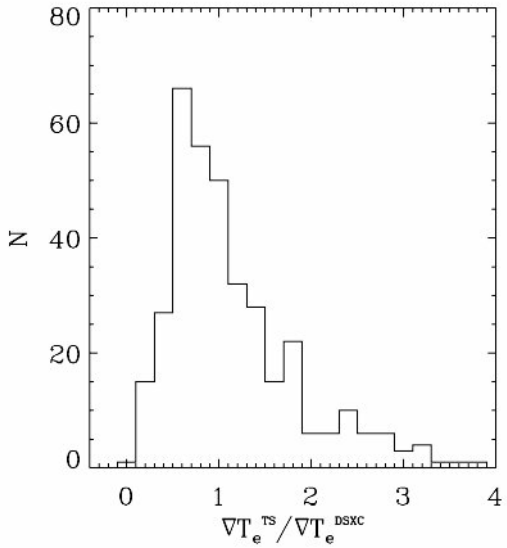

Figure 3.2: Comparison of ∇T_eestimations. The plot reports the distribution of the ratio between the gradient obtained from the TS profile (∇T_e^{TS}) and the one from DSXC (∇T_e^{DSXC}).

of this procedure can been seen in figure 3.1(b) where the fit of the Fermi function is shown in magenta.

We have performed numerous comparisons between the two methods and we found that the gradient estimations are very close, hence both methods can be used alternatively. The incremental ratio method has the advantage to be faster.

As mentioned before, DSXC is able to measure the temperature with high time resolution, and some of the profiles are taken at the same time of TS measurements. Note that Thomson Scattering has not been directly involved on this analysis since it collects only 10 profiles each shot; anyway, thanks to its high spatial resolution (84 points in the camera diameter), it can be used as a benchmark for gradient estimations.

According to 1.4, in order to compare gradients and profiles of two diagnostics at different toroidal point, the dominant mode periodicity, which is (1,-7), must be taken into account: the toroidal separation between the two diagnostics is 180°and thus the TS profile must be rotated by 180°, to be directly compared to the DSXC one. After this operation the gradient on TS profiles (∇T_e^{TS}) is computed with a linear fit on 6 consecutive points: also in this case the steepest gradient is chosen inside the characteristic interval found before.

In order to compare the gradients coming from the two diagnostics the estimations have been performed for 358 profiles, all taken during QSH intervals. In figure 3.2 we report the distribution of the ratio between ∇T_e^{TS} and ∇T_e obtained from the

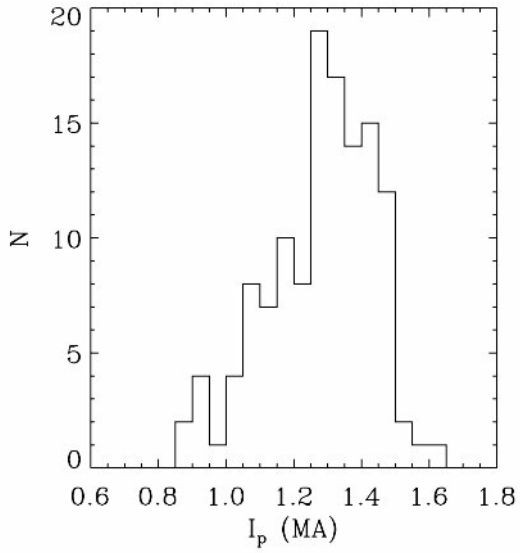

Figure 3.3: Current distribution of the shots included in the database.

DSXC profile. Here the estimation of the gradient in DSXC profiles is given by the first of the methods described, i.e. the maximum incremental ratio on the temperature profile. The distribution is centered near 1, as expected, however there is a notable dispersion. This result is not surprising if we take into account some features of the two diagnostics. For instance, DSXC estimates the temperature from the emissivity of the plasma, while TS uses the velocity of electrons. Moreover, SXR diagnostics get the temperature from line integrals and thus are less sensible to local or sharp variations of temperature. For the same reason the position of the temperature is not really known and the profile reconstruction is based on the approximation that the measurement corresponds to the middle of the line of sight. Besides, the resolution of DSXC is lower than that of TS.

3.2 The database

This paragraph shows the modalities adopted to build up the database; which will be used for the analysis of the thermal behavior in QSH intervals. The pulses included in the database have high values of plasma current in order to increase statistics in QSH states, whose occurrence is higher as the plasma current rises [59]. The distribution of the plasma current is shown in figure 3.3.

During a discharge, QSH intervals have been detected analyzing the magnetic modes amplitudes, in particular the dominant one. In fact the QSH regime is achieved once the energy of the dominant mode (the 1,-7 in RFX-mod) exceeds the others. An example of such a dynamics of magnetic modes is shown in figure 3.4(a) where also another characteristic is pointed out: QSH interval can be split

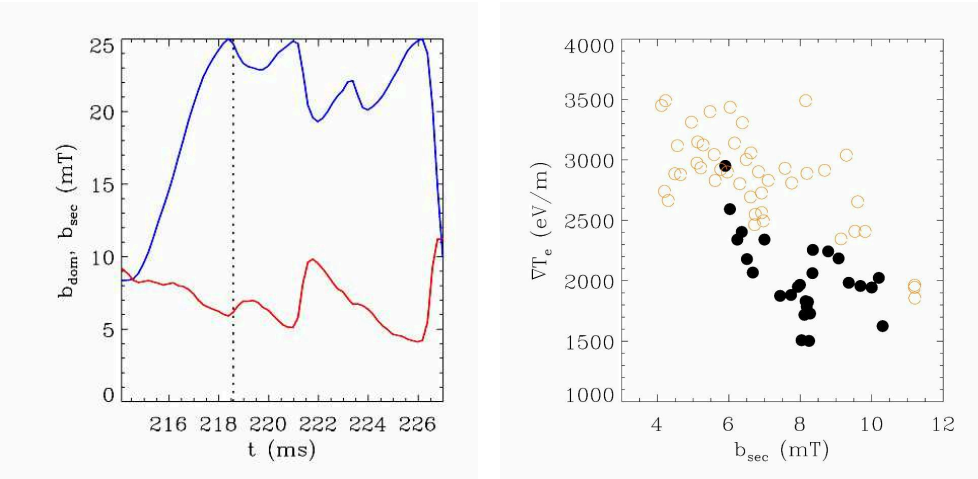

(a) (b)

Figure 3.4: (a) Example of dynamics of magnetic mode amplitudes during a QSH interval. The blue curve represents the amplitude of the dominant mode (with periodicity (1,-7) in RFX-mod) while the red one is the quadratic sum of the secondary modes. The vertical dashed line identifies the end of the *rising* phase and the begin of the *flattop*. (b) Example of correlation between $\nabla T_e$and secondary modes. Here the same QSH interval reported in (a) is shown; the *rising* phase is drawn in black while the *flattop* is in orange. The exponential correlation between these two measurements is clearer during the *rising* phase.

in two phases: the first, where the dominant mode grows (the *rising* phase), and the second, where it saturates and its value is almost constant (the *flattop* phase). The study of some preliminary cases tells us that this magnetic timetable holds also for the temperature gradient. This means that ∇T_e may behave in a different way during *rising* and in *flattop* intervals. An example is shown in the paradigmatic case of figure 3.4(b) in which are plotted the gradient estimations, computed every 0.2ms, of the same interval shown in figure 3.4(a): we can see that, during the *rising* phase (drawn in black), an exponential correlation between the gradient and the secondary magnetic modes is recognizable, but the same relation is no more visible during the *flattop* phase (drawn in orange). For this reason a simple algorithm has been developed, in order to automatically distinguish the two phases.

Moreover, according to the hypothesis that the dominant mode dynamics is strictly linked to the QSH regimes characteristics, we have classified the QSH intervals in four groups: the first is characterized by cases with a smooth growth of the dominant mode and without *flattop* phase; in the second group the growth of the dominant mode does not change, but a stable *flattop* must follow it; the third group is like the second one but now the *flattop* fluctuates; finally the fourth group includes all the cases with a fluctuating growth of the dominant mode during the

rising phase. Examples concerning these four groups are shown in figure 3.5.

Another classification has been introduced and it is based on the shape of TS profile, whenever it is present in the QSH interval. Three classes have been defined: the first corresponds to flat TS profiles (no thermal structure visible), the second to small thermal structures (possible DAx case) and the last to big structures extending more than half of the camera diameter (typical SHAx structure). Figure 3.6 shows three TS profiles related to the three classes.

Finally we have proceeded to collect the most important plasma parameters in a common time scale. The quantities collected are: the amplitudes of all magnetic modes with periodicities from (1,-7) to (1,-24); the mode phases; the pulse number and the time; the value of F and Θ; indicators of the presence of pellets and OPCD (which states for Oscillating Poloidal Current Drive); the plasma current and the temperatures estimated with the DSXC. The common time scale is equal to 5kHz which is the maximum suitable frequency of DSXC. Besides these data, we have computed and saved the temperature gradients and their positions, with both the methods described in 3.1.

Eventually, the database is composed by 63 quantities collected on 97085 instants, belonging to a total of 125 shots.

3.3 The ∇T_ebehavior

After the compilation of the database we can investigate the relations between the temperature gradient and other parameters of the plasma.

This is not the first analysis focused on the temperature gradient: previous studies have investigated the strong correlation between its magnitude and the energy of magnetic modes for both the regimes, MH and QSH; for example [33] for the former and [61] for the latter. Notice that in MH regimes all the magnetic modes are play a perturbing role while in QSH regimes it is fundamental to distinguish the dominant and the secondary modes. The study presented here adds the analysis of the gradient evolution in every QSH interval.

In the following, gradient data will be fitted with equation 3.3, where b_{dom} and b_{sec} are the amplitudes of the dominant and of the secondary modes while **A**, **B**, α and β are the four free parameters of the fit.

$$\nabla T_e = \mathbf{A} \cdot b_{dom}^{\alpha} \cdot b_{sec}^{\beta} + \mathbf{B} \tag{3.3}$$

Before performing the fit it is worth to note that the lines of sight of DSXC cover only half of the poloidal section of the chamber. On the other hand, the helical axis in QSH regimes can lay at any poloidal angle around the camera axis. Consequently a selection of QSH intervals, based on the dominant mode phase η, is necessary. Using the geometrical parameters of DSXC (toroidal angle ϕ =262°30', and slope in the poloidal section of the innermost line of sight equal to 132°30')

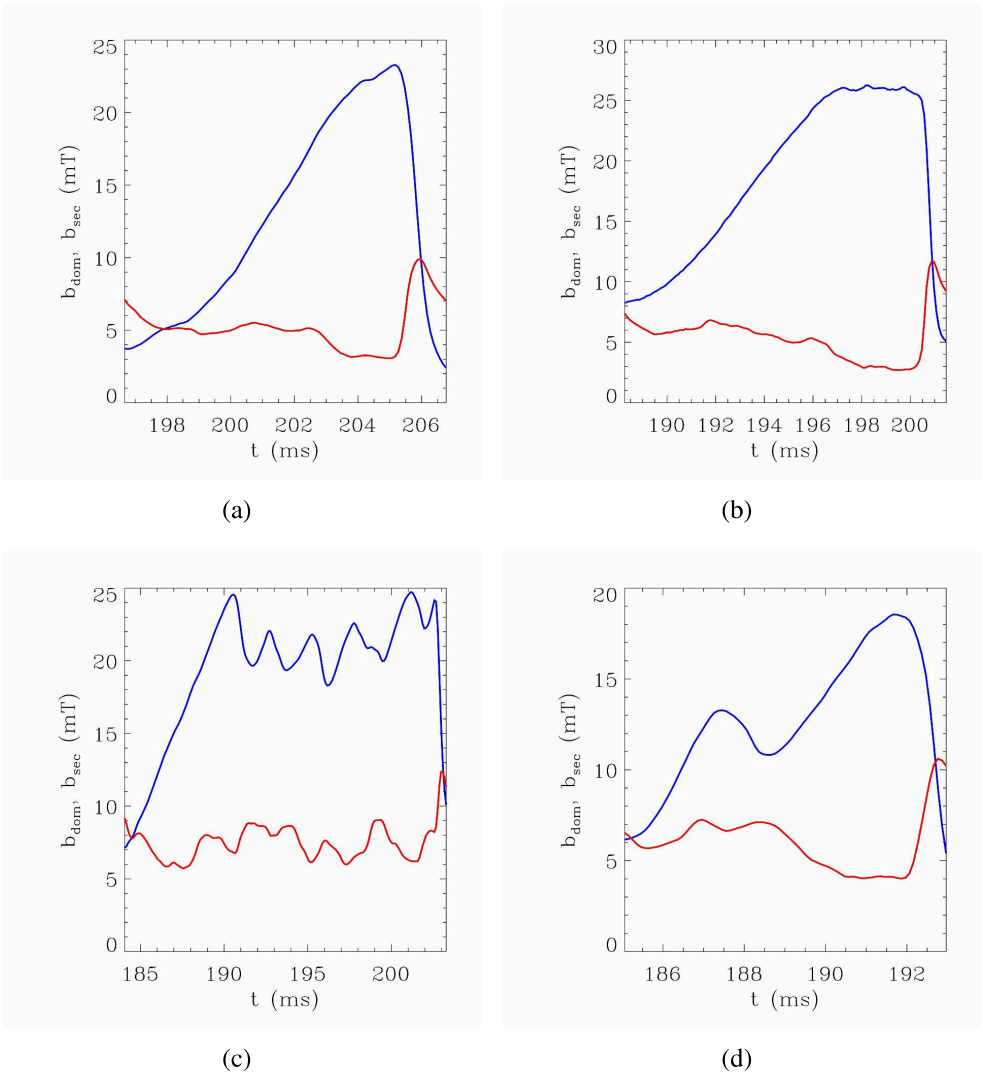

Figure 3.5: Categories of magnetic dynamics for QSH intervals in database. Panel (a): QSH of the first type, there is not *flattop*. Panel (b): QSH of the second type, after a smooth *rising* phase there is a stable flattop. Panel (c): QSH of the third type, *flattop* is saw-toothed. Finally, panel (d) reports an example of magnetic dynamics for a QSH of the fourth type: the *rising* phase is not smooth.

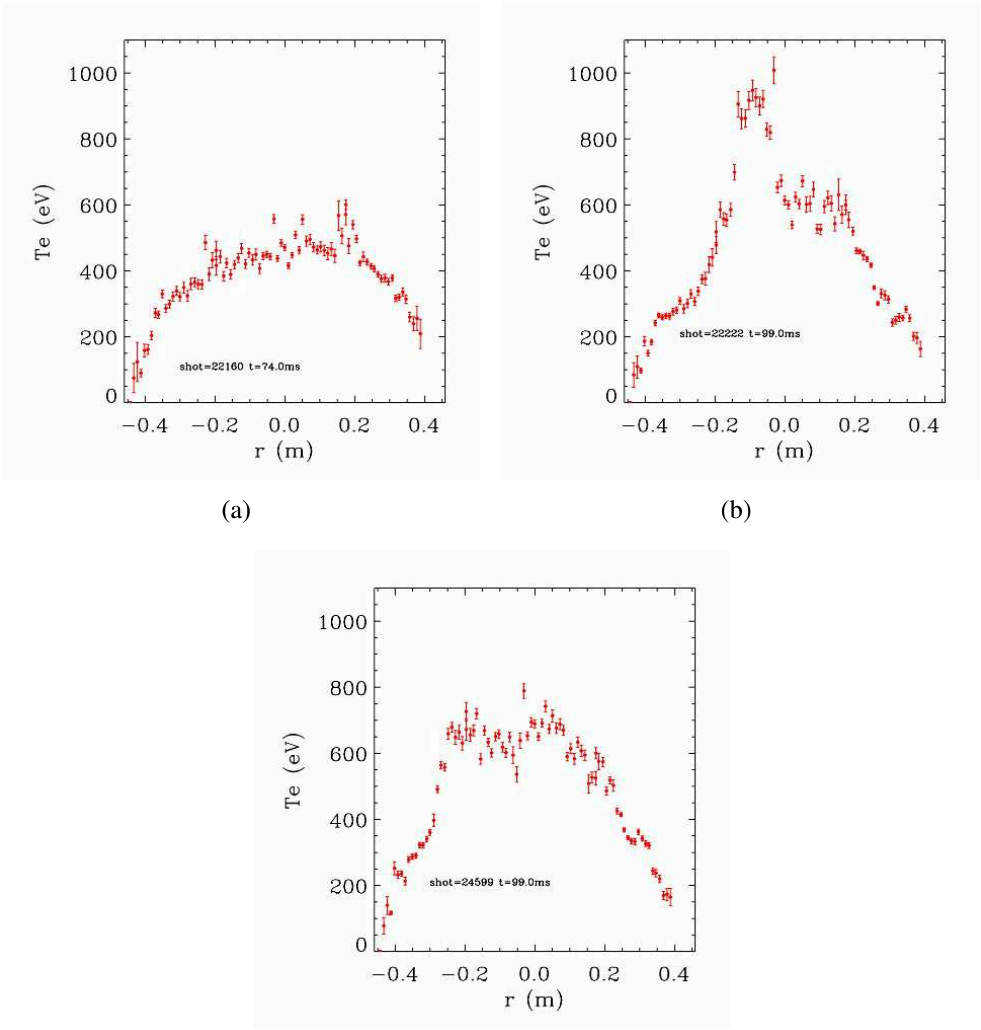

(a) (b)

(c)

Figure 3.6: These TS profiles, all collected during QSH intervals, are showing the three different patterns available for the plasma temperature: (a) flat profile, (b) typical DAx case (characterized by a high and localized temperature peak) and finally, in (c), a fully developed helical structure.

the interval of the phase of the dominant mode has been found and it is reported in formula 3.4, where θ_0 is the dominant mode phase at the toroidal angle $\phi = 0$:

$$100^\circ \lesssim \theta_0 \lesssim 280^\circ \tag{3.4}$$

All the QSH intervals where η exceeds these limits are excluded.

Once the selection has been done, the equation 3.3 is fitted on each QSH interval which has been considered separately. Figure 3.7(a) summarizes the results reporting the distributions of the four free parameters with the red curves. The second and third panels tell us that the dependence of the gradient from the dominant mode is weak (distribution of α around 0) while, in contrast, the dependence from the secondary modes is stronger (β parameter around -0.7). Concerning the other parameters: the distribution of **B** is developed around 0 eV/m, as expected, and **A** concentrates most of the cases between 0 and 10 eV/mT$^{\alpha+\beta}$/m. Previous analysis of ∇T_e dependence on the amplitude of secondary modes during non-QSH shots returned an exponent value of $\beta \simeq -1.4$, see [62]; the lower exponent found here, for QSH regimes, can be referred to the minor importance of chaotic transport, which is driven by magnetic turbulence as explained in 1.5. The black curves report the parameters obtained fitting equation 3.3 in all QSH interval, without any selection on the phase of the dominant mode. The results are similar to the previous ones, this means that the extension of the fully grown helical structure spreads over most of the plasma diameter and hence it can be recognized with DSXC even if its center lays in the other side of the camera.

The analysis has proceeded splitting the QSH interval in *rising* and *flattop* subintervals. Stated that the phase of the dominant mode does not influence the results no further selection has been done. The results are reported in 3.7(b), here the blue curve is referred to the *rising* intervals while the green one is for the *flattop*. These fits do not highlight differences and the results are not different from the previous analysis.

Also, when the dynamics of the dominant mode is used as the discriminating factor (that is in the four typologies introduced in paragraph 3.2) the results do not present significant variations. The distributions of the four parameters can be seen in figures 3.8(a) and 3.8(b): the first and the second typologies are reported in 3.8(a) with the black and red curves respectively (anyway the number of cases of second typology is scarce); the third and the fourth typologies are shown in 3.8(b), also here, with the black and the red curves respectively. The last discrimination applied concerns the presence or not of the OPCD operation during the shot; also in this case the parameters distributions, shown in 3.8(c), do not have a significant change.

Carrying on the analysis in a similar way, we can investigate the relation of the barrier position with the amplitude of dominant and secondary modes. The law used to fit the data is:

$$r_{\nabla T_e} = \mathbf{A}' \cdot b_{dom}^{\alpha'} \cdot b_{sec}^{\beta'} + \mathbf{B}' \tag{3.5}$$

and it is in the same form of 3.3. The results of these last analysis will not be reported because no dependence has been found. This is probably due to the method

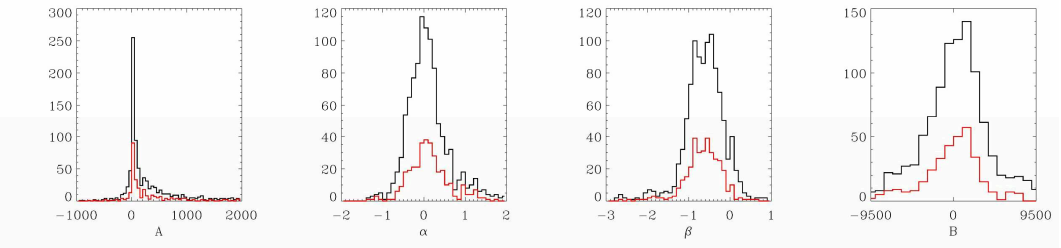

(a)

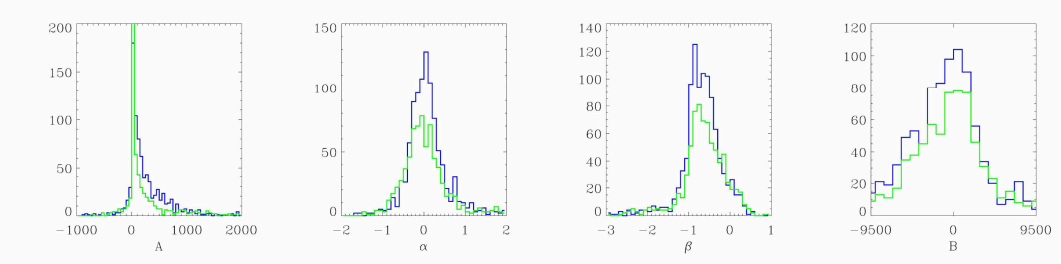

(b)

Figure 3.7: Convergence results for the fitting function 3.3. Each row of plots reports the four free parameter distributions in the order **A**, α, β and **B**. Row (a) shows the distributions obtained considering entire QSH intervals; in the red distributions a selection on the QSH interval has been performed: only the cases where the helical magnetic is in the *right* position are considered, as explained in paragraph 3.3. Panels in (b) are reporting the distributions for the *rising* and *flattop* intervals (in blue and green, respectively).

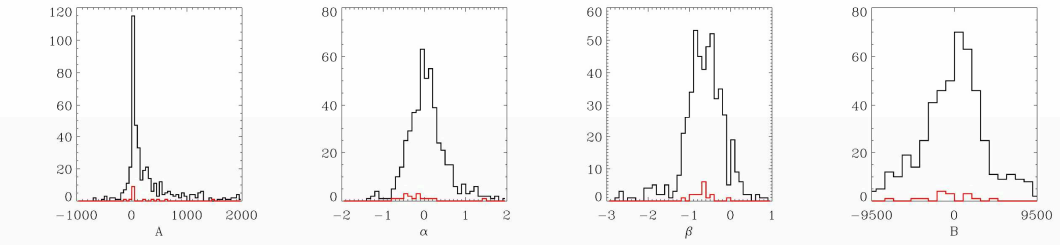

(a)

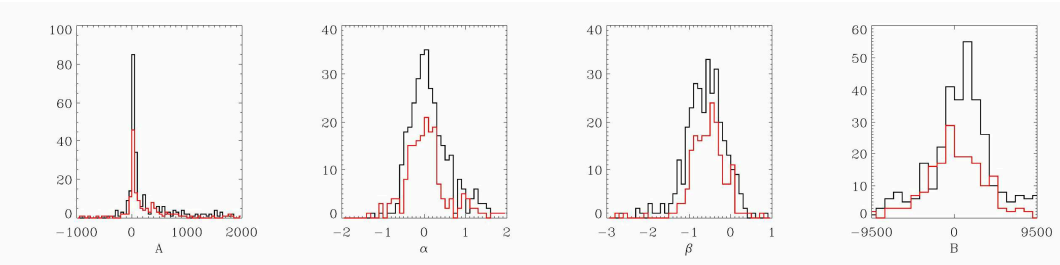

(b)

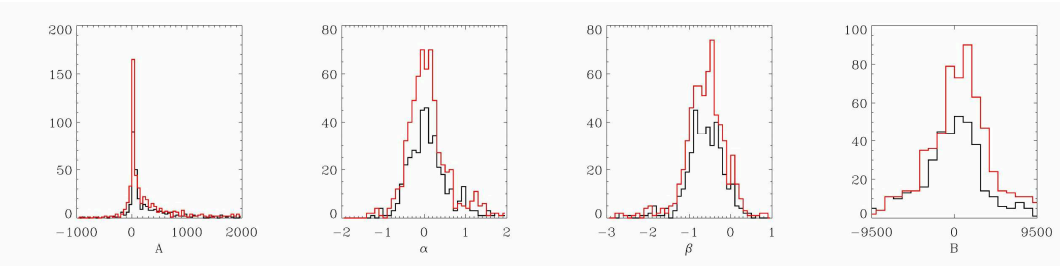

(c)

Figure 3.8: Convergence results for the fitting function 3.3. Each row of plots reports the four free parameter distributions in the order **A**, α, β and **B**. Row (a) is relative to QSH intervals with magnetic dynamics of first and second typologies, in black and red respectively. Row (b) is referred to magnetic dynamics of third and fourth typologies, again in black and red respectively. The four typologies of magnetic dynamics are described in paragraph 3.2. Finally row (c) shows the differences between the distributions for QSH intervals in absence (black) or in presence (red) of OPCD operations.

adopted to estimate the gradient together with a too low resolution: in this way DSXC can give only discrete $r_{\nabla T_e}$ values, actually, an almost constant one. The last observation implies the impossibility of any further analysis concerning the barrier position.

With these analysis we can asses the fact that the gradient magnitude is influenced mainly by the amplitude of the secondary modes, once the QSH regime is achieved. This outcome is confirmed even if the database is split in various categories: different characteristics in QSH formation, shot methodology or kind of subinterval considered in the QSH regimes. In all cases, the spread on the results does not allow to identify small variation between these categories.

3.4 The coefficient of thermal electron diffusivity

Usually the computing of the electron heat diffusion coefficient (χ_e) relative to a plasma region is a binding quest. In this paragraph we will develop a basic model able to compute χ_e at the internal transport barrier (ITB). The model is then applied to the entire database and, in analogy to previous analysis (see either [24], [62] or [61]), relations between the diffusion coefficient and the amplitude of the magnetic modes are investigated. In this case we will limit our study to secondary modes assuming that the transport mechanism, which weakens the ITB, is mainly due to the residual magnetic chaos.

The model used here is mono-dimensional and thus equation 1.44 can be used to define the electron heat diffusivity χ_e; in this case $\mathfrak{Q}$ is the power exiting the region inside the Internal Transport Barrier (ITB). The last term is better defined in the following equation:

$$\mathfrak{Q} = P_\Omega - \frac{\partial U}{\partial \mathrm{t}} \tag{3.6}$$

where P_Ω is the Ohmic heating power introduced in the plasma inside the ITB and U is its internal energy ($\int_{\mathrm{ITB}} \mathrm{d}v\ 3/2 \mathrm{n_e} T_e$). In equation 1.44 the gradients (∇T_e) are obtained with the method described in 3.1 (incremental ratio between subsequent points). In the model the density is assumed to have a flat profile with a value given by the interferometer central chords.

Computation of $\mathfrak{Q}$, composed by two terms, is less immediate and some hypotheses are necessary. For simplicity's sake we suppose that the region internal to the ITB has a D-shape with the inner line passing through the center of the camera; moreover, the curve part of the perimeter, which is half of a circle, has a radius determined by the position of the ∇T_e in the DSXC temperature profile. Using this hypothesis together with the temperature profile returned by DSXC, we can easily compute the internal energy U and its time derivative $\partial U/\partial \mathrm{t}$.

Following a standard power deposition profile from $\mu\&p$ model [27], the Ohmic power is assumed to be a function on the plasma radius in the form $1 - r^{1.5}$. A cor-

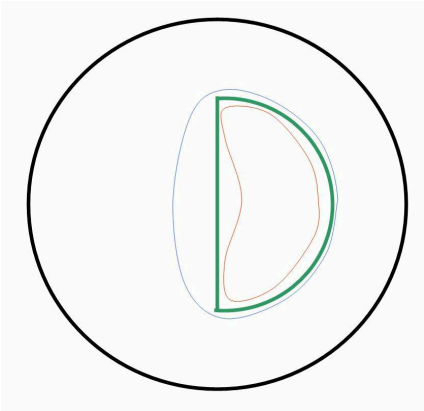

Figure 3.9: Poloidal section illustrating the D-shape region used to estimate $\mathfrak{Q}$, the power exiting through the ITB. The three curves represent: the edge of the ITB region as expected in DAx configuration, shown in red; the edge of the same region in SHAx configuration in blue and, finally, in green is the D-shape region considered during this analysis.

rection of the plasma resistivity based on a Spitzer dependence on the temperature, though implemented, was beyond the purpose of the model and finally not adopted.

Once the characteristics of the Ohmic power heating are defined, the contribution P_Ω in equation 3.6 can be easily computed. Anyway, it is interesting to note that the comparison of these two last terms tells us that the contribution given by $\partial U/\partial$t is $\leq$10% of P_Ω and thus it can be neglected.

The model described can be applied to the entire database in order to find the dependence of χ_e from the secondary modes amplitude.

$$\chi_e = \mathbf{K} \cdot b_{sec}^{\gamma} + \mathbf{C} \tag{3.7}$$

In analogy with the previous fit, equation 3.7 is fitted on all the QSH intervals separately. The distribution of the exponent γ from the fits is shown in figure 3.10(a) while those of the other two parameters is shown in 3.10(b).

The resulting distribution of γ says that if the model parameters change, χ_e does not vary in an appreciable way as its scaling results in a slightly positive exponent ($0.1< \gamma <0.4$). This result is quite different from the value of 2 expected from the analysis in [24], which are obtained in a totally stochastic regime, similar to MH states. Despite the high dispersion of the sample and the model approximations (especially in th P_Ω term evaluation), the difference is significant and suggests that, in QSH regimes, besides magnetic chaos other contributions to the electron heat transport in the core can become important.

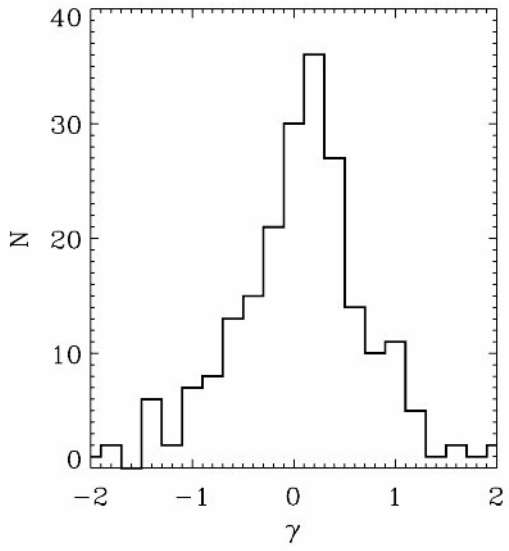

(a)

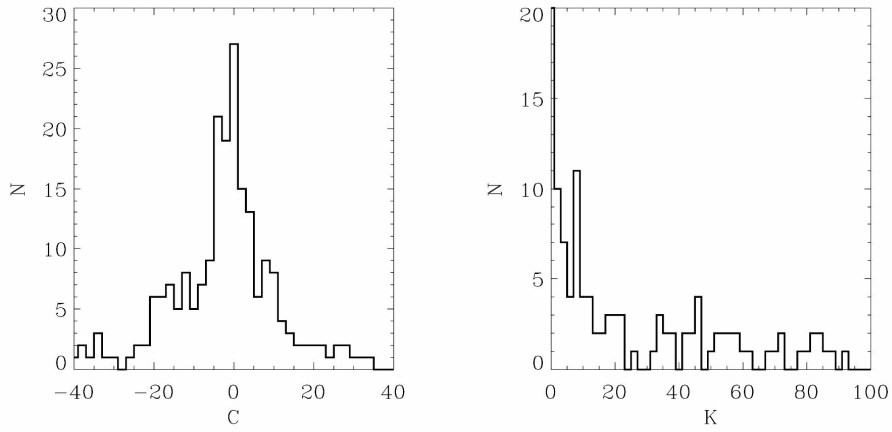

(b)

Figure 3.10: (a) Convergence results for the fitting function 3.7. The plot shows the distribution of γ, which is the exponent of the secondary modes. (b) distributions of **K** and **C**, parameters of the fitting function reported in 3.7

CHAPTER 4

SXR emissivity estimation and T_e profile mapped in helical flux coordinates

As stated in paragraph 2.2, high time resolved measurements of SXR emissivity on a poloidal section from the plasma is not provided only by DSXC, but also from the tomography diagnostic (DSXT).

Typically the data coming from this diagnostic are interpreted by the Cormack method which is based on the decomposition in periodic functions [46]. This method works well in axi-symmetric states since the reconstruction is a sum of radial and angular components which decompose the emissivity, but this characteristic makes it unsuitable to describe other plasma configurations, such as those with an asymmetrical core, like SH or QSH regimes, where a helical magnetic axis is present.

Paragraph 4.2 describes an approach to reconstruct the emissivity, keeping into account the plasma magnetic topology which is obtained by the computation of the helical flux coordinates (see paragraph 4.1) performed by the SHEq code.

Besides the improvement in the tomographic method, the plasma topology reconstruction is useful for a better interpretation of the *two foil* temperature estimation: as mentioned in paragraph 2.2, the *two foil* method does not allow to determine the localization of the T_e measurement, but once the plasma topology is computed this problem can be solved with the method exposed in paragraph 4.3.

The remapping of the temperature profile, applied to the DSX3 diagnostic, will be used in the next chapters to investigate the presence and the behavior of thermal transport barriers during the helical regimes. In this investigation it is important to estimate the ∇T_e; this topic will be developed in paragraph 4.4. Moreover, subsection 4.4.1 introduces the new coordinates $\langle r \rangle$ and X, which are useful to compare temperature profiles coming from different plasma equilibria.

Finally, the tools developed in paragraphs 4.2 and 4.3 (the map of the magnetic

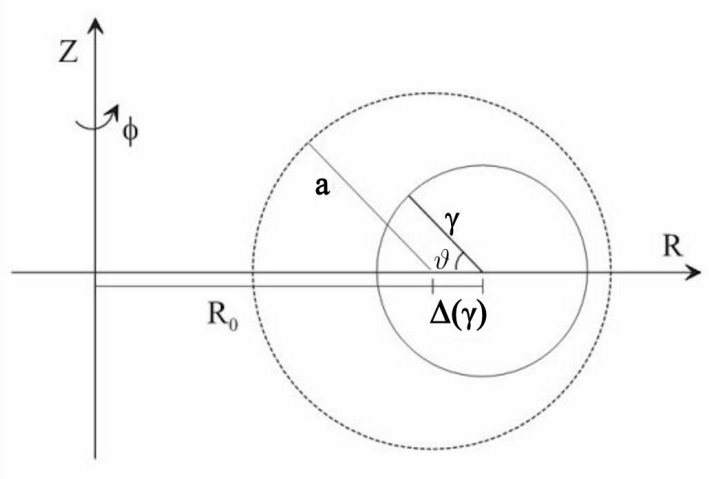

Figure 4.1: Definition of the *geometric coordinates* (γ, ϑ, ϕ).

topology, the program for the numeric line integration and the temperature remapping) are used in paragraph 4.5 in order to estimate the emissivity profile. For this new computation we assume that the plasma emissivity depends only on its temperature. Then we estimate the enhancement factor profile, introduced in section 2.3, comparing the emissivity profile described in paragraph 4.2 with the new one, which does not take into account the impurities contribution.

4.1 Flux coordinates in SH states

In a RFP, the magnetic flux surfaces of an unperturbed equilibrium can be described by the so called *geometric coordinates* (γ, ϑ, ϕ) (figure 4.1), which are related to the cylindrical one (R, Z, ϕ) by:

$$R = R_0 - \gamma \cos\vartheta + \Delta(\gamma) \tag{4.1}$$

$$Z = \gamma \sin\vartheta \tag{4.2}$$

In QSH regimes the geometrical set of coordinates (γ, ϑ, ϕ) is no more suitable and the magnetic topology must be described by the new set of *helical flux coordinates* [63]. These are defined as:

$$\chi = (\psi_{0,P} - 7\cdot\psi_{0,T}) + (\psi_{7,P} - 7\cdot\psi_{7,T}) \cdot \cos\left(\tilde{\vartheta} - 7\cdot\phi + \eta\right) \tag{4.3}$$

$$\tilde{\vartheta} = \vartheta + \lambda(r,\vartheta) \tag{4.4}$$

where χ is the new radial helical flux coordinate; $\psi_{0,P}$, $\psi_{0,T}$ are the unperturbed poloidal and toroidal magnetic flux components respectively; $\psi_{7,P}$ and $\psi_{7,T}$ are the

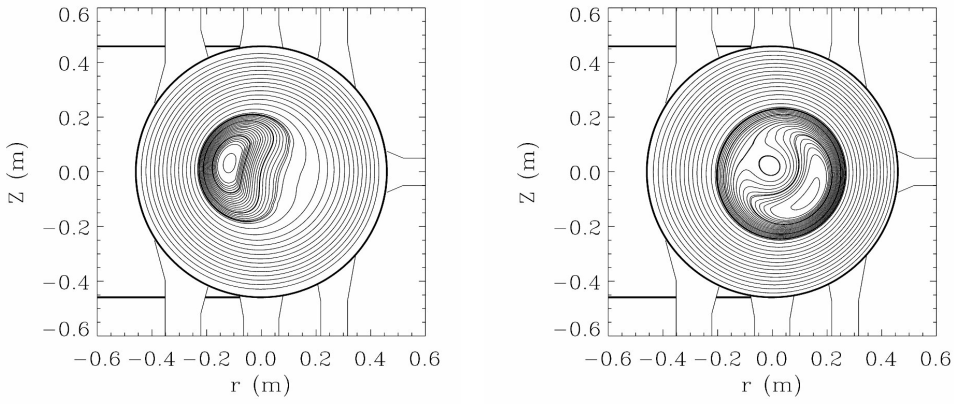

Figure 4.2: Maps of the radial helical flux coordinate ρ provided by SHEq code. While panel (a) shows a SHAx case, in panel (b) is still visible the second axis at the center of the section due to the presence of the separatrix (DAx case).

perturbed poloidal and toroidal magnetic flux components (the perturbation considered has periodicity (1,-7)); ϕ is the toroidal angle and η is a phase. Equation 4.4 defines the poloidal helical flux angle $\tilde{\vartheta}$, where ϑ and r are the standard poloidal angle and radius defined in figure 4.1; $\lambda(\gamma,\theta) = \nu(\gamma,\theta)/\psi'_{0,T}(\gamma)$ (prime denotes the derivation with respect to γ) is the transformation function obtained with the standard procedure for introducing the flux coordinates as it is clearly described in [64].

In the following the normalized radial helical flux coordinate ρ will be used instead of χ. It is defined as:

$$\rho = \sqrt{\frac{\chi - \chi_0}{\chi_a - \chi_0}} \tag{4.5}$$

where χ_0 is the helical flux at the helical axis and χ_a is the helical flux at the edge, consequently ρ will vary from 0, at the helical axis, to 1, at the edge.

The code used to obtain the magnetic topology is called **SHEq** [63]. An example of the reconstruction of ρ on a poloidal section is shown in figure 4.2. Panel (a) reports a DAx case, where either the O-point and the original magnetic axis are still visible whereas panel (b) reports a case in which the separatrix has been expelled. The code SHEq can reproduce both SHAx and DAx equilibria, though particular attention must be used in DAx cases in order to keep into account the fact that the function $\rho(r)$ is not invertible.

4.2 Emissivity profile determination method

This paragraph explains the method developed for the computation of the plasma emissivity from the tomography brightness data.

First we report some details concerning the Cormack method, which is usually employed to solve the Radon equation (formula 2.1) and get the tomographic inversion. In this approach emissivity and brightnesses are expanded in a truncated Fourier series. The expansion uses the cylindrical geometry and hence it takes the following form:

$$\epsilon(r,\theta) = \sum_{m=0}^{M} \left[\epsilon_m^c(r)\cos(m\theta) + \epsilon_m^s(r)\sin(m\theta)\right] \tag{4.6}$$

$$f(p,\phi) = \sum_{m=0}^{M} \left[f_m^c(p)\cos(m\phi) + f_m^s(p)\sin(m\phi)\right] \tag{4.7}$$

where (r,θ) and (p,ϕ) are the coordinates on the poloidal section defined in figure 2.4(b), finally ϵ and f are the emissivity and brightness, respectively. Cormack proved that between the Fourier components in formula 4.6 and in formula 4.7 the follows relations hold:

$$\epsilon_m^{c,s}(r) = -\frac{1}{\pi}\frac{\mathrm{d}}{\mathrm{d}r}\int_r^a \frac{f_m^{c,s}(p)T_m(p/r)r\mathrm{d}p}{p\sqrt{p^2-r^2}} \tag{4.8}$$

$$f_m^{c,s}(p) = 2\int_p^a \frac{\epsilon_m^{c,s}(r)T_m(p/r)r\mathrm{d}p}{\sqrt{r^2-p^2}} \tag{4.9}$$

where $T_m(p/r)$ is a Chebyshev function of the first type (it is defined as $T_m(x) = \cos(m\cdot\arccos(x))$). With some manipulations, the relation (4.9) can be simplified into a matrix equation, which is solvable [47, 48].

Before starting the analysis another important property of emissivity has to be highlighted. As reported in paragraph 1.4, during helical states the chaotic drift of magnetic field lines is limited by the rise of Cantori layer which are expected to limit the diffusion of energy in radial direction, but not along the other two dimension (tangential and toroidal). Consequently, most plasma features will depend on helical flux coordinates, especially on the radial one ρ; namely, we can write temperature and density as $T_e(\rho)$ and $\mathrm{n_e}(\rho)$, respectively. Also emissivity will then depend on ρ and its expression will become:

$$\epsilon(\rho) = K\,\alpha\,\mathrm{n_e^2}(\rho)\cdot\frac{\mathrm{e}^{-E/T_e(\rho)}}{\sqrt{T_e(\rho)}} \tag{4.10}$$

The method of emissivity estimation, but also of temperature remapping that will be reported later, are based on this assumption.

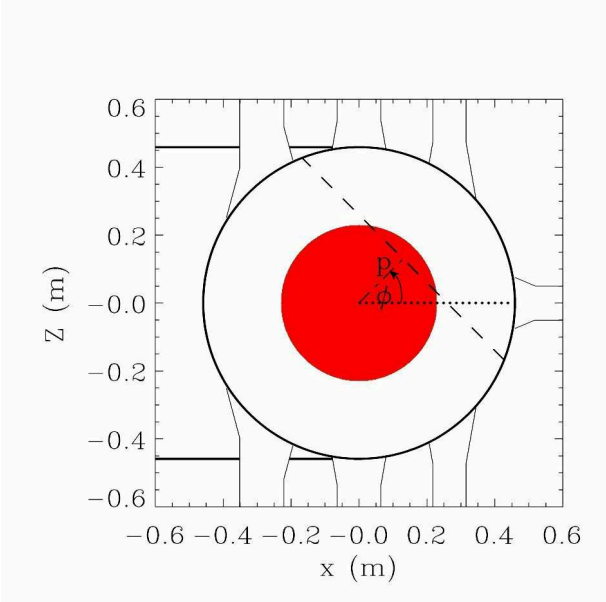

Figure 4.3: The coordinates used to define the line of sight geometry in the poloidal section: p is the impact parameter and ϕ the impact angle. Moreover, also the test emissivity used to test the numerical integrator is shown: the red disk represents the non-null zone.

4.2.1. The algorithm

This paragraph illustrates the details of the algorithm developed to estimate the SXR plasma emissivity.

The method uses a numerical integration in order to estimate the brightness from a given emissivity profile and topology of the plasma. It modifies, with an iterative cycle, the initial emissivity profile by comparing the estimated brightness and the experimental one, until a convergence occurs.

In order to estimate the brightness, this algorithm requires a subroutines that performs a numerical path integral along a line with a specified geometry for a given emissivity map. We have chosen to define the emissivity map of the poloidal section as a square grid. The program identifies the points of the grid intercepted by the chord and then it computes the path integral.

In order to test the path integral algorithm, a test emissivity map, characterized by a simple shape, has been considered. The chosen map has zero value in every point but in a disk centered in the origin. The test emissivity is shown in figure 4.3 and is defined by the following formula

$$\epsilon(x,y) = \begin{cases} 0 & \text{if } \sqrt{(x^2+Z^2)} > r \\ 1 & \text{if } \sqrt{(x^2+Z^2)} \leq r \end{cases} \tag{4.11}$$

where r is the disk radius.

In this case an analytical solution of the path integral can be computed. In fact the chord on the poloidal plane $c(l)$, where l is the coordinate along the line of sight, has the (x, y) coordinates defined as:

$$y = \frac{\mathrm{p} - x\cos(\phi)}{\sin(\phi)}, \tag{4.12}$$

where p and ϕ are the chord parameters and their definition is reported in figure 4.3. Thus, with the emissivity definition reported in equation 4.11, the path integral results:

$$f(r, p, \phi) = \int_{|c(l)|<R} \mathrm{d}l\, \epsilon(c(l)) \|c'(l)\| = \int_a^b \frac{\mathrm{dx}}{\sin(\phi)} \tag{4.13}$$

In the last passage of equation 4.13, a and b are the x coordinates where the chord intercepts the disk border of the emissivity map. They are defined as $\mathrm{p}\cos(\phi) \pm \sqrt{\sin^2(\phi)(r^2 - p^2)}$.

In table 4.1 the relative errors of numerical integrations along the same chord are reported, they correspond to different emissivity map resolutions. The grid has the same length of the diameter of the experimental poloidal section width.

resolution	relative error
51x51	0.08
101x101	0.03
151x151	0.03
201x201	0.002
251x251	0.03
301x301	0.0012
351x351	0.0015
401x401	0.017
451x451	0.003
501x501	0.0007

Table 4.1: the chord parameters are $p = 0.1836$m and $\phi = 45$ degrees, while the emissivity disk has radius 0.2295m.

As a result of this analysis a map with 501x501 points resolution has been chosen. Such a resolution keeps the relative error on the integration below 0.1% while the computing time is still acceptable. Note that, with this resolution, the physical distance between two points in RFX-mod of this map is 1.8mm.

In order to simulate the brightness with a given magnetic topology, we have first to compute the map of ρ, then define the emissivity profile $\epsilon(\rho)$ and finally use the numerical integration described before. Once the magnetic topology map

is computed and the emissivity profile is chosen, it is possible to determine the brightness for all the chords.

Since the experimental poloidal section is circular while the emissivity map is square with the side dimension equal to the chamber diameter, a condition has been imposed in the algorithm in order to exclude the regions outer the chamber in the path integral computation.

As next step the convergence of the emissivity profile can be performed. With this purpose the IDL procedure *curvefit* has been used. This function uses the Newton method in order to minimize the χ^2 from an initial set of parameters.

In order to describe the emissivity profile by a parameters set, different approaches have been tested. First the function

$$\epsilon_{\alpha,\beta}(\rho) = A \cdot (1 - \rho^{\alpha})^{\beta} + B \tag{4.14}$$

has been used, where the parameters are four: A, B, α and β. The low number of free parameters allows a fast convergence, but the simple shape of the function can not reproduce the experimental brightness in a great number of cases.

Since a good convergence was not systematically possible with this kind of profile, a polygonal line has been used. By this approach the parameters are the emissivity values corresponding to polygonal vertex coordinates. Although typically the convergence on the brightness was good, the resulting emissivity profiles had unphysical features like negative emissivity, great oscillations and high values at the edge.

In order to avoid unphysical results, in the following $\epsilon(\rho)$ is described using the derivative values $\epsilon'(\rho)$ in defined intervals of ρ: in this way the ϵ profile is reconstructed step by step starting from the edge (where emissivity is assumed to be 0). A further constraint to impose is $\epsilon'(\rho) \leq 0$ which means a monotonically decreasing $\epsilon(\rho)$ profile. At last we have imposed an emissivity profile always positive, monotonically decreasing and with the edge value equal to 0. The rapid convergence is assured using only nine intervals in the emissivity profile and fixed interval dimensions.

The results obtained from this convergence algorithm is reported in the following subsection.

4.2.2. The convergence results

The first comparison reported between the three types of the emissivity profiles is the paradigmatic case of the shot 31541 at 49 ms.

The statistical χ^2 resulting from the convergence with the analytical curve is equal to 3.1 and the time of convergence is 4.7 seconds. As visible in figure 4.5(a) the emissivity profile has negative values at the edge.

In order to compare the three types of profiles introduced in subsection 4.2.1, the convergence for each of them has been performed for the shot 31541 at 49ms.

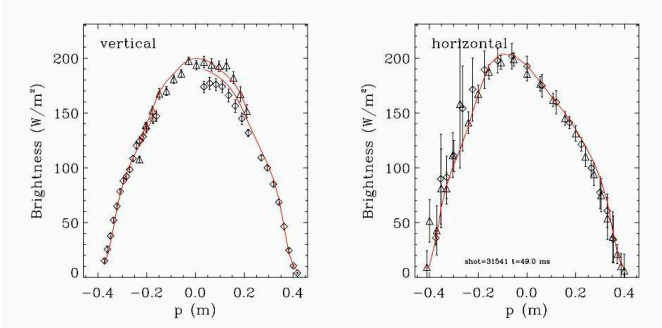

(a) analytical profile

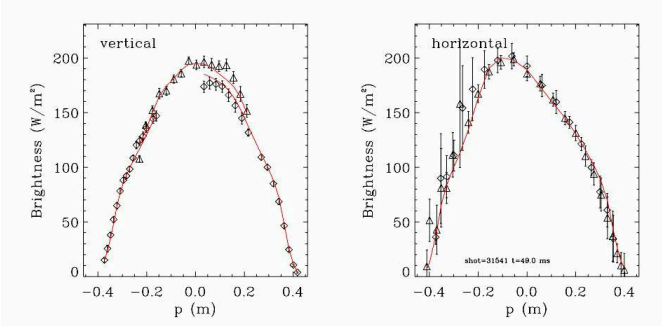

(b) polygonal line

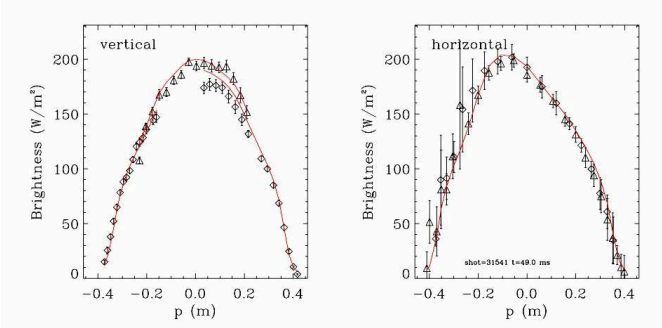

(c) monotonic polygonal line

Figure 4.4: The brightnesses simulated using the profile obtained by the convergence algorithm explained in 4.2.1. In black are shown the experimental data, relative to the shot 31541 at 49ms, while in red are the simulated one. In (a) are shown the brightnesses resulting from the convergence with the analytical function written in 4.14. In (b) the polygonal line has been used while in (c) the same polygonal line but imposed the monotonicity and the zero value at the edge has been used.

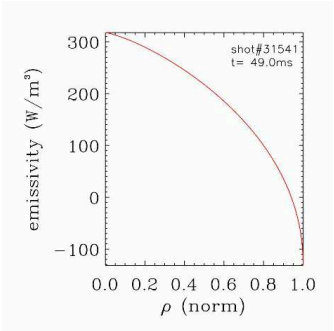

(a) analytical profile

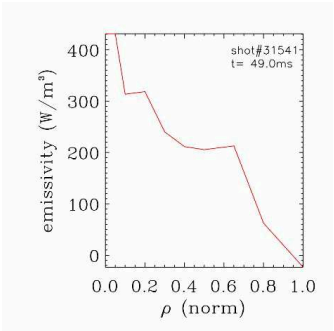

(b) polygonal line

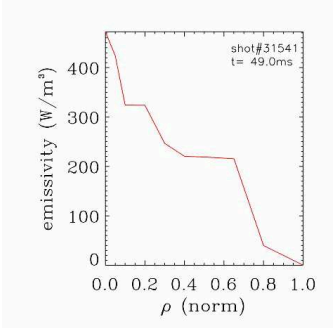

(c) monotonical polygonal line

Figure 4.5: The emissivity profile obtained by the convergence algorithm described in 4.2.1 for the shot 31541 at 49ms. The analytical profile defined in 4.14 is shown in (a) while in (b) there is the polygonal line. In (c) the polygonal line with the monotonicity and the zero edge value conditions is shown.

The resulting brightnesses are shown in figure 4.4 and the corresponding emissivity profiles in figure 4.5. The polygonal curve (figure 4.5(b)) results more accurate with a χ^2 equal to 1.2 but with a longer time of convergence of 5.2 seconds. The curve is slightly negative beyond $\rho \sim 0.9$. The performance of the polygonal curve with monotonicity condition lies in the middle with a χ^2 equal to 2.1 and a time of convergence of 28 seconds. The shape of the emissivity profile, shown in figure 4.5(c), is close to the simple polygonal line, but, as expected, there is no negative emissivity and $\rho \sim 0.6$, $\epsilon'(\rho)$ has not positive values.

For a statistical analysis, the comparison has been extended to several other cases (about 8500 convergences). They have been selected during QSH regimes in discharges with plasma current between 1.2MA and 1.8MA. The behavior obtained in this statistical analysis is similar to the one shown before. Figure 4.6(a) shows the distributions of the statistical χ^2 for the three profiles: red is the analytical function, green is the polygonal curve and blue is the monotonic polygonal curve. As it can be seen, the χ^2 values are higher for the analytical function and lower for the simple polygonal line. Between the two lines there is the monotonic one. Such big deviations from 1, the statistical expectation value of χ^2, are not only due to the limits imposed to the model of the emissivity profile, but mostly to the reconstruction of ρ.

The distribution of the convergence times is reported in figure 4.6(b); also here the color red identifies the analytical function, the green the polygonal line and blue the monotonic polygonal line. According to the case considered before, the analytical curve and the polygonal line have similar convergence times, about 5 seconds, on the contrary, the monotonic polygonal line requires a longer time, often even more than 40 seconds.

In figure 4.7 a comparison, in a QSH case, between the outputs of classical tomography and of the new method is reported. According to paragraph 2.3, panel (a) is computed using the Cormack method whereas panel (b) is obtained from the emissivity profile, reported in figure 4.5(c), applied to the corresponding map of ρ. In panel (a) the helical structure can be clearly identified just above the camera axis, on the other hand, cylindrical geometry is still visible. Inversion in panel (b) reconstructs the shape of the magnetic helical structure without problems.

4.3 T_e mapping method

The determination of the plasma emissivity can take advantage of the use of the magnetic topology reconstruction, as explained in paragraph 4.2. In a similar way, the magnetic topology reconstruction can be used to estimate the actual location of the temperature measurements obtained by the SXR diagnostic. In fact, as mentioned in paragraph 2.2, the temperature obtained by the SXR *two foil* diagnostics is not a local value.

This problem can be overcome if, besides the temperature data, the magnetic

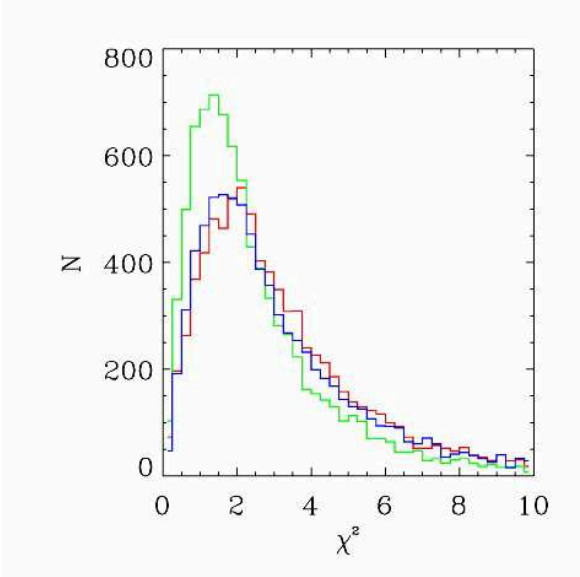

(a)

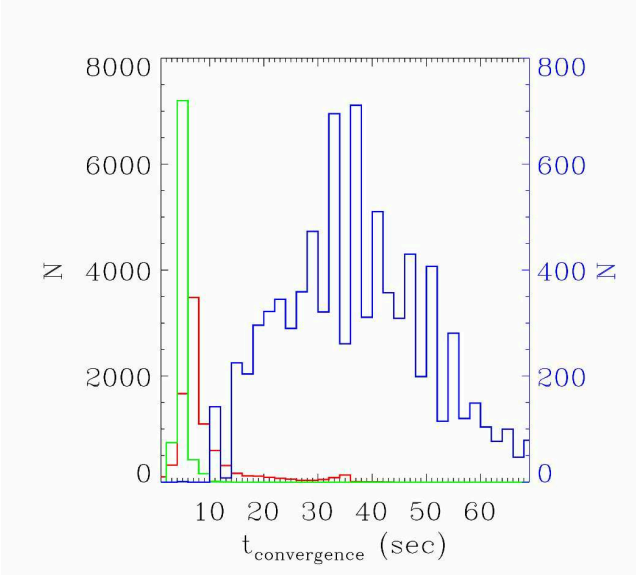

(b)

Figure 4.6: (a) Distributions of statistical χ^2 for the convergences of the emissivity profile: red is the convergence with the analytical function, green is the polygonal line and in blue is the monotonic polygonal line with the imposition of zero value at the edge. (b) Distribution of the time of convergence for the three kind of profile: red is the analytical function, green is the polygonal line and blue is the monotonic polygonal line. The blue curve is related to the right ordinate axis.

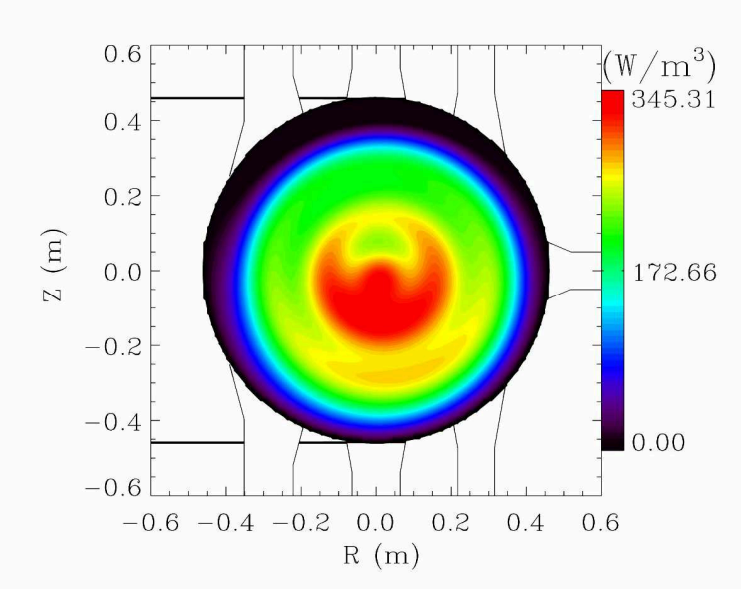

(a)

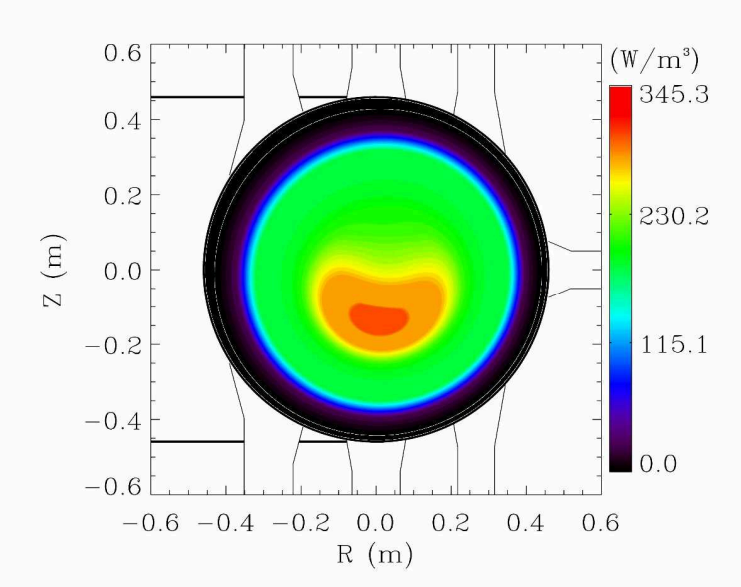

(b)

Figure 4.7: Comparison between classic tomography and new emissivity estimation method. (a) shows the emissivity reconstruction on the poloidal section using the Cormack method and the expansion in cylindrical harmonics of the emissivity. (b) shows the emissivity profile, obtained with the convergence method discussed above, applied to the map of ρ.

topology is considered. The procedure is based on the fact that the brightness collected along a line of sight, described by equations 2.2 and 2.1, depends mainly on the plasma volume with the highest temperature since it gives the most relevant contribution to the brightness. In other terms, volumes characterized by low temperatures are negligible. This implies that the *two foil* technique estimation is close to the maximum temperature along the line of sight. Moreover, during states characterized by helical topology, and thus by a higher magnetic order, the temperature and the emissivity can be considered as functions of the helical flux coordinates and, in particular, of the radial coordinate ρ.

In order to map the temperature we will assume that the estimation obtained with a *two foil* device is equal to the maximum T_e intercepted along the line of sight, that depends only on ρ, and that the temperature grows from the edge to the helical axis, i.e. that at lower ρ is the plasma is hotter.

According to these assumptions, the electron temperatures estimated with the *two foil* device is associated to ρ values and thus also to the corresponding flux surfaces. The trend of ρ along the line of sight is found implementing its geometry on the map of ρ, computed in paragraph 4.2, thus the minimum value of ρ is determined and associated to that line of sight. Once this procedure is applied to every line of sight the profile $T_e(\rho)$ is obtained. It is worth noting that two lines of sight can be associated to almost the same ρ, especially when they lie on different sides of the helical axis.

An example of T_e profile, obtained with the DSX3 diagnostic, is shown in figure 4.8(a). DSX3 temperatures are shown with the solid circles (blue) and squares (red); the two shapes (and colors) distinguish the two sides of the plasma in relation of the magnetic axis.

To validate the procedure it is useful to compare the T_e profiles from DSX3 with an independent measure, for example with the Thomson Scattering (TS) data. The comparison is possible if the two temperature measurements are mapped on the same coordinate (ρ). We can use again the map of ρ, considering its profile function along the trajectory of the TS laser this allows to determine the values of ρ relative to the TS measurement positions and finally to remap the T_e as the ρ coordinate. For this determination the map of ρ has been computed at the toroidal angle of the TS diagnostic in order to take into account the toroidal periodicity of the dominant magnetic mode. The TS profile versus the ρ coordinate is also reported in figure 4.8(a) with the empty magenta circles and cyan squares. It can be seen from this plot that the two side of the TS profile are well superimposed one over the other and the profiles of the two diagnostics are almost overlapped confirming the goodness of the mapping method and the consistency of the two diagnostics.

According to the paragraph 2.2, the two diagnostics will not have always a perfect agreement, in fact, as the DSX3 diagnostic process line-integrated measurements, when the hot region has a limited extent the estimated temperature may be too low. This is the case of the DAX states and an example of the temperature

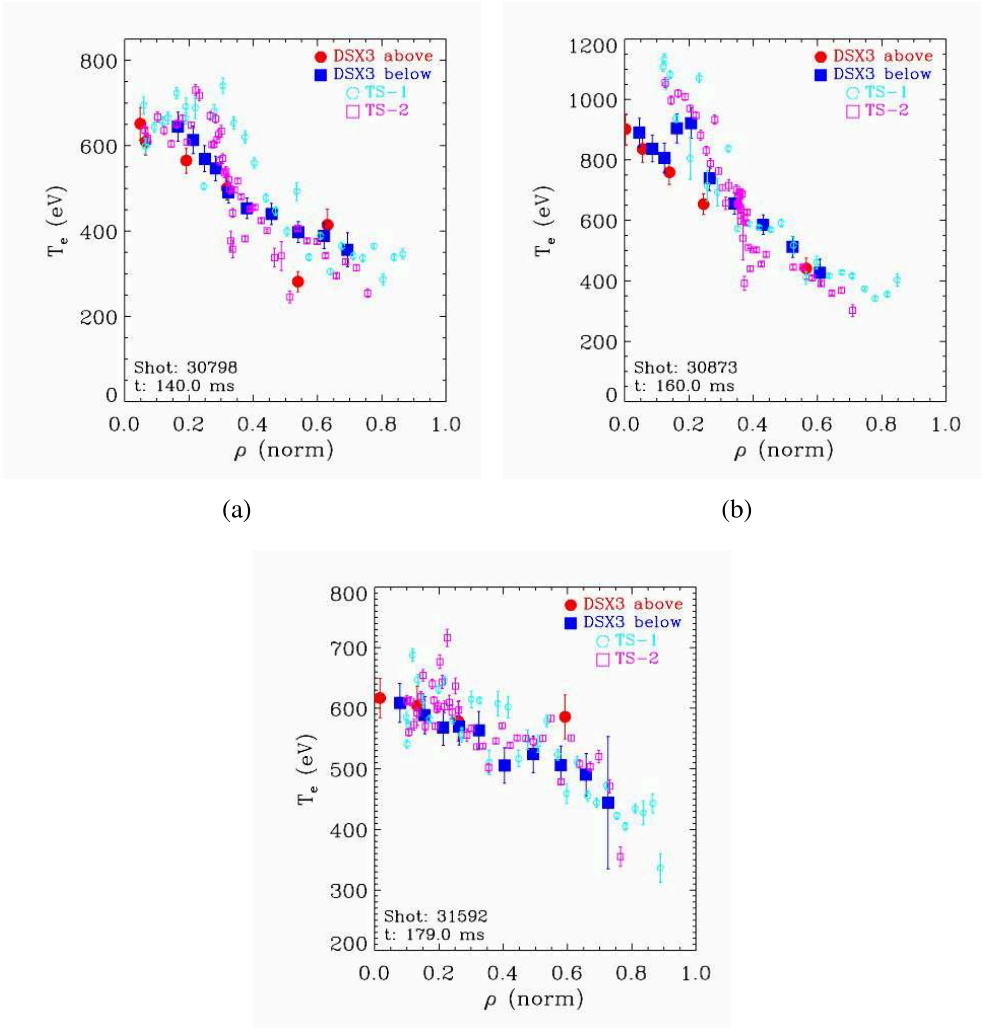

(a) (b)

(c)

Figure 4.8: Remapped temperature profiles. (a) SHAx case, (b) DAx case and (c) MH case: solid points are related to temperatures obtained with the DSX3, the red dot and the blue square distinguish the side of the helical structure. Empty points are for TS measurements, also here the shape (circle or square) and the color (cyan or magenta) change according to the side of the structure considered.

profiles is reported in 4.8(b). This picture shows that the DSX3 can resolve small structures although their maximum temperature is underestimated. For the sake of completeness we report in figure 4.8(c) the temperature profile relatives to a MH state.

The comparison of the two diagnostics can be seen from a different view remapping the DSX3 temperature measurements on the TS trajectory. The profiles shown before in figure 4.8 remapped on the TS trajectory are reported in figure 4.9

4.4 Estimate of the maximum gradient and its location on the temperature profile

Transport barriers are identified on the temperature profile as those regions with high value of temperature gradient. We show in this paragraph the method developed to estimate it by introducing a new spatial coordinate. In fact, topology described by the flux coordinate ρ changes from an equilibrium to another and the comparison of the temperature profiles is very difficult. Moreover, it is normalized and thus it is unable to take into account the real physical dimension of the helical structure.

4.4.1. $\langle r \rangle$ and X coordinate definitions

To get information on the structure extension in the real space we first define the coordinate called here *average radius* ($\langle r \rangle$). It is the radius of a circle equivalent in area to the corresponding flux surface in the poloidal section. It can be defined by the equation

$$\langle r \rangle(\hat{\rho}) = \sqrt{\frac{A(\hat{\rho})}{\pi}} \tag{4.15}$$

where $A(\hat{\rho})$ is the area on the poloidal section of the helical flux surface with coordinate $\hat{\rho}$. $A(\hat{\rho})$ has been estimated numerically from the map of ρ: first, the number (N) of pixels with $\rho \leq \hat{\rho}$ has been determined; then an area (a) has been associated to each pixel (a is equal the total area of the map ($4 \times 0.459^2 \mathrm{m}^2$) divided by the number of the pixels 501×501); finally $N \cdot a$ gives $A(\hat{\rho})$. An average radius has the advantage to be strictly related to the volume of the magnetic structure. Figure 4.10(a) shows an example of the temperature profile remapped in this coordinate.

An alternative way chosen to get physical information on the temperature gradient is to consider the maximum ∇T_e around the helical axis. As the distance between neighbor surfaces is not constant, the absolute value of the gradient varies along the surfaces.

It can be seen that the locus of points where surfaces are closer each other (more *packed*, corresponding to a region where ρ is steeper) is approximatively lying on a straight line that passes through the center of the axisymmetric coordinate system

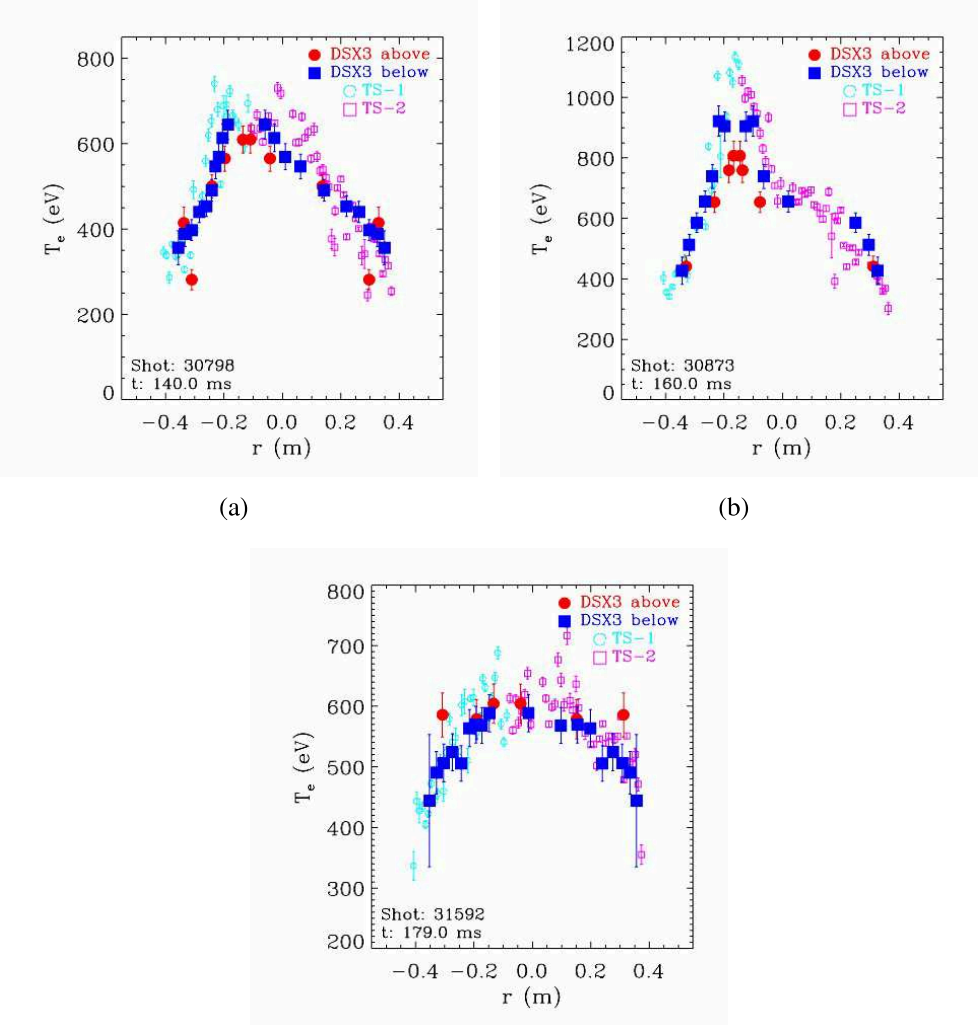

Figure 4.9: DSX3 temperature profiles remapped and plotted on TS coordinates. (a) SHAx case, (b) DAx case and (c) MH case: filled points are related to temperatures obtained with the DSX3, the red dot and the blue square distinguish the side of the helical structure. Empty points are for TS measurements, also here the shape (circle or square) and the color (cyan or magenta) change according to the side of the structure considered.

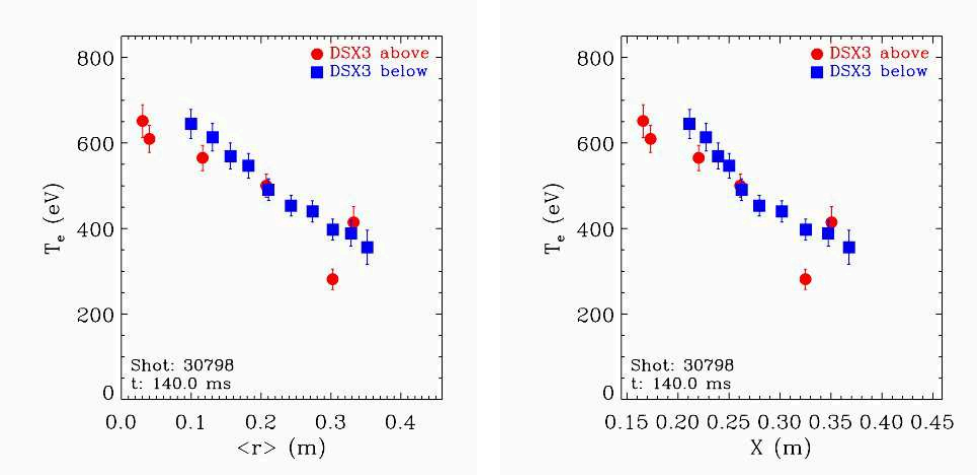

(a) (b)

Figure 4.10: (a) Remapping of the T_e DSX3 data in the $\langle r \rangle$ coordinate. (b) Remapping in X. In both panels, red dots are related to the lines of sight above the helical axis while the blue squares are for those below.

(O_A) and the magnetic axis of the helical structure (O). Such a straight line, which is shown in figure 4.11 (dashed line), crosses each flux surface in two points, with the notable exception of the O-point. The X coordinate is defined as the distance from O_A of a point along the line. The direction of X is chosen in such a way that the coordinate $X_{O-point}$ of the O-point of the magnetic structure has a positive coordinate. Given this choice, the region of points along the line where surfaces are closer is characterized by coordinates $X > X_{O-point}$. The arrow in figure 4.11 shows the coordinate X of the T_e data point measured along the line of sight tangent to the selected flux surface (highlighted by the thicker line). The $T_e(\langle r \rangle)$ profile of figure 4.10(a) becomes, as a function of the new coordinate X, the one shown in figure 4.10(b). This representation has the advantage that the slope of the curve immediately gives the local maximum gradient.

4.4.2. ∇T_e determinations

For statistical analysis it is important to develop algorithms which estimate the maximum temperature gradient and its location. As the direct computation of the gradient by simple difference between adjacent points is noisy, several smoothing techniques have been tested. A first analysis is based on a linear fit to a series of points while a second approach uses profile fit by an analytical function. For both methods, once the fit has converged, the steepest slope in the profile will give the ∇T_e value and its position.

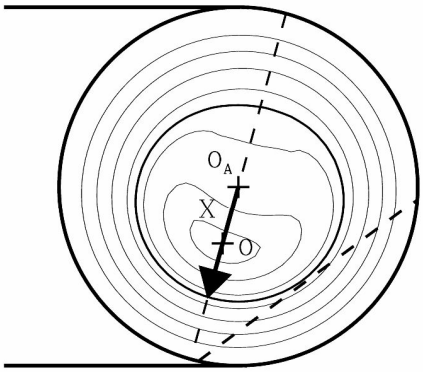

Figure 4.11: Definition of the X coordinate: it is the distance (black arrow) from the center O_A of the axisymmetric coordinate system to the opposite side of the helical flux surface highlighted with a thicker line. O is the O-point of the helical structure. Dashed chord indicate a line of sight labeled by the arrow.

The first method, hereafter addressed as *linear method*, uses the linear fit over a fixed number of points of the T_e profile.

The remapping of the T_e data coming from the DSX3 lines of sight below and above the helical magnetic axis is rather good, as already shown in various panels of figure 4.8, but slight differences occur and a discrepancy still exists. This dispersion, due to an imperfect reconstruction of the magnetic equilibrium gives rise to a considerable noise in the gradient determination. It was therefore decided to use only T_e data taken either above or below the helical magnetic axis, preferring the side with the greatest number of measurements.

Linear fit is performed over a sliding window of 6 adjacent points and the evaluated gradient is assigned to the average coordinate of the points. The choice of 6 values is a compromise between spatial resolution and reduction of spatial oscillations.

Figure 4.12(a) shows all of the ∇T_e estimate, highlighting the steepest one.

The second method adopted, called hereafter *tanh method*, fits all the profile points with the function:

$$T_e(X) = A_0 \tanh\left(A_1 \left(X - A_2\right)\right) + A_3 \tag{4.16}$$

where A_0, A_1, A_2 and A_3 are the free parameters of the fit.

To account for of the errors of the magnetic topology reconstruction different weights are assigned to points located on different sides of the o-point: those on

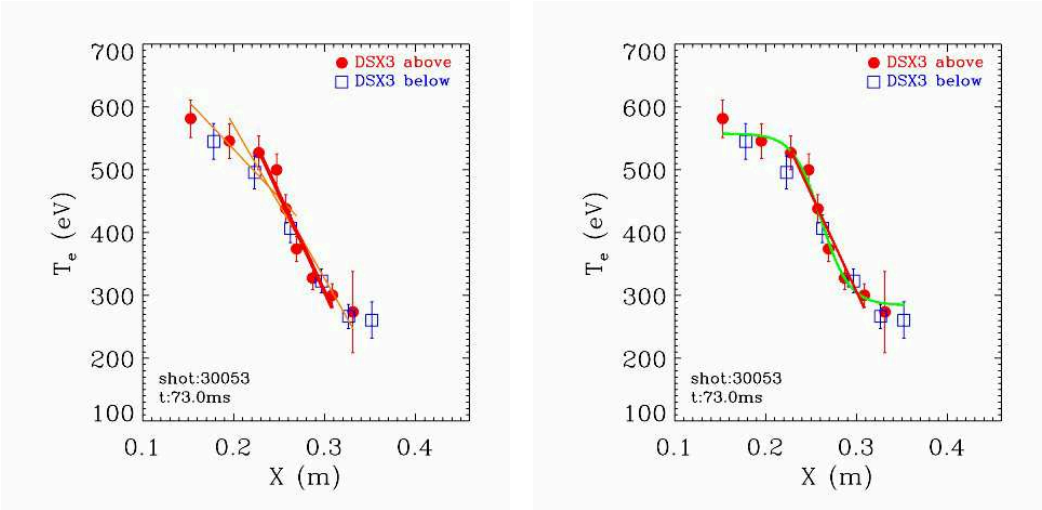

(a) (b)

Figure 4.12: Examples of ∇T_e estimation. (a) *Linear method*: the ∇T_e is the steepest slopes (red thick line) among the linear fits performed on the entire $T_e(X)$ profile (orange thin lines). The fit is performed on the red points only, which are on the side with the greatest number of measurements. (b) *Tanh method*: the function 4.16 is fitted on the entire profile (weighting double the side with the majority of the points), the ∇T_e is obtained taking its steepest slope. The plot shows the fitted function, with the green curve, compared to the chosen fit of the *linear method* (the red line).

the side with the majority of the points are characterized by a double weight in comparison to the others.

Since the procedure is based on a locally converged algorithm, some results have been rejected in order to avoid unphysical outputs. This is done by imposing conditions on the slope magnitude and dimension of the step.

Figure 4.12(b) shows, with the green line, an example of the *tanh* fit (the green curve) compared to the one based on the *linear* fit (the red line).

4.4.3. Limits of the ∇T_e determination

The limited spatial resolution of the DSX3 leads to an uncertainty in the maximum ∇T_e determination, which is related to the poloidal position of the helical magnetic axis. We want to quantify this uncertainty by simulating the measurements for different poloidal locations of the same temperature profile.

In general the smoothing effect, highlighted in the comparison between TS and DSX3 measurements for DAx configuration, may affect also the reconstruction of the temperature profile for the SHAx case. This is the reason why different type

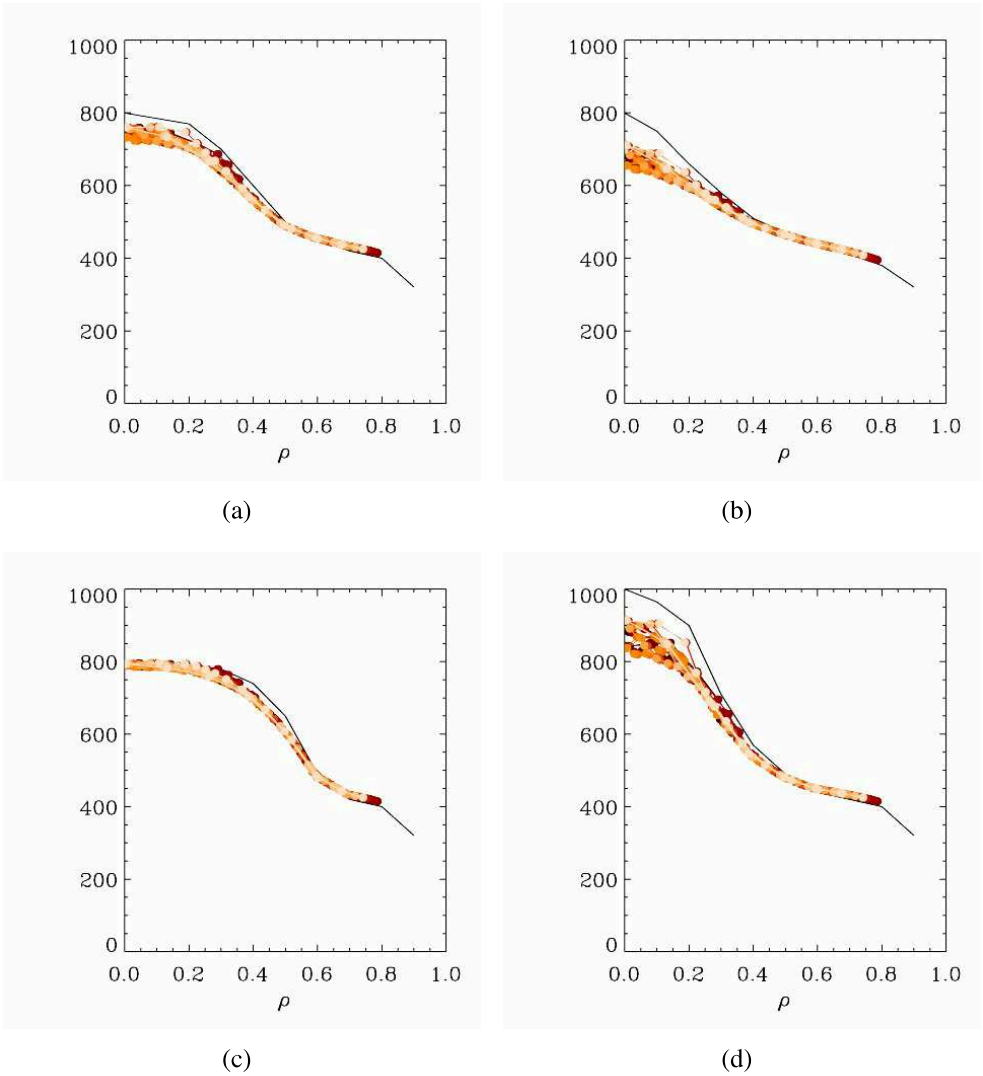

Figure 4.13: The simulated temperature profiles. Black lines represent the starting temperature profiles and the curves in red scale are the simulated ones for the DSX3 diagnostic. They have been estimated applying starting profiles to a single magnetic configuration rotated 16 times in the poloidal plane. Profile (a) is expected from a typical SHAx, (b) has the gradient closer to the magnetic axis, (c) has a wide thermal structure, (d) has a really steep temperature profile (expected for a DAx case).

of profiles have been used during this test. Figure 4.13 shows with the black line the four profiles used: they have the maximum gradient at different positions and with different slopes since the purpose is to verify a significant survey of possible scenarios.

All the temperature profiles have been applied to the real map of ρ shown in

figure 4.14, the map is then rotated poloidally at 16 different angles and the DSX3 brightnesses are simulated.

The method adopted to estimate the brightnesses of DSX3 is based on the formula 2.2 considering a typical density profile for RFX-mod.

Figure 4.13 reports the simulated profiles in gradation of red (16 for each panel). It can be observed that reconstructed profiles are slightly different and always lower in gradients than the original ones. Note that this effect only depends on the line averaging nature of the measurement. The magnetic equilibrium uncertainties are not included in this simulation: the same helical topology is in fact used to simulate the measurements and to remap the profile.

The algorithm is also applied to determine ∇T_e in the simulated measurements. Its dependence on the helical axis position (in abscissa) for all the simulated profiles has been shown in figure 4.15, where ∇T_e (in ordinate) have been normalized to the maximum simulated gradient: 4.15(a) shows the *linear method* while 4.15(b) shows the *tanh method*. The colors of the four curves distinguish the different profiles: red is the profile shown in figure4.13(a), blue the (b), green the (c) and brown is the (d).

It is evident that the estimated maximum gradient is always less than the real one. Moreover a variation of about 30-40% may occur, depending on the angle of the helical magnetic axis. The approximate symmetric behavior around 180°is due to the fact that the gradient is best estimated when the helical structure is located at poloidal angle approximately perpendicular to the lines of sight. Besides, the amplitude of the oscillations depends on the temperature profile type: the steeper or the inner the gradient is the bigger the oscillations are: as an example, consider in figure 4.15 red vs blue curve or the magenta vs green one. The plot tells us also that *linear method* has wider oscillations than the *tanh* one. Finally, differently from the *linear method*, the *tanh method* returns to its highest gradient values at about 0°, i.e. when the magnetic axis is exactly in front of the probe.

It is worth to note that a significant reduction of the uncertainty could be obtained by assuming to measure the temperature along lines of sight from a second fan, perpendicular to the first one. Such a diagnostic is not available for the data set that we consider for this paper but it is planned for future campaigns.

4.5 The Bremsstrahlung emissivity profile

This paragraph illustrates a procedure to compute the emissivity profile from plasma quantities, like temperature and density, in contrast to the method adopted in paragraph 4.2 that uses exclusively brightness data. The starting data of this method are the profile of T_e, obtained from DSX3 and remapped on the helical coordinate ρ, and the topology of the plasma.

The emissivity and the temperature of the plasma are linked by the formula 4.10 and thus the latter can be computed once the temperature profile and the features of the tomography diagnostic (for instance, its filters and detectors thicknesses) are

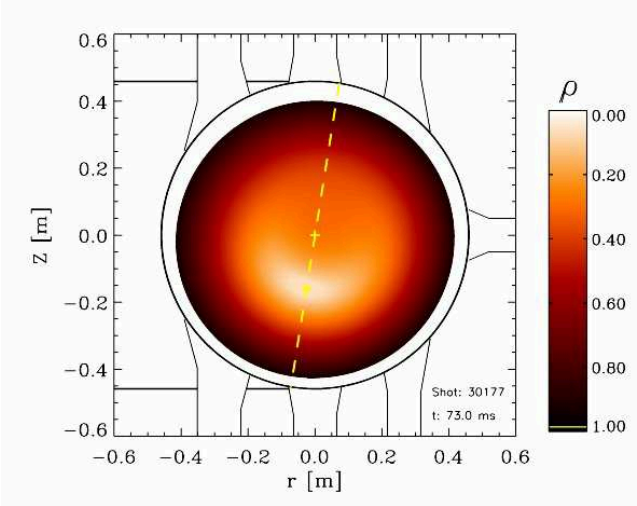

Figure 4.14: The map of ρ used to compute the simulated brightnesses of the DSX3 (at the poloidal angle of 260°). The red scale indicates the value of the coordinate and the yellow line shows the axis passing through the center of the camera and the O-point.

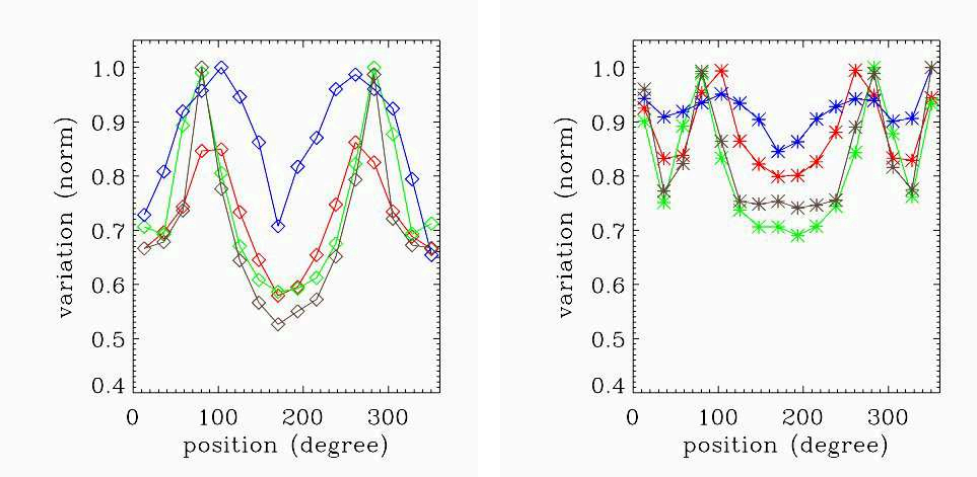

(a) (b)

Figure 4.15: Simulation results. Plots show the behavior of the ∇T_e obtained from the simulated temperature profiles of DSX3 for various poloidal angles of the O-point. Plot (a) reports the results of the *linear method* and (b) those of the *tanh*. In both panels the poloidal angles of the O-point are in abscissa while ∇T_e, normalized to the gradients of theoretical profiles, are in ordinate. Colors indicate the theoretical profile adopted: red is the profile shown in figure 4.13(a), blue the (b), green the (c) and brown is the (d).

known. The curve describing the temperature is obtained starting from the profile of T_e, which has been remapped by the method described in paragraph 4.3. The curve used to fit the points of the temperature profile is a spline similar to the monotonic polygonal curve introduced in 4.2. This means that the profile is defined by the derivative values of the temperature profile ($T'_e(\rho)$), imposed to be always negative, in chosen intervals of ρ; the reconstruction starts at the edge where temperature is assumed to be 0. For this fit the polygonal line has six vertexes which are also the constraints of the spline. Figure 4.16(a) shows the temperature profile, as usual the lines of sight above the helical axis are shown in red while those below are in blue, and the curve obtained from the fit is in magenta.

Not only the temperature profile, but also the enhancement factor K is not determined a priori and must be computed. Note that K is just a multiplying factor in formula 4.10 thus it is first sufficient to perform an integration with a standard value of K (for example 1) and then divide the experimental brightness by the computed one, the ratio gives us the value of K (in the case reported in figure 4.16(a) K is about 5). Considering vertical and horizontal arrays separately, two enhancement factors are estimated (K_v is for the vertical lines of sight, K_h for those horizontal); the lines of sight chosen to have an estimation of K_v and K_h are the longest available, which correspond to the inner ones. The curve of the temperature is now introduced in the formula 4.10 and the bremsstrahlung emissivity profile $\epsilon^{br}(\rho)$ is obtained. Figure 4.16(b) shows the emissivity profile obtained with this procedure with the blue solid line. It is compared to the profile obtained using the convergence method reported in paragraph 4.2, red solid line.

With the estimated values of $K_{v,h}$, all the brightnesses are computed and the comparison with the experimental data is shown in 4.17: the experimental data are plotted in black while the computed brightnesses are in blue. Central lines of sight show a good agreement between the experimental brightnesses and the computed one, this is consistent with the fact that the value of K is obtained using just the most central lines of sight of vertical and horizontal arrays. In contrast, the other lines of sight have a visible gap from the experimental data that grows for the external points, this may indicate variations of the enhancement factor toward the external lines of sight.

According to paragraph 2.2, the parameter K accounts for other sources affecting the emissivity, which is computed, otherwise, as pure bremsstrahlung. However, the other sources of emission are not uniform on the poloidal section of the plasma and thus the enhancement factor represents a too crude approximation. Coherently to previous assumptions a valid solution is to consider an enhancement factor profile depending on the ρ coordinate, $K(\rho)$. An estimation of $K(\rho)$ is possible if we consider the emissivity profile $\epsilon^{br}(\rho)$, which is computed using the bremsstrahlung formula, and the profile found in paragraph 4.2, which considers all the possible sources. This means that the ratio $\epsilon^{br}(\rho)/\epsilon(\rho)$ gives us the enhancement factor profile. An example of such a profile is shown in figure 4.16(b) with the dashed cyan

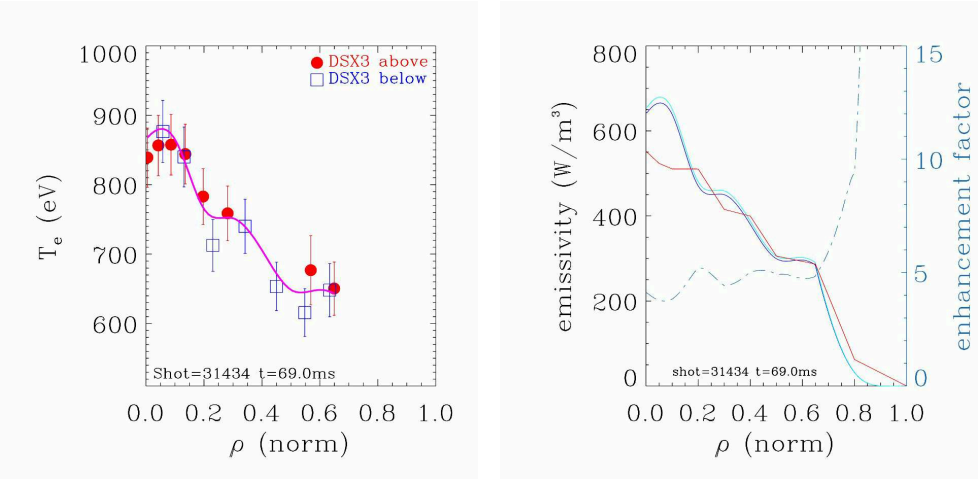

(a) (b)

Figure 4.16: (a) The temperature curve mapped in ρ. Red points and blue squares are the DSX3 experimental temperatures, different symbols are used to indicate the two sides of the magnetic structure. The fitting curve is shown in magenta. (b) Comparison of emissivity profiles as function of ρ. Blue and cyan are the profile obtained with the bremsstrahlung approximation for the horizontal and vertical arrays, respectively (the only difference between the two curves is due to the use of K_v and K_h for the vertical arrays and the horizontal one respectively). The red curve is the emissivity obtained with the convergence method discussed in paragraph 4.2. Finally the dashed line shows how the enhancement factor K varies with ρ.

line. At low values of ρ, up to $\rho \sim 0.5$, it is close to 5 while for $0.5 \lesssim \rho \lesssim 0.8$ it decreases. At $\rho \gtrsim 0.8$ the value grows very high level, but this is not surprising since the enhancement factor profile is not really defined beyond the most external point of the experimental temperature. Moreover, the impurities at the edge have higher concentration than in the core and the bremsstrahlung approximation may not be good enough.

From these results we can conclude that:

- The value of K is far from 1, according to the analysis in paragraph 2.2.
- Though in the shown case the simulated brightnesses are close to the experimental values, in many cases this is not true and bigger differences are visible in some groups of lines of sight.

The last observation is not surprising if we consider that uncertainties in the estimated profile of emissivity are translated in bigger errors in simulated brightnesses. These errors can be due to the temperature profile function which is based

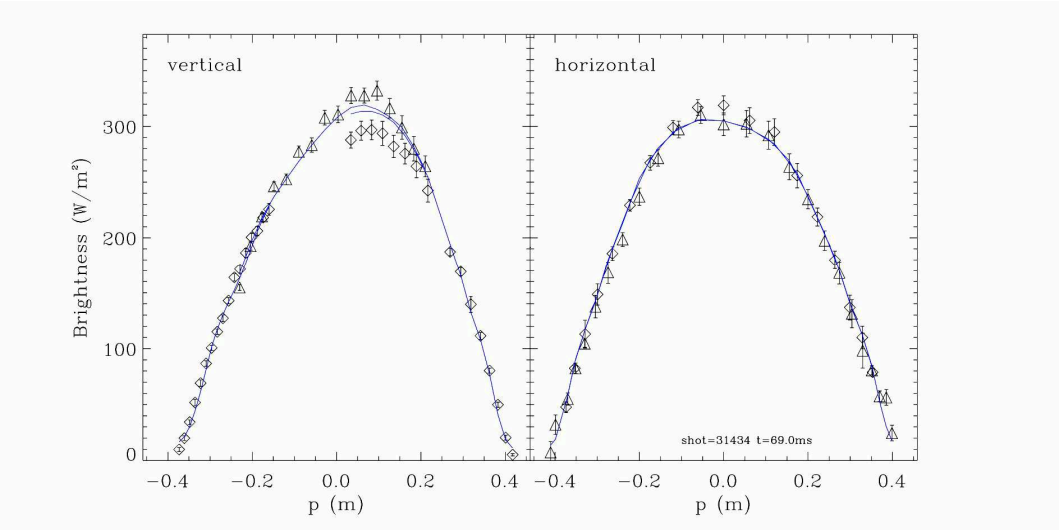

Figure 4.17: Brightnesses estimation with the Bremsstrahlung approximation. Plots report the experimental brightnesses in black while the simulation results are shown with the blue curve. Left panel reports vertical arrays, right panel reports the horizontal one. The simulation has been done using the value of K estimated with the central line of sight.

on remapped measurements: when small errors in the remapping process occur the computed emissivity profile will be, in some intervals of ρ, far from the real one. For these reasons, this technique must be improved in order to achieve reliable estimations of the enhancement factor profile.

CHAPTER 5

Mapped T_e profile dynamics during QSH regimes

This chapter is dedicated to the study of temperature gradient dynamics, estimated with the two methods shown in the previous chapter. The analysis is focused on QSH phases; in fact QSH are considered potentially improved regimes in confinement of energy (a detailed discussion is reported in chapter 1). The study hereafter described is peculiar, in the sense that a fast temperature diagnostic (DSX3, see paragraph 2.2) is extensively used for the first time.

The first step, presented in paragraph 5.1, is the comparison of the two procedures available for the gradient estimation, in order to select the most suitable for the analysis. Once an analysis method is defined, it is ready to be used on a wide database, whose construction is described in details in paragraph 5.2. Then, paragraph 5.3 describes the statistical analysis of the gradient dynamics reporting the correlations of its amplitude with plasma current, with magnetic modes and with other plasma parameters. Furthermore, also correlations of the gradient position ($r_{\nabla T_e}$) has been investigated. Finally, in paragraph 5.4, some conclusions are drawn.

5.1 ∇T_e choice

The methods for ∇T_e estimation defined in section 4.4 (*linear* and *tanh*) give comparable results although they use two different approaches: the *linear* method determines the slope involving a limited number of points on a single side of the helical structure, while the *tanh* method takes into account the full profile. Moreover, the *linear* method fits the data using the linear regression while the *tanh* method uses the hyperbolic tangent function: this may lead to interpret the profile as step shaped, even though it is almost flat.

As a result, *linear* method is less prone to remapping errors and its convergence is reliable, although steepest gradients may be underestimated (figure 4.12(b) shows

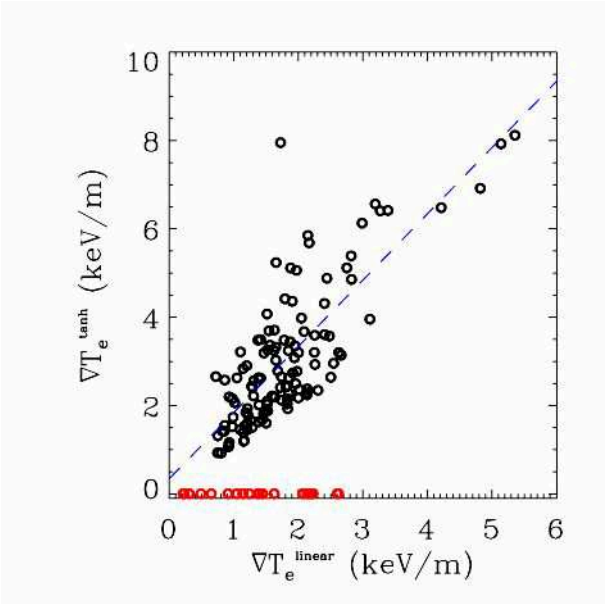

Figure 5.1: Comparison between *tanh* and *linear* methods for the gradient estimation on the shot 29961. The values of ∇T_eobtained with the *Linear* method are reported in abscissa while the corresponding estimations with the *tanh* method are reported in ordinate. Profiles where convergence of the *tanh* method has not been possible are shown in red. Dashed blue line summarizes the averaged relation between the two methods.

an example). Figure 5.1 summarizes the comparison of the two estimations for shot 29961: abscissa reports the gradients obtained with the *linear* method while ordinate reports those with the *tanh*. The two estimations are linearly correlated and the slope of the fitting line is higher than the equality, as expected. The plot reports in red also the cases where *tanh* method has failed to converge; for those ∇T_e^{tanh} has been imposed equal to 0. Most of the convergence failures happened at small ∇T_e, i.e. when the temperature profile does not show a clear step. Since next analysis is concentrated on QSH regimes, flat profiles should be rare, but we will see later in this chapter that this is not always true and the convergence problem related to these problems must be taken into account.

Paragraph 4.4.3 shows that the gradient estimation depends on the phase of the dominant mode and highlights that the correlation is stronger with *linear* method than in *tanh*. Anyway this effect has minor importance since the helical axis has a rotation frequency of about 25ms whereas QSH intervals usually last less than 10ms, thus the phase of the dominant mode does not change enough during a QSH interval. In this regard, figure 5.2 shows an example of the phase of the dominant mode as a function of time (panel (a)) and the evolution of the magnetic modes (panel (b), dominant mode in black). The comparison of the two panels shows that, during QSH intervals, the speed of the dominant phase slows down guaranteeing an

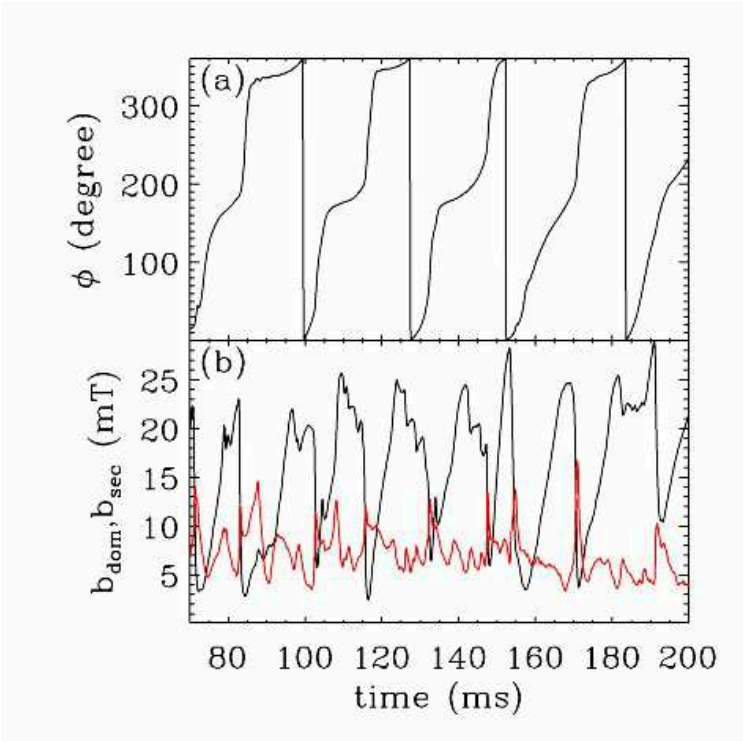

Figure 5.2: Example of phase dynamics for the dominant magnetic mode. Panel (a) shows the phase of the dominant mode as a function of time while panel (b) shows the corresponding amplitude, in black, and the amplitude of secondary modes, in red.

almost constant value of the magnetic axis position in the poloidal section. Figure 5.2 highlights also that QSH intervals do not happen at any phase of the dominant mode, on the contrary two favorite phases are clearly visible at about 180° and 0°. At the DSX3 toroidal position, such phases imply that the poloidal positions of the magnetic structure are 90° and 270°: incidentally, these are also the angles required in paragraph 4.4.3 for the best estimation of ∇T_e.

Since the scaling analysis have been mostly performed within single QSH intervals, the absolute value of the gradient is less important than its relative evolution. Hence the reliability turns out to be the most important feature to discriminate between the two methods and thus, although the higher precision on steep gradients achieved with *tanh* method, *linear* method will be preferred.

5.2 The database

This paragraph describes which are the main features of the pulses in the database. Several pulses belonging to high current campaigns have been analyzed selecting 157 discharges for a total of 555 QSH cycles. Each QSH cycle has been manually

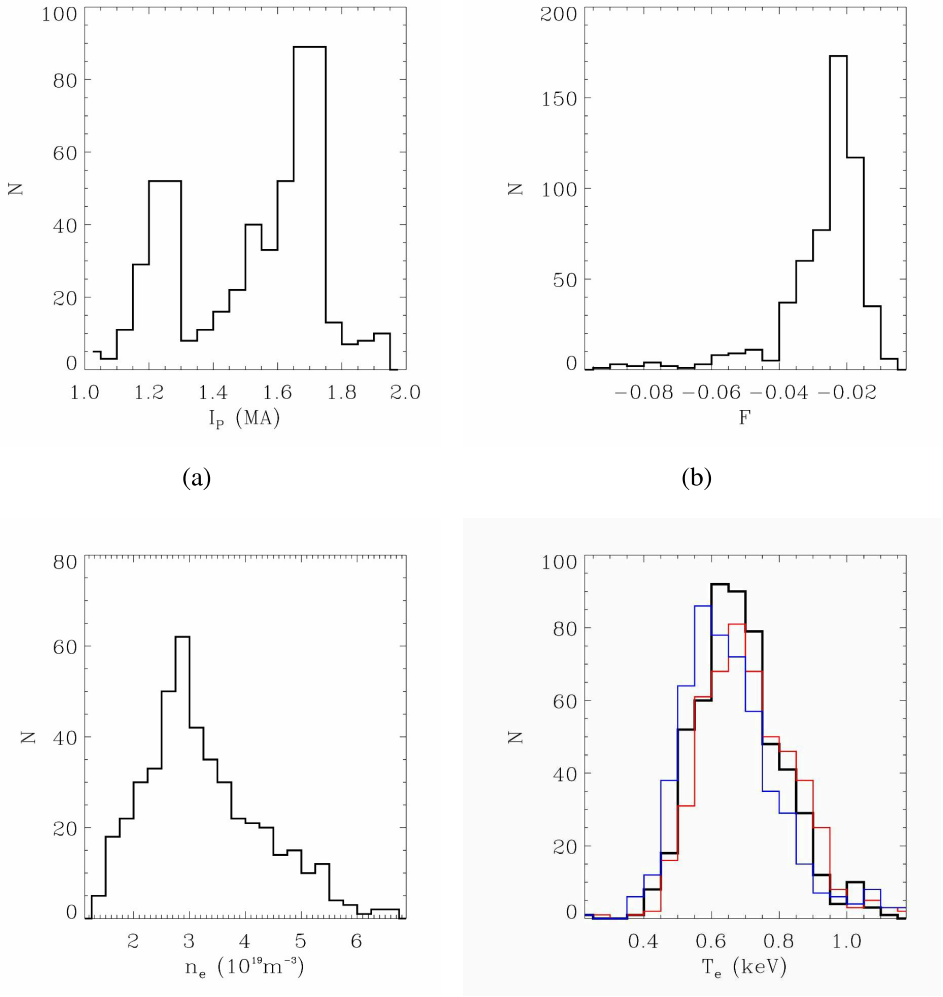

Figure 5.3: Features of the QSH intervals in the database. (a) The distribution of the plasma current. (b) The distribution of the reversal parameter F. (c) The distribution of the density. (d) the distribution of the central temperature is reported in black. The red and blue distributions are the central temperature averaged during *rising* and *flattop* intervals respectively. For each parameter a time average on the QSH interval is considered.

identified considering the evolution of the dominant mode, but it has been rejected whenever the SXR signals was noisy. The plasma current of the selected shots varies from 1 to almost 2 MA but the majority of cases is at 1.2 MA and at 1.7 MA. Figure 5.3(a) shows the distribution of the averaged current of each QSH interval in the database.

All of the QSH intervals are characterized by a similar equilibrium: the reversal parameter F, defined in formula 1.32 is in the range [-0.07, -0.02]; pulses with a lower value of F have been rejected. The distribution of this parameter is shown in figure 5.3(b).

All data have been sampled every 0.5 ms. This choice allows a good integration for the SXR signals, avoiding noise problems, and it ensures the required time resolution.

The duration of QSH intervals varies from 3ms to 50ms and, in analogy with paragraph 3.2, the long ones are split in two phases: the *rising* phase, in which the dominant (1,-7) mode rises and secondary modes decreases; the *flattop* phase, in which the dominant mode remains at high level (even if the amplitude fluctuates). Short QSH intervals do not have *flattop* phase. The distinction is justified since ∇T_e exhibits different behaviors during the two phases and, according to this, we have separated also the subsequent analysis.

The distribution of electron density (n_e) is reported in figure 5.3(c): most of the cases n_e is around $3 \cdot 10^{19}$ electrons per cubic meter, but some cases at high density (above $5 \cdot 10^{19} \mathrm{m}^{-3}$) have been included.

Finally, we report, in figure 5.3(d), the distribution of the central temperature averaged over every QSH interval (in black). These temperatures correspond to the average of the three lines of sight of DSX3 closest to the helical axis. The other two distributions, in red and blue, are the temperatures averaged on all *rising* and *flattop* intervals, respectively.

5.3 Results of statistical analysis

Here we present the results obtained from the statistical analysis of temperature gradients in QSH regimes. This paragraph is organized as follows:

- 5.3.1 reports and describes a paradigmatic QSH interval, in order to describe the features noted during this study; the distinction between *rising* and *flattop* phases are underlined.
- 5.3.2 analyzes the role played by the plasma current in the QSH features.
- In 5.3.3 the influence of the dominant magnetic mode on the barrier position is investigated.
- In 5.3.4 the gradient amplitude has been correlated to the secondary modes amplitudes.

- Finally, in 5.3.5 a threshold on the temperature gradient is defined, in order to distinguish the states with a thermal structure from those without it. Once the threshold has been established we measure the persistence of such states in the QSH intervals.

5.3.1. ∇T_e behavior during QSH intervals

This paragraph shows a typical example of QSH interval, in order to present the main features encountered during the analysis.

The example is shown in figure 5.4 where the transition between the two phases (*rising* and *flattop*) is highlighted by the vertical dashed line. Panel (a) represents the dominant (dash-dot) and the secondary (solid line) normalized toroidal mode amplitudes, measured at the plasma edge.

Panel (b) shows the time evolution of the estimated gradient. On the time scale shown in the figure the poloidal location of the helical structure does not vary significantly, therefore the gradient evolution is due to temperature profile modification and not to the instrumental error described in 4.4. It clearly appears that, even though the magnetic field topology remains helical during the QSH period, the thermal structure is not stationary. In the shown *flattop* phase there are 4 back-transitions to less peaked profiles; the corresponding gradients decrease to values of about 500 eV/m, which are typical of MH cases. On the other hand, transitions to low ∇T_e cases are less frequent during the rising phase, as paragraph 5.3.5 will show.

Panel (c) shows the central temperature (solid line), determined along the lines of sight nearest to the helical axis. The dashed line is the *edge* temperature, defined as the average of the T_e data points from the outer lines of sight. These chords correspond to a value of X up to $0.3 \div 0.35$m so this temperature should be considered as the outermost T_e for the diagnostic and not a true edge plasma T_e (the minor radius of RFX-Mod is 0.459m). Inspection of panel (c) shows that the gradient evolution is due to both a variation of the helical temperature and of the edge one. Moreover, transitions to flatter profiles are characterized by a decrease of the core temperature that may be accompanied by an increase of the edge temperature.

Finally, panel (d) shows the T_e gradient location $X_{\nabla Te}$ (black dots connected by a solid line, y-axis on the left, as indicated by the black arrow). It typically amounts to 20-30 cm from the helical magnetic axis and does not significantly oscillate in time. In the same panel the position of the O-point $X_{O-point}$ is shown (blue diamonds on a dotted line, y-axis on the right, as indicated by the blue arrow), defined as the distance of the magnetic O-point from the center of the vessel: it can be seen that during the QSH event the magnetic topology does not change significantly. In the following we will use $(X_{O-point} - X_{\nabla Te})$ as a way to estimate the radial location of the transport barrier or, equivalently, the size of the thermal structure.

The oscillations of ∇T_e that are shown in figure 5.4 typically occur in the whole

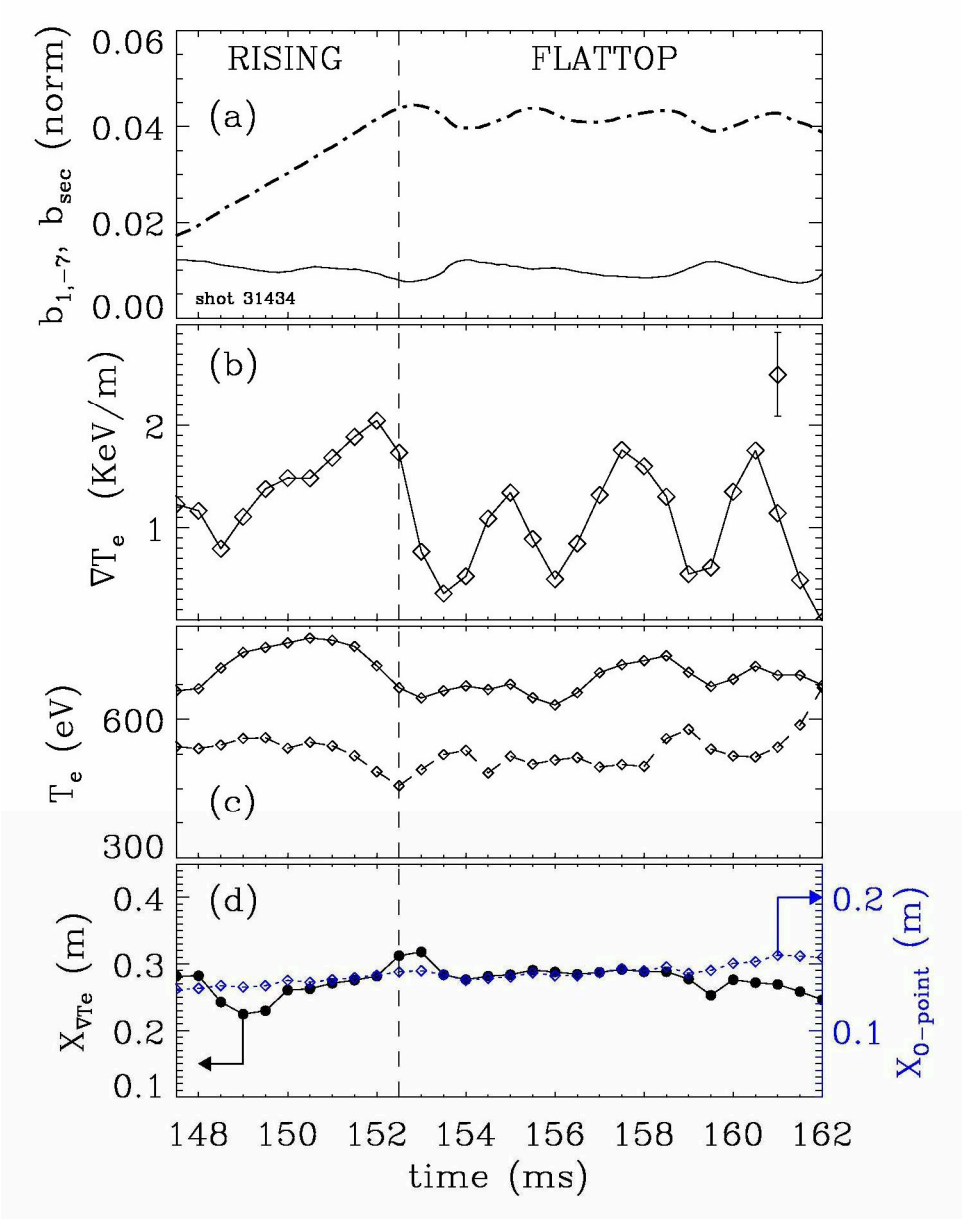

Figure 5.4: The ∇T_e evolution for shot 31434 between 147.5 and 162 ms: (a) The dash-dot line represents the dominant normalized toroidal mode amplitude and the solid line represents the secondary normalized toroidal mode amplitude. (b) The graphics shows the ∇T_e sequence estimation. (c) The central (solid line) and external (dashed line) temperatures. (d) The ∇T_e position $X_{\nabla Te}$ (solid line) and the O-point distance from the center of the chamber $X_{O-point}$ (dotted line, related to the right vertical axis). The vertical dashed line identifies the end of the *rising* and the beginning of the *flattop* phase.

database. A statistical characterization is performed by analyzing the distribution of the gradients for each phase of a QSH interval. Again the *rising* and *flattop* phases are considered separately, because the former is characterized by steeper gradients. As we wish to characterize the fluctuating behavior of the T_e gradient dynamics, we focus our attention on the extreme values by computing the $\nabla T_e^{10\%}$ corresponding to the 10^{th} and $\nabla T_e^{90\%}$ corresponding to the 90^{th} percentiles of the distribution: 10% of the gradients are below $\nabla T_e^{10\%}$ while 10% of them are above $\nabla T_e^{90\%}$. We have chosen this threshold so that, in short intervals (lasting for example 5 ms), 10% of the data corresponds to one sample at least.

5.3.2. The role of the plasma current

In this paragraph we analyze the possible correlations between the temperature gradient and the plasma current.

Figure 5.5 shows the I_p dependence of the *rising* (a) and *flattop* (b) phase duration. QSH phases below 3 ms in the *rising* phase have not been considered in order to avoid too short QSH events. It can be seen that the *rising* phase may last longer for discharges with current higher than 1.5 MA compared to 1.2 MA. The spread of *flattop* duration is significative, but longer *flattops* occurs more frequently at higher currents.

The database that we are considering includes QSH intervals that behaves qualitatively in a similar way with respect to the one published in [59]: longer lasting QSH intervals occur at the highest plasma currents.

The 10^{th} (blue dots) and 90^{th} (red dots) percentile of the ∇T_e distribution of the rising phase of each QSH intervals, as a function of I_p, is shown in 5.5(c). Within the spread of the data (that cannot be ascribed only to the (±20%) uncertainty in the gradient estimate illustrated in paragraph 4.4.3) we observe that the ∇T_e fluctuates in time at all plasma currents. It can be observed the trend of both the maximum and minimum gradients to increase with current, confirming the empirical criterion pursued recently in RFX-mod in which the increasing of plasma current implies higher confinement times [32, 59, 65]. Besides the confinement time, also the growth of the heating power injected in the plasma can result in higher temperatures and gradients, but this is not the case. In fact we have evaluated the ohmic power for all the QSH intervals in the database and no correlation has been found with the plasma current, resulting almost constant instead.

This behavior is less clear during the flattop phase, shown in 5.5(d). Minimum gradients are lower than the corresponding ones in the rising phase, and do not seem to significantly vary with plasma current. Maximum gradients do scale with current, i.e. higher gradients can be found at higher currents, but they are not as steep as the ones occurring during the rising phase. This would suggest a saturation of confinement when the amplitude of the dominant mode reaches its maximum.

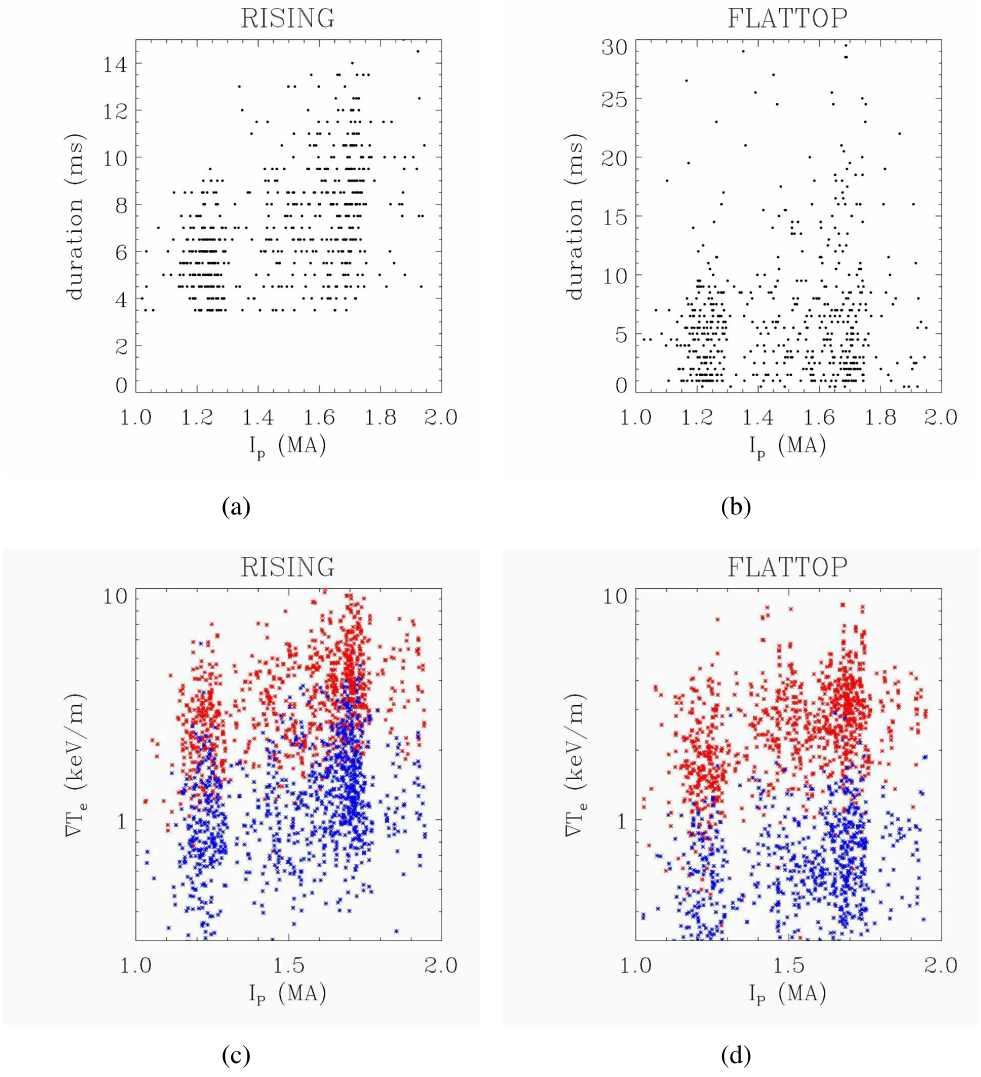

Figure 5.5: The *rising* (a) and the *flattop* (b) phase duration against the plasma current. Here I_p is defined as the plasma current averaged over the phase interval. The durations values are multiples of 0.5 ms because of the re-sampling. (c) The ∇T_evalues against the plasma current during the *rising* phases. The red dots correspond to the 90^{th} percentile in a given interval while the blue dots correspond to the 10^{th} percentile of the ∇T_edistribution. (d) The ∇T_evalues against the plasma current during the *flattop* phases.

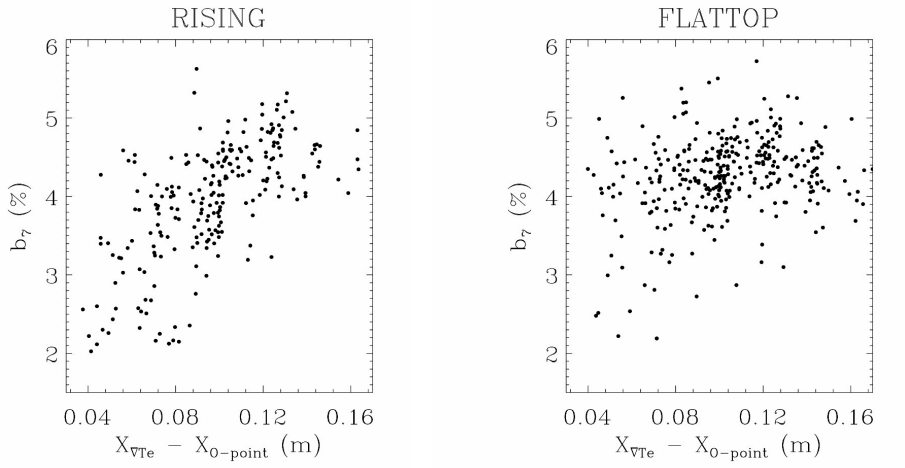

(a) (b)

Figure 5.6: Amplitude of the dominant magnetic mode, normalized to the edge magnetic field, plotted against the 90^{th} percentile of the size of the thermal structure. The *rising* phase is in (a), the *flattop* phase is in (b).

5.3.3. The role of the dominant mode

The intermittent behavior of the ∇T_e dynamics has been analyzed in terms of other magnetic quantities. As a first step, the effect of the amplitude of the dominant mode has been investigated. This mode determines the helical topology: it has in fact been shown numerically in [66] that the location of the transport barrier scales with the amplitude of the dominant mode, and it can be seen from equation 4.3 that the helical flux increases with the amplitude of ψ_7.

Figure 5.6 (a) and (b) show the amplitude of the dominant mode for the rising and flattop phases respectively, as a function of the location of the transport barrier (or the radial size of the thermal structure), as estimated by the difference between the maximum T_e gradient location ($X_{\nabla Te}$) and the O-point ($X_{O-point}$) location. To simplify the figures, only the steepest gradients during the intervals (i.e. the 90^{th} percentiles) are considered; moreover a selection on the parameter F, which can influence strongly the dimension of magnetic structures, has been performed ($-0.05 < F < -0.025$). Again, a significant correlation is found during the rising phase, which is characterized by a growth of the dominant mode. The same does not hold during the flattop phase, where a significant spread of the data points is observed even though the amplitude of the dominant mode is always large.

Previous studies, based on statistical analysis of profiles measured by the Thomson scattering diagnostic [66], have shown that the position of the helical transport barrier is strongly correlated with the location of the null point in the q shear profile. In the same paper, a numerical study shows that the amplitude of the dominant mode determines the helical equilibrium and therefore the location of the zero in

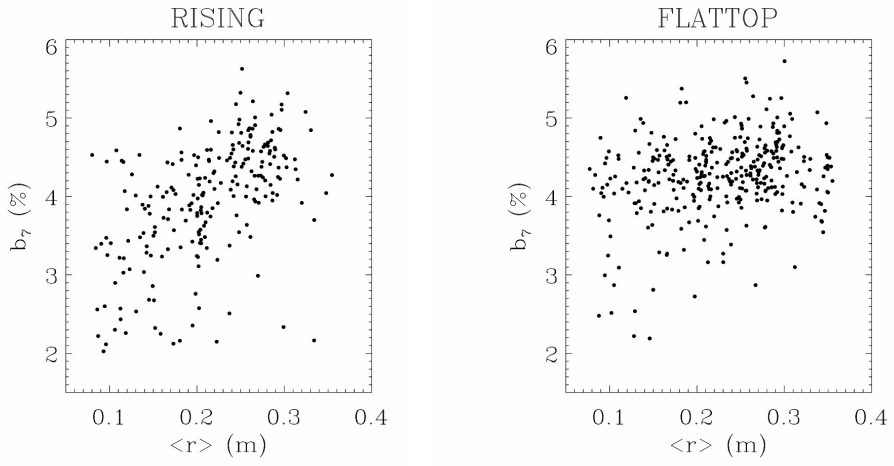

(a) (b)

Figure 5.7: Amplitude of the dominant magnetic mode, normalized to the edge magnetic field, plotted against the 90^{th} percentile of the size of the thermal structure. The *rising* phase is in (a), the *flattop* phase is in (b).

the shear of the q profile. Thanks to the higher time resolution of the DSX3 diagnostic, the results shown here give a more detailed picture. During the rising phase, the maximum Te gradient is located near the vanishing shear radius region, consistently with previous findings. Therefore, during the rising phase an expansion of the thermal barrier, related to the increase mode amplitude, often occurs. On the other hand, during the flattop period the barrier is more likely located in an inner region, away from the vanishing q location, indicating that other transport mechanisms (occurring on slower time scales compared to the rising duration) determine the transport during that phase.

Anyway, the growth of the difference $X_{\nabla Te} - X_{O-point}$ does not implies strictly an increase of the structure dimension. For instance, it is compatible also with a shape variation of the transport barrier. In particular, this last hypothesis is consistent with the DAx→SHAx transition, which involves a variation from a concave shape (necessary to incorporate the second axis and the separatrix) to another more convex one (see figure 4.2 for a visual comparison). A resolutive study can be done using $\langle r \rangle$, defined in paragraph 4.4.1, instead of the distance of ∇T_e from the O-point. $\langle r \rangle$ computation is based on the area of the helical structure on the poloidal section and hence it is directly linked to its volume. Plots in figure 5.7 report the dominant mode amplitude as function of the $\langle r \rangle$, in analogy to those in figure 5.6 excluding the abscissa. The results are confirmed and a correlation is still visible during the *rising* phases whereas it is absent during *flattop* ones.

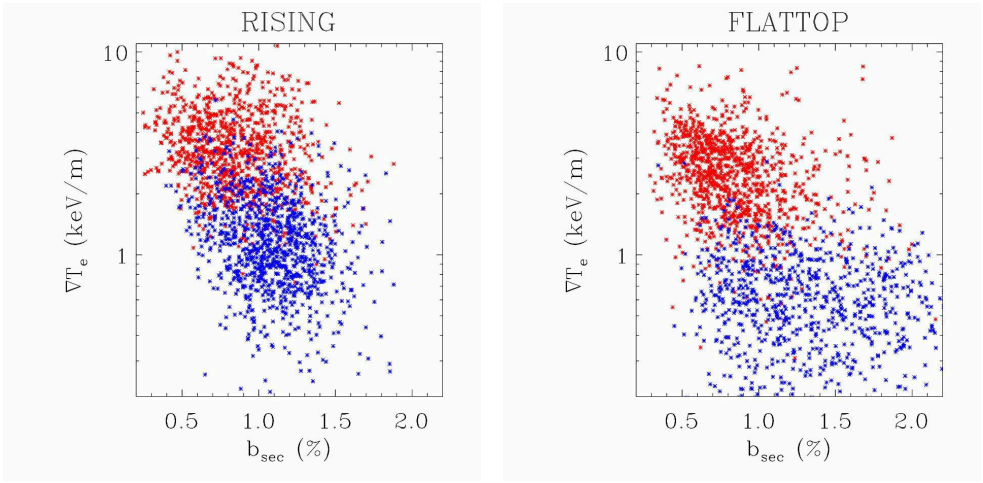

(a) (b)

Figure 5.8: The ∇T_e values against the secondary modes normalized to the edge magnetic field. The gradient above the 90^{th} are shown in red and those below the 10^{th} percentile in blue. (a) *rising* phases; (b) *flattop* phases.

5.3.4. The role of the secondary modes

Secondary modes have often been considered as a fundamental parameter governing RFP transport, in the wake of the work by Rechester and Rosenbluth (RR) on tearing-mode dominated, chaotic transport [24]: and indeed a scaling of energy confinement time as $\tau_E \approx (b_{sec}/B_{\theta,a})^{-1.1}$ has been found in the RFX-mod [33, 42]. But, from a theoretical point of view, the applicability of a RR-like type of transport is obviously questionable in a QSH state, where much of the flux surfaces in the core are conserved, as shown above. This prediction was confirmed in the past analysis reported in [67]. Here we will consider the role of these modes on the gradients, on the same database used for the dominant mode. While the location and size of the maximum ∇T_e is found to depend on the dominant mode (at least as an upper limit, for the cases where a significant gradient exists), its amplitude is found to only weakly depend on the secondary modes. Figure 5.8 (a) and (b) show the dependence of the T_e gradient on the normalized amplitude of secondary modes. Even if a certain spread affects the data, an inverse dependence of the gradient on secondary modes can be highlighted during the rising phase. In particular the lowest gradients (i.e. the 10^{th} percentile, blue dots) on average occur when secondary modes are higher.

Concerning the flattop phase, a more complex picture emerges. The highest gradients almost always occur at low values of secondary modes, but the opposite does not hold so clearly as for the rising phase. Low values of the gradients are found for a relatively wide range of secondary modes amplitude, further suggesting that an additional transport mechanism is at work in this phase. Overall, the behavior of

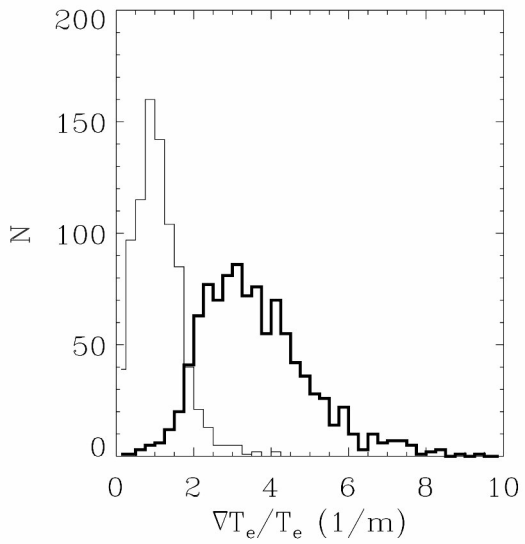

Figure 5.9: The $\nabla T_e/T_e$ distribution for the *flattop* phases: the thick line indicates the gradients higher than 90^{th} percentile and the thin line those below the 10^{th} percentile. 2m^{-1} is the separation value.

the secondary modes is closely related to the dominant mode, as secondary modes decrease when the dominant mode increases during QSH (see Fig.5 (a) in ref. [59]).

5.3.5. Duration of a internal transport barrier

The time evolution of the electron temperature gradient during the rising phase is basically determined by the combined evolution of the dominant mode, that determines the size and location of the thermal helix, and by the secondary modes that determines the amplitude of ∇T_e. On the other hand the evolution during the *flattop* phase is less clear. To add new information in the analysis of this phase, the duration of the periods of *high gradient* has been characterized. These *high gradient periods* are defined as the times within a QSH phase (*flattop* or *rising*) where the ∇T_e is above a certain threshold; the durations of these *high gradient periods* has to be compared with the overall durations of the entire phases.

The choice of the threshold is not obvious as we want to compare intervals at different plasma current and consequently at different temperatures. Various approaches have been pursued. Firstly, the typical ∇T_e in a MH states is evaluated: it results to depend on many factors, as stated in [33], but it is always lower than 1 keV/m. Such a value can not be considered a good choice for the threshold since the database includes a wide range of currents and hence of temperatures. The most simple way to take into account these measurements is to normalize it to the core temperature of the plasma (described in paragraph 5.3.1). With such a method the

resulting value is about 2m^{-1}.

Another approach is to evaluate the distribution of the normalized T_e gradients during *flattop* intervals. *Flattop* phase has been preferred to *rising* one because in the latter ∇T_e is strictly dependent on the magnetic condition (dependence on the dominant and secondary modes), as expected in a QSH state, whereas the former does not present these evidences, gradients are lower and more oscillating and consequently back transitions to MH-like configurations are possible. Also in this case ∇T_e is normalized to T_e^{core}. In figure 5.9 the distributions of the 10^{th} and 90^{th} percentile (thin and thick line, respectively) of the normalized gradients are shown. The two distributions are only slightly overlapped, and a separation threshold can be defined at $\nabla T_e/T_e$=2m^{-1} (or equivalently L_{Te}=0.5m) in order to distinguish between the *high gradient periods* and the flat T_e profile periods.

It is worth to note that, if higher ∇T_e in almost every *flattop* interval can not be certainly ascribed to a MH-like configuration, lower ones can: their normalized ∇T_e are below the first threshold found and thus their energy transport is compatible with the one in a chaotic state. A similar behavior is seen in the tokamak ITB ("critical gradient" mechanism) [68, 69].

To compare the overall phenomenology of the gradients with the dynamics of the dominant mode, the *rising* and *flattop* phases of all QSH intervals have been analyzed and the periods when the $\nabla T_e/T_e$ is above the threshold have been recorded. The Maximal Thermal Duration (MTD) is the length of the longest period above the threshold. Figure 5.10(a) shows the MTD vs the corresponding *rising* phase duration. The size of each dot is proportional to the number of 0.5 ms instances. The majority of cases stay along the bisector confirming statistically that thermal structures very often occur simultaneously with the magnetic helix, even though thermal back-transition may occur (dots below the bisector). The same correlation does not hold during the *flattop* phase as shown in figure 5.10(b). This means that the back-transition of the gradients, which is seen when the dominant mode saturates (figure 5.4 (b)), is driven by some mechanism other than the interplay between dominant (figure 5.6(b)) and secondary (figure 5.8(b)) modes, and does not even seem to be correlated with the ohmic input power (figure 5.5(d)).

To complete the analysis also the Total Thermal Duration (TTD) has been considered, defined as the overall time in which the threshold is exceeded (even in non consecutive time frames). The results are basically the same as shown in figure 5.10 (c) and (d).

5.4 Conclusions

In this chapter in order to perform a statistical analysis a single method of gradient estimation of the two proposed in 4.4.2 has been chosen. Then, the gradient has been computed in 157 selected shots every 0.5 ms, in order to reconstruct the thermal dynamics during the QSH intervals. A different behavior has been recognized

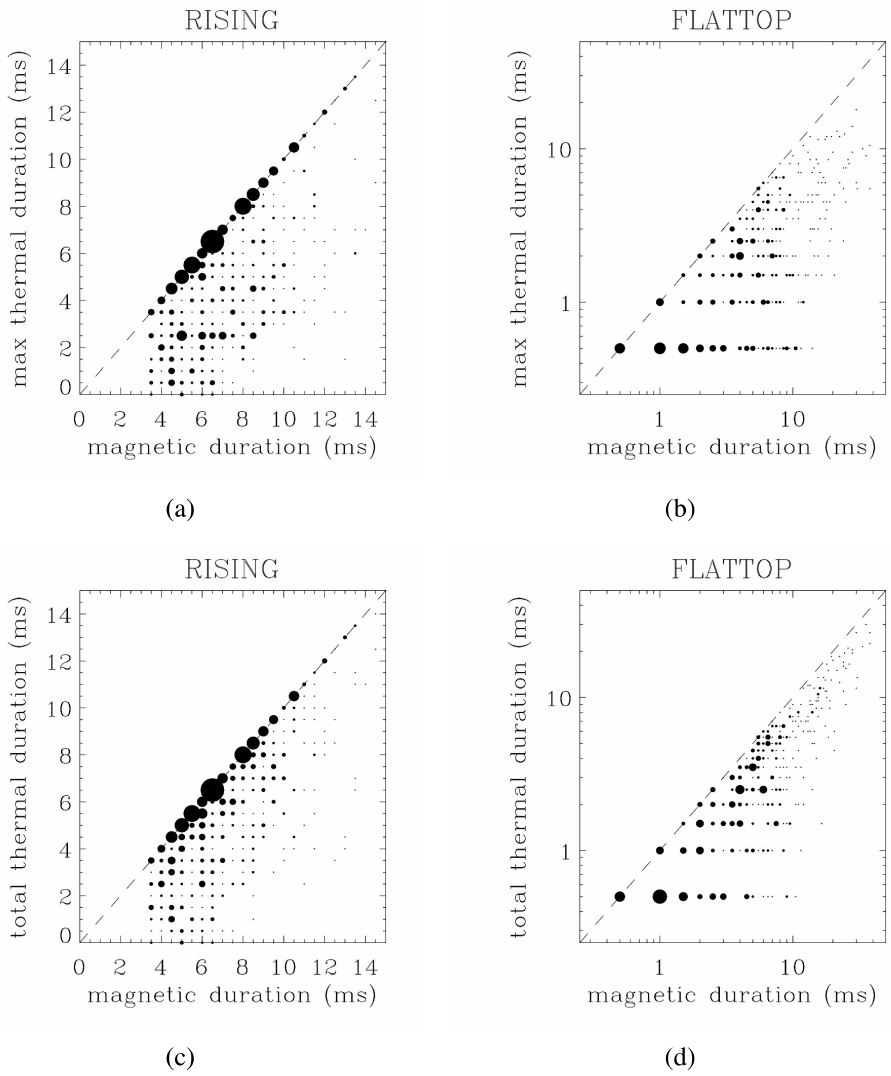

Figure 5.10: (a) Distribution of Maximum Thermal Duration (MTD), plotted against the corresponding *rising* phase length (Magnetic Duration). (b) MTD for the *flattop* length. (c) and (d) Total Thermal Duration (TTD) against the corresponding *rising* and *flattop* phase duration. The size of the dots is proportional to the number of 0.5ms instances.

comparing the *flattop* and the *rising* phases. Moreover, a slight correlation between gradients and plasma current has been noted during the *rising* phase. The same correlation is not visible for the weakest gradients (i.e. below the 10% percentile) during the *flattop*. The size of the thermal structure has been investigated and it has been found that it typically expands during the rising phase correlated with the dominant mode amplitude, as numerically predicted in [66].

During the *flattop* phase a more complex mechanism governs the structure dimension, so that its value spreads out in spite of the constant value of the dominant mode. The gradient is also influenced by the secondary modes, both during the *rising* and the *flattop* phases. Nevertheless the weakest gradients in the *flattop* phases seem unaffected by the secondary modes; their behavior and their values are similar to that occurring during MH configurations. From these considerations a threshold on $\nabla T_e/T_e$ has been defined in order to define the intervals where there is the thermal evidence of the helical structure. The helical structure is evident during most of the time in the *rising* phases. Vice versa, in the *flattop* phases the time duration of the thermal evidence does not last as long as the magnetic interval and, in general, it is unable to last more than 10ms.

Summarizing, temperature profiles follow closely the helical flux surfaces set by the dominant mode, but the gradients (evaluated along the flux surfaces) follow the dynamics of the helical mode only when it is growing. The role of the secondary modes, which has been underlined in the past [33, 42], is similar to that of the dominant mode. When the dominant mode grows and saturates, some other mechanism acts in the fashion of the "critical gradient" mechanism of Tokamaks [68, 69], with a characteristic length of the gradient L_{Te} = 0.5m. Possible candidates are micro-turbulence [70] or helical plasma-wall interaction and flows at the edge plasma [71].

CHAPTER 6

SXR emissivity and T_e profile estimation in helical flux coordinates in MST

Since SXR tomographies are widely adopted to investigate plasma dynamics, the methods developed above in this thesis, can be applied on many other RFP experiments. During my PhD period, I have had the opportunity to apply the algorithm for the reconstruction of the emissivity profile (see paragraph 4.2) to the Madison Symmetric Torus (MST) experiment (Madison, WI, USA).

This chapter describes how the algorithm has been converted; in fact, as described in the following, the two SXR tomography diagnostic of MST and RFX-mod have different features. Moreover, the aim of the converted algorithm has changed in the estimation of the temperature profile instead of the emissivity one; this choice is due not only to the differences between the to experiments diagnostics, but also because MST experiment did not have two foil diagnostics for fast temperature analysis; .

In addition, an alternative method to estimate the profile of T_e has been developed. This new method is called *two foil simulation* since it exploits the features of MST tomography (which divides the lines of sight on two filter thicknesses) to simulate the missing brightnesses for a two foil diagnostic.

This chapter is organized as follows:

- In paragraph 6.1 the features of the MST experiment are described. Moreover, its SXR diagnostics are discussed.
- Paragraph 6.2 explains how the algorithm, developed in chapter 4, has been adapted to the new diagnostic device, with some results.
- Finally, paragraph 6.3 describes the method, named *two foil simulation*, de-

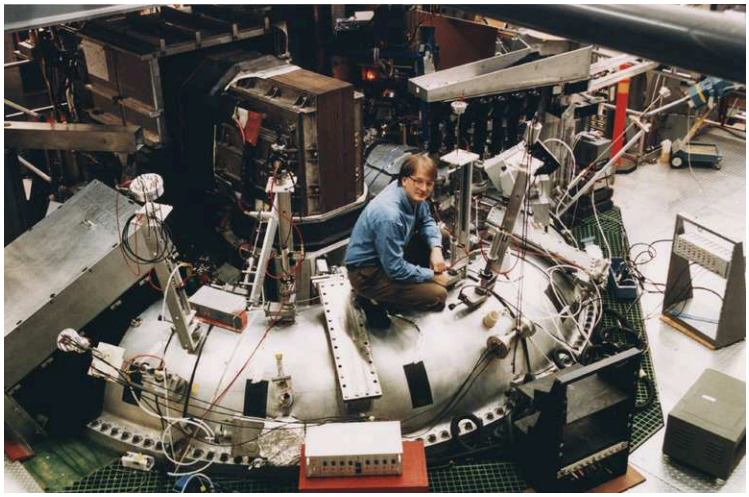

Figure 6.1: The MST experiment in Madison, Wisconsin.

veloped to determine the temperature profile. An analysis on its reliability is also reported. Such a study characterizes the limits of this new method applying it to both the experimental and numerical case.

6.1 The Madison Symmetric Torus experiment

MST is a large RFP experiments with 1.5m major radius and 0.52m minor radius; it can drive plasma currents up to 600 kA. The working electron density ($0.5 < n_e < 2 \cdot 10^{19}\mathrm{m}^{-3}$) is lower than that of the RFX-mod machine ($1 < n_e < 6 \cdot 10^{19}\mathrm{m}^{-3}$); the I/N range for the two machines is however similar around $2 \div 5 \cdot 10^{-14}$ Am.

There are some important differences in the way the two experiments are built: in particular, MST has not separate components for the vacuum vessel, the flux conserver, the first wall and the toroidal field winding: all these function are made by a thick aluminum vessel, interrupted by a toroidal and a poloidal insulated gap. The toroidal magnetic field is obtained discharging a capacitor bank directly on the vessel, so that a current can flow in the poloidal direction around the chamber.

The first wall is essentially metallic, since the plasma faces the vessel inner surface except for a thin row of graphite tiles which runs along the toroidal gap and acts as limiter; this influence the density behavior: compared to RFX-mod, the recycling from the wall is lower and this is one of the reasons why the density profile appears more peaked in MST; moreover, the density control is easier, since graphite wall, in RFX-mod, requires a wall which absorb H atoms and acts as an H reservoir conditioning for operations at low densities.

Another difference is in the poloidal winding for the inductive current drive: while RFX-mod uses an air core transformer, in MST there is an iron core couple to the winding with the plasma torus.

In MST there are no coils for the control of the magnetic instabilities except

at the poloidal gap neither vertical field windings for the horizontal equilibrium of the plasma: the horizontal stability is limited by the resistive diffusion time of the magnetic field across the aluminum shell. This is one of the reasons why the discharge duration is lower ($\approx$ 50ms) than in RFX-mod (up to 400ms). MST usually works with deuterium filling; this feature is important in QSH analysis since the way in which the instabilities rotate is experimentally found to depend on the gas type.

MST operates mainly in standard mode or PPCD [72]. PPCD (acronyms for Pulsed Poloidal Current Drive) [73, 74] is a transient regime developed with the aim of suppressing the magnetic chaos by driving directly the poloidal current. This is transiency done varying the toroidal flux, in principle, eliminating the requirement of the dynamo to sustain the poloidal current. It is performed applying a current waveform on the toroidal magnetic system (i.e the vessel itself in MST). PPCD phases last for $\approx$ 10ms and are characterized by the decrease of all $m = 1$ modes. An internal barrier is associated either to cases with all the modes suppressed, or with one or two modes remaining higher than the others. The latter evidence is coherent with the picture of PPCD as axysimmetrical states, whose topology is independent on magnetic spectra: ITBs are thought to develop only as a result of dynamo suppression. However, the point is still controversial: in particular, analysis performed in the past with PPCD discharges were able to identify rotating, bright SXR islands in the plasma core [12, 75, 76] and magnetic reconstruction of the plasma topology have shown that DAx configurations are often reached. This suggested the possibility to relate the ITB to a QSH-like state and to identify the internal barrier with the presence of a single island in the plasma core. Concerning the operations in standard modes, the most interesting regimes are achieved with $F = 0$ (non-reversed discharges); in these cases QSH regimes have been observed in magnetic spectra.

6.1.1. Diagnostic devices

This paragraph presents firstly the features of the magnetic diagnostic and finally the features of SXR tomography. At the time of this work no two foil diagnostic, for high frequency measurements of the temperature, were implemented.

In MST magnetic perturbations are measured with the toroidal array of 64 coil sets evenly distributed in toroidal angle. Each set consists of $\tilde{b}_\theta$, $\tilde{b}_\phi$ and $\tilde{b}_r$ coils wound on a single die. Anyway, every other poloidal field coil are usually employed, for a total of 32 $\tilde{b}_\theta$ signals, providing a resolution of the dominant toroidal modes up to $n = 15$ [77]. Magnetic data are then processed with a standard Fourier decomposition to extract the fluctuating components of individual toroidal modes.

In RFX-mod magnetic data are used to determine the magnetic topology of the plasma, as described in paragraph 4.1; also here, adapting the same procedure, it is possible to reconstruct the helical magnetic surfaces associated with the dominant mode. Unfortunately, the straight application of the algorithm is not possible be-

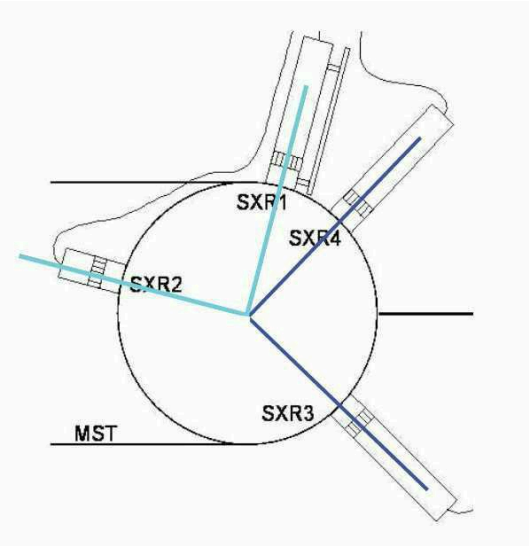

Figure 6.2: Layout of the head positions in MST tomography.

cause MST discharges have usually $F = 0$ and thus the standard $\alpha - \theta_0$ parametrization for the current density [27] is not able to reproduce both the axisymmetric edge magnetic data and the resonance condition of the dominant mode. This problem implies a non-automatic procedure for the determination of the magnetic topology. The paper of Auriemma et al. [78] discuss exhaustively the problem.

The SXR tomography in MST consists of 4 measuring heads, 20 lines of sight each, mounted in the same toroidal position [79]. Each head contains a silicon diode array which houses the 20 detectors on a single chip, disposed in a row; the bandwidth of the system reaches 100 kHz.

Each diode array is shielded from the plasma by a steel piece with rectangular pinhole (aligned with the photodiode itself) which defines the line of sight. A Beryllium foil covers the pinhole and act as a high pass filter for the X-ray radiation, the cutoff wavelength depending on its thickness. The distance between the pinhole and the detector, which is of few millimeters, can be set to two different values in order to vary the divergence of the lines of sight fan; this is useful if one wants to achieve a better resolution in the core (losing informations on the edge).

As reported above, the first wall is made of aluminum, which implies the presence of such element between the plasma impurities; for this reason SXR diagnostics require thicker *Be* filters in comparison to those used in RFX-mod. During the years various pairs of filters were adopted but the most frequent are 303-761μm and 408-821μm (in comparison to 42 and 88μm used in RFX-mod).

The diagnostic is usually set to work as a double color temperature tomography: the four heads are divided in two couples, the two heads belonging to each couple lie at a 90° poloidal distance. Each couple can reconstruct independently the SXR radiation pattern; if the two pairs are equipped with filters of different thickness,

they can be used to measure the plasma temperature from the ratio of emissivities, as a normal double filter T_e diagnostic, but returning a 2D map. A sketch of the arrangement of the four probes is reported in figure 6.2.

Unfortunately double color tomography involves significant temperature errors linked to mathematical coupling between the two tomographic inversions: tiny oscillations in the emissivity reconstructions are sufficient to destabilize their ratio and thus the related temperature. Figure 6.3 shows an example of temperature profile obtained with this method [79].

6.2 Algorithm to reconstruct the temperature profile in helical coordinates

In this paragraph the algorithm, originally developed in RFX-mod and then adapted to the MST experiment, will be described. This new algorithm has the purpose to estimate the temperature profile from the tomography, keeping into account its complex design.

According to chapter 4, the reconstruction of the magnetic topology allows a different approach to the SXR tomography. Briefly, the method developed above consists of: considering the emissivity of the plasma as a function of the helical flux coordinate ρ; then, from the known magnetic topology, obtaining the brightness of each line of sight with a numerical integration; finally, after a comparison between numerical and experimental data, getting the emissivity profile that fits the SXR data.

This method can be also applied to the MST experiment, but the different features of the tomography impose a different approach. As mentioned in paragraph 6.1.1, the tomography uses two filter thicknesses and thus the process to estimate the emissivity should converge twice providing two distinct profiles. Moreover there are not two foil diagnostics for fast temperature estimation. These problems can be overcome performing a convergence on the temperature profile instead of the emissivity one; this is possible using formula 4.10 in which the emissivity is obtained from the electron temperature. Consequently, with one temperature profile the brightness of each line of sight of the tomography can be simulated, independently of the array it belongs to.

The algorithm follows the same strategy developed in paragraph 4.2, but here the temperature profile is modified instead of the emissivity one. The exact procedure used in the algorithm is the following:

1. Maps of ρ, SXR data and the initial guess of the temperature profile are collected.

2. The brightness of each line of sight is computed and compared to the raw data.

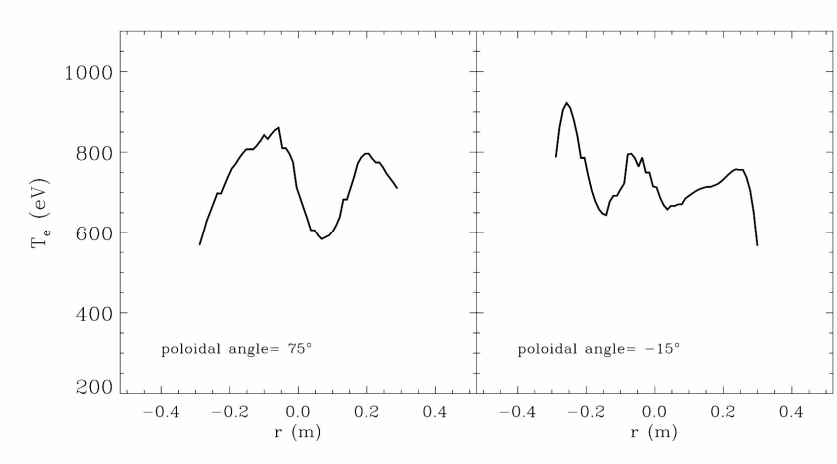

(a)

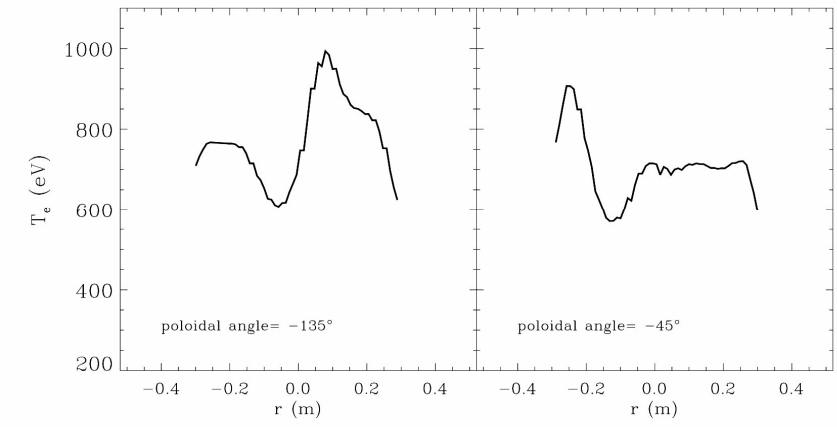

(b)

Figure 6.3: Temperature estimation provided by the double color tomography (shot 1070829100 at 26ms). The four profiles shown above are obtained cutting the temperature contour at four different poloidal angles. Such angles are selected in a way that cuts are facing the four probes of the tomography. In particular the two profiles in (a) are facing probes 1 and 2 while the profiles in (b) are facing probes 3 and 4. Such a method of the temperature estimation involves significant and unphysical temperature oscillation, as visible in this example.

3. The algorithm changes the temperature profile in order to minimize the χ^2 computed from the raw data and the calculated one; the SXR data errors are taken into account. A loop of the two actions 2 and 3 starts.

4. When the minimum of the χ^2 is reached the algorithm interrupts the iteration and quit.

In this algorithm, temperature profile is modeled as a polygonal line in which the free parameters are the slopes of the constituting segments. At the beginning all the slopes are assumed constant and proportional to the central temperature; then, they are modified by the algorithm in order to converge the simulated brightness to the experimental data. The construction of T_e profile starts from the edge where the temperature is imposed equal to zero; in this way, the profile will grow monotonically from the edge to the center, as slopes are imposed to be negative. The profile is composed by nine segments (the chosen vertex are in $\rho \equiv \{0, 0.1, 0.2, 0.3, 0.4, 0.5, 0.7, 0.9, 0.95, 1\}$).

Supposing that the emissivity of the plasma is exclusively due to the bremsstrahlung effect, the enhancement factor K in formula 4.10, must be equal to 1. In real plasma, the fraction of the emissivity not due to bremsstrahlung effect (which gives eventually the factor K) can be evaluated from the ratio f_{ex}/f_{br}, in which f_{br} is the brightness computed taking in account only the bremsstrahlung effect and f_{ex} is the experimental one. The standard temperature profile, required to compute of f_{br}, is defined in formula 6.1 in which: $\alpha = 3.5$, $\beta = 2.5$ and the value of T_e^0 can be obtained either from the TS or from *the two foil simulation* (see description in paragraph 6.3).

$$T_e(\rho) = T_e^0 \cdot (1 - \rho^\alpha)^\beta \tag{6.1}$$

The algorithm implements the two enhancement factors calculations (one per filter thickness). The lines of sight chosen to determine K are those passing through the magnetic axis of the plasma.

The number of the lines of sight for each filter thickness is sufficient to perform two different convergences in order to obtain two different temperature profiles, instead of a single one. In this case the procedure described above is still adopted but it is executed two times, one per filter. The two resulting temperature profiles are then compared.

6.2.1. Convergence results

Here some results obtained from the application of the convergence method developed in previous paragraph are shown.

In the following analysis we have proceeded with separated processing on the two filters comparing the resulting temperature profiles at the end.

The first example reported here is referred to shot 1070829100 at 26ms. This shot is characterized by filters thicknesses of 303μm, in arrays 1 and 2, and 761μm,

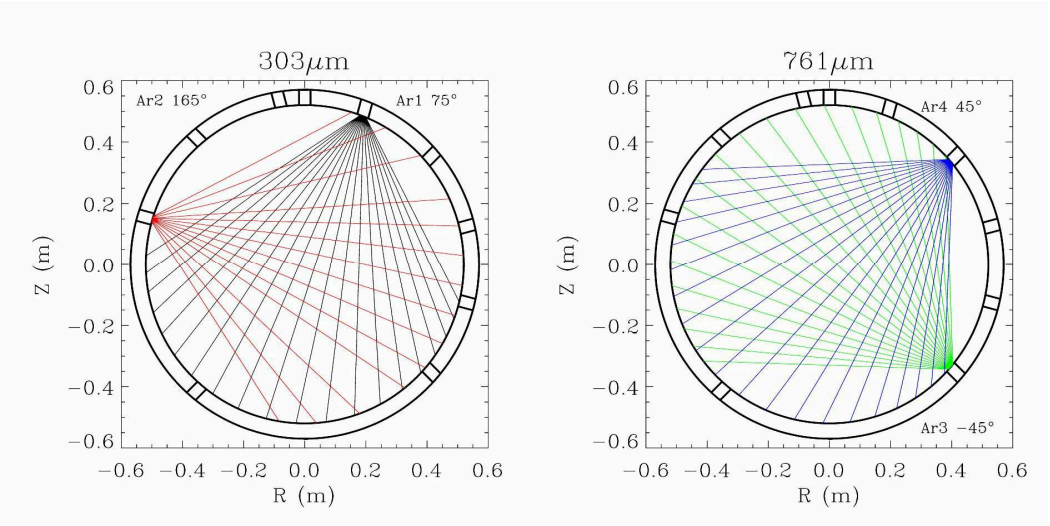

Figure 6.4: Lines of sight scheme for the shot 1070829100. Left panel: lines of sight for the probes 1 (black chords) and 2 (red chords). Right panel: lines of sight for the probes 3 (green chords) and 4 (blue chords).

in arrays 3 and 4. All the four fans of tomography were active and the sketch of lines of sight is reported in figure 6.4. Although the discharge make use of the PPCD modality, at the selected instant PPCD is already finished and the QSH is weak (note that the dominant mode in this case has periodicity (1,-6)). The density at that instant is $9.6 \cdot 10^{18} \mathrm{m}^{-3}$ and the plasma current has the value of 490kA.

The enhancement factors found here are $K_1 = 78.3$ and $K_2 = 80.0$ for thin and thick filter respectively.

In figure 6.5 the blue solid lines represent the simulated signals and the black void circles are the experimental data. Panel (a) shows the brightnesses of arrays 1 and 2 while panel (b) the arrays 3 and 4. The two temperature profiles obtained are reported in figure 6.6(b), red identifies the thin filter and blue the thick one. Finally, the plasma topology determined for this case is shown in 6.6(a).

The two enhancement factors are very high, this is coherent with the fact that MST plasmas have usually a big amount of impurities (overall Aluminum), if compared to those in RFX-mod. Besides, the brightnesses obtained with the computation are close to the data, this indicates both that the topology reconstruction is good and that the T_e profiles have finely converged. Finally, temperatures obtained from the two filters are close to each other as expected.

Another test has been performed on shot 1090415018 at 19.5ms. This discharge is characterized by plasma current of 496kA and the electron density resulted of $n_e = 1.42 \cdot 10^{19} \mathrm{m}^{-3}$; also in this shot the PPCD modality has been adopted.

In this case the chord fans have been narrowed increasing the distance between pinholes and diodes, as visible in figure 6.7 in which their configuration is shown. The estimations of the enhancement factors are: $K_1 = 81.2$ for the thin filter and

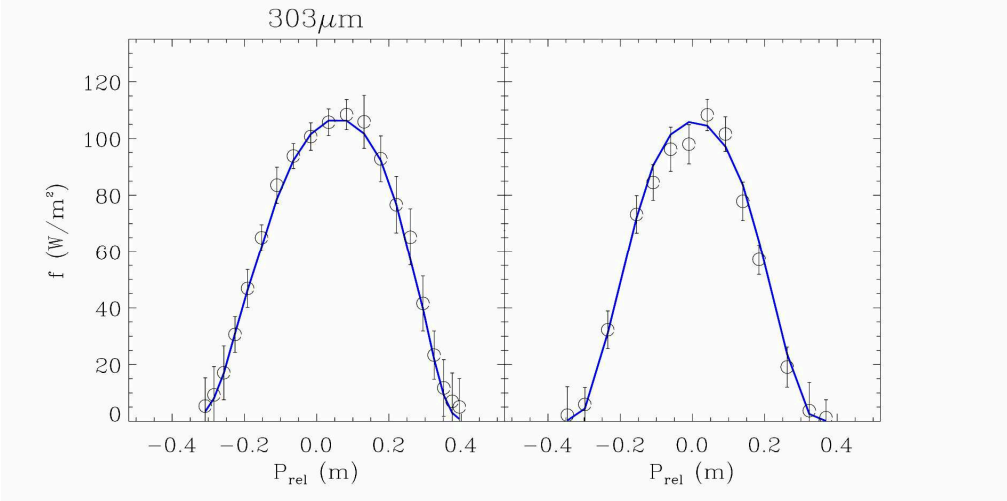

(a) tomography arrays 1 and 2

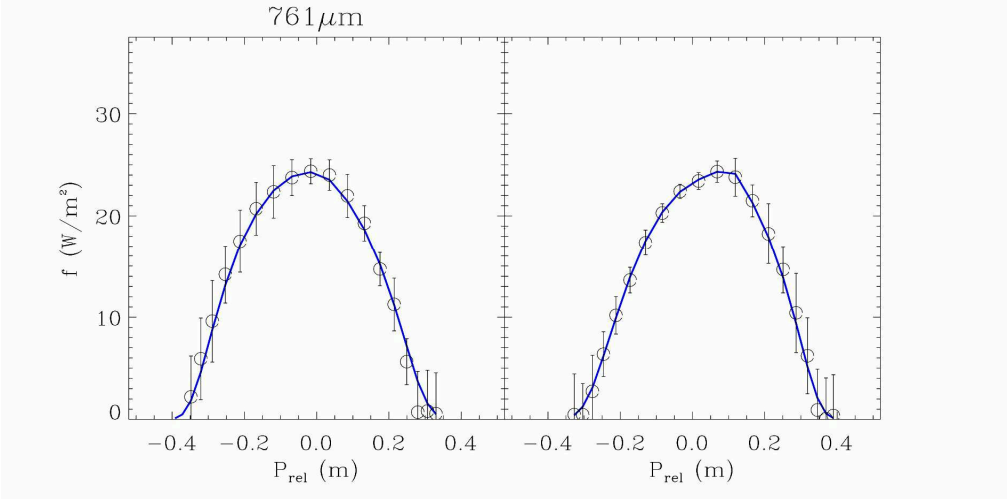

(b) tomography arrays 3 and 4

Figure 6.5: Algorithm for the temperature profile estimation applied to shot 1070829100 at 26ms. Plots show the brightnesses obtained from the convergence on the temperature profile (blue line) compared to the experimental ones (black circles).

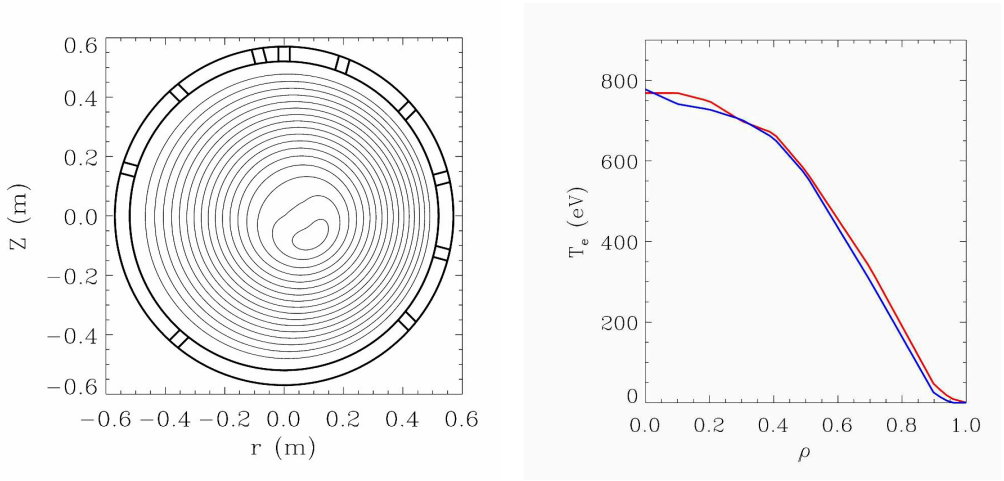

(a) (b)

Figure 6.6: Algorithm for the estimation of the temperature profile, shot 1070829100 at 26ms. Panel (a) is a contour of the map of ρ. The two profile $T_e(\rho)$ obtained from the convergences on the two filters are shown in panel (b). Red curve identifies the 303μm filter while the blue one the 761μm filter.

$K_2 = 80.3$ for the thick one, resulting very close to those estimated in the previous case although the used filters are thicker: 408μm thin filter and 821μm thick filter.

Plasma topology was not available at the selected instant and the reconstruction has been performed with the map developed in the previous case. Although the phases of the dominant magnetic mode of the two cases are close (about 300°), this map describes another plasma condition and the convergence can not reach the same accuracy level.

The results are reported in figure 6.8, also in this case blue lines are referred to simulated brightnesses and black circles are the tomography data. In figure 6.9 the temperature profiles obtained are shown: red for the thin filter, blue for the thick one.

Temperature profiles in this last case are well superimposed, like in the previous. The difference between K_1 and K_2 is negligible confirming that line emissions are not recognizable in the range of energy defined by the filter thicknesses and giving a proof of the theoretical results obtained in the test reported in paragraph 2.3.

Concerning the brightnesses, blue curves are close to the experimental data assuring that the convergence has taken place, but a systematic error is visible: the shift between simulated and experimental data was expected since the using of a wrong topology reconstruction.

A third example is now reported, referred to shot 1060907059 at the instant 20ms. The arrangement of the lines of sight is equal to the one of the shot 1070829100

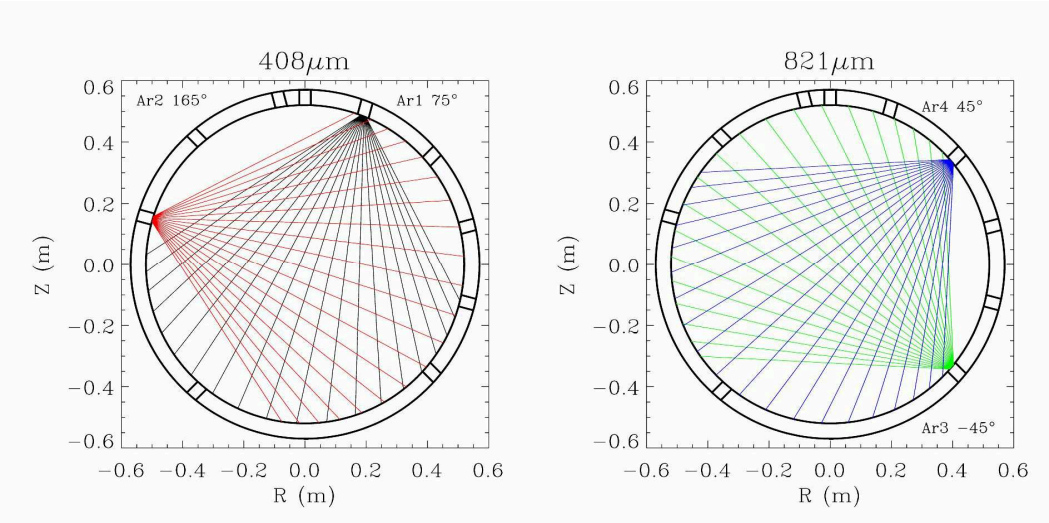

Figure 6.7: Lines of sight scheme for pulse 1090415018. Left panel: lines of sight for the probes 1 (black chords) and 2 (red chords). Right panel: lines of sight for the probes 3 (green chords) and 4 (blue chords).

for arrays 1 and 2 and to the shot 1090415018 for arrays 3 and 4.

Notice that also in this case the reconstruction of the coordinate ρ is not available and thus the plasma topology have to be estimated in a different way. We have substituted the reconstruction of the radial flux coordinate with a set of circles whose centers are gradually shifted from the camera to the plasma axis (the exterior circle is centered on the camera while the innermost circle is centered on the plasma axis). The contour of these *pseudo flux* coordinate is shown in figure 6.10(a). This description is justified by the fact that the poloidal rotation period of magnetic modes is much shorter than the brightness integration interval and thus the magnetic poloidal angle dependency structures should be unnoticed. The position of the plasma axis has been manually chosen with the SXR tomography reconstruction.

The enhancement factors obtained in this case are lower than the previous: $K_1 = 56.7$ and $K_2 = 54.2$. The temperature reconstructions obtained with the convergence are shown in figure 6.10 (blue and red curves),together with the TS profile [80] (orange dots). The two curves are well superimposed and have values compatible with the TS measurements, even though TS profile is very noisy.

The comparison between simulated and experimental brightnesses is reported in figure 6.11. Simulated brightnesses are close to the experimental one although, also in this case, a systematic error is still visible, especially for the arrays 3 and 4 (panel (b)). Like the previous example, such a systematic deviation is probably due to the wrong topology reconstruction.

In order to validate this technique several cases should be analyzed and compared to other profiles, the latter provided by different diagnostics. In fact, the reliability at the edge may be spoiled by the impurities concentration, which usu-

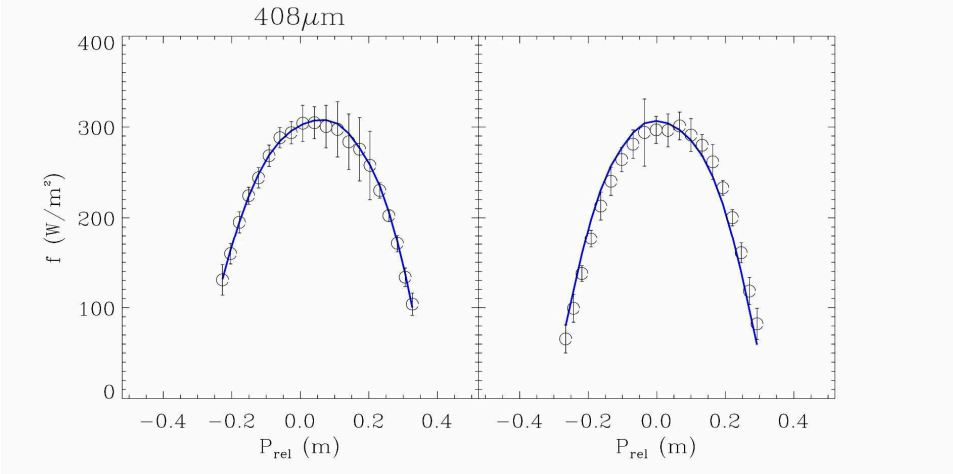

(a) tomography arrays 1 and 2

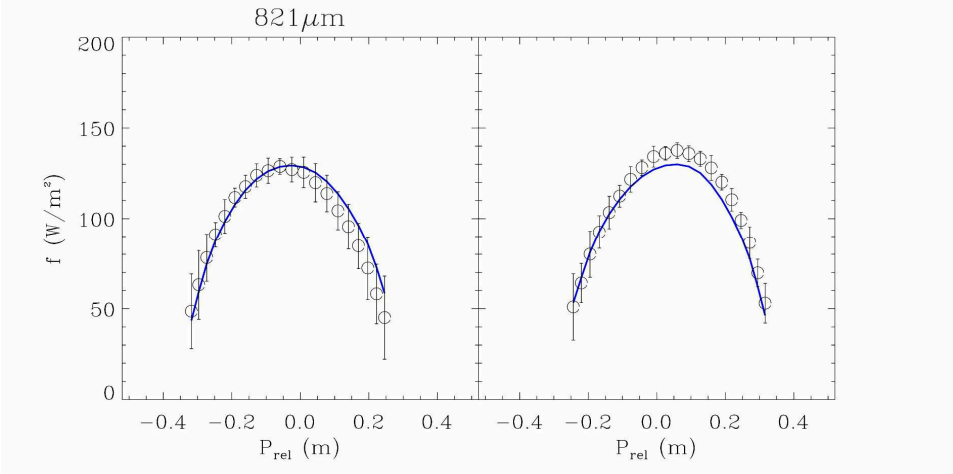

(b) tomography arrays 3 and 4

Figure 6.8: Algorithm for the estimation of the temperature profile applied to pulse 1090415018 at 20ms. Plots show the brightnesses obtained from the convergence on the temperature profile (blue line) compared to the experimental ones (black circles).

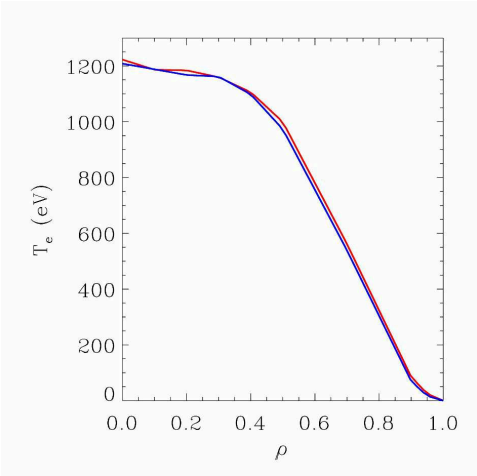

Figure 6.9: Algorithm for the estimation of the temperature profile, pulse 1090415018 at 20ms. This figure shows the two profile $T_e(\rho)$ obtained from the convergences on the two filters. Red curve identifies the 408μm filter while the blue one the 821μm filter.

ally grows (in magnitude and number of species) from the center to the edge. On the other hand, only few suitable cases were found and a specific campaign should be done.

6.3 The *two foil* simulation

This paragraph is devoted to describe the method, hereafter named *two foil simulation*, developed to obtain plasma temperature from the double color tomography data.

According to paragraph 6.1.1, two color tomography does not allow a reliable temperature estimation of the plasma. *Two foil simulation* represents an evolution of this technique and allows to estimate the plasma temperature with the same diagnostic device, but renouncing to the 2D temperature reconstruction.

The essential point of this method is to get the brightnesses from two different filters on every line of sight, so that the temperature can be estimated using the standard procedure adopted for the two foil diagnostic, as in DSXC and DSX3 in RFX-mod. Since all the lines of sight have just one filter thickness, the lacking brightnesses from the other filter must be simulated. Double color tomography reconstructs the emissivity of the plasma for two filter thicknesses and thus we can get such an estimation from the tomographic inversion with an analytical path integration. We can expect that the brightness estimation, which is an integration process, and the ratio between computed and experimental data will limit the oscillations discovered in the double color tomography.

The exact procedure used in the algorithm is the following:

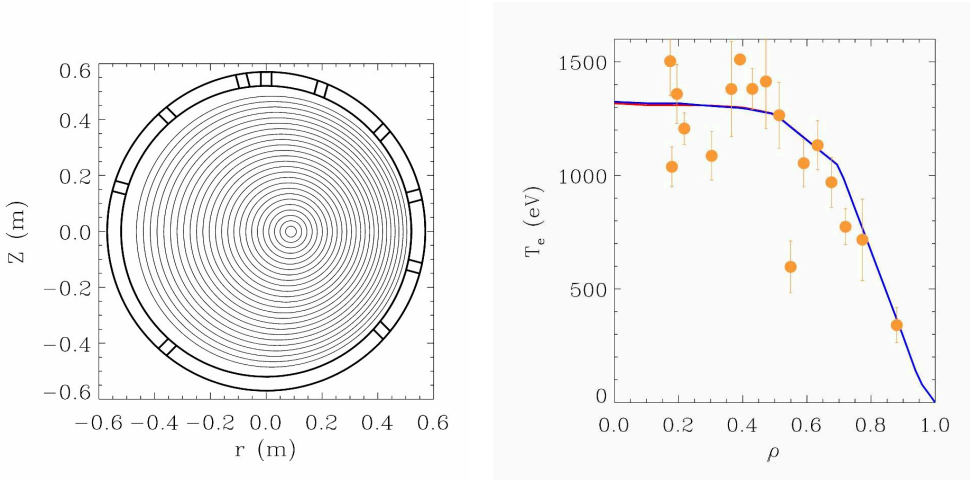

(a) (b)

Figure 6.10: (a) Contour of the pseudo radial flux coordinate. Such a coordinate is obtained tracing circles gradually shifted from the plasma center. (b) Algorithm for the estimation of the temperature profile, pulse 1060907059 at 20ms. the two profile $T_e(\rho)$ obtained from the convergences on the two filters are shown. Red curve is referred to the 303μm filter while the blue one to the 761μm filter. Also the TS temperature measurements are remapped and reported (orange points).

1. The first tomographic inversion is obtained from the data of the probes 1 and 2 (thin filter).

2. The second tomographic inversion is obtained from the data of the probes 3 and 4 (thick filter).

3. From the first inversion (thin filter) brightnesses on the lines of sight of the probes 3 and 4 are estimated (the integration process is analytical and exploits the parameters resulting from the inversion).

4. From the second inversion (thick filter) brightnesses on the lines of sight of the probes 1 and 2 are estimated.

5. 80+80 brightnesses are now available. For each line of sight the ratio $R = f_{thin}/f_{thick}$ is computed (experimental brightnesses are used together to the estimated one).

6. Finally, temperatures are estimated from the ratios R.

As a drawback, this method does not allow to directly locate the estimated temperature and thus another passage to remap them is required. Anyway, the remap-

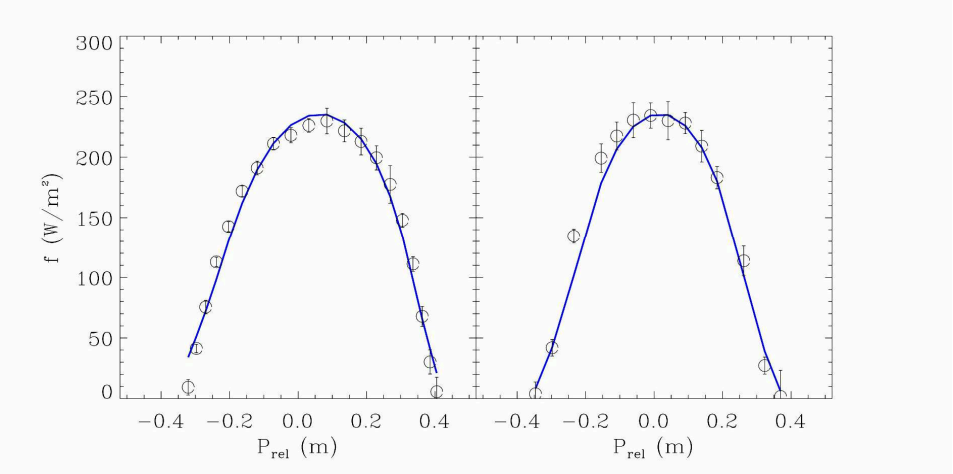

(a) tomography arrays 1 and 2

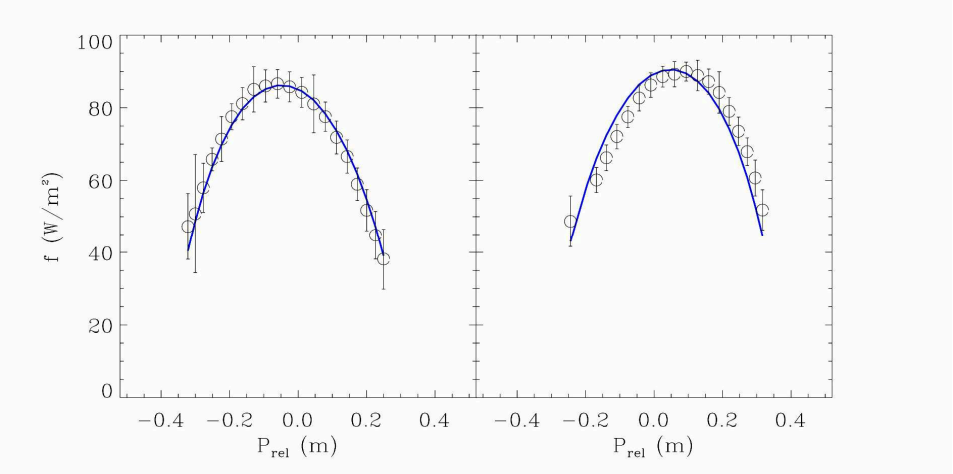

(b) tomography arrays 3 and 4

Figure 6.11: Algorithm for the estimation of the temperature profile applied to the pulse 1060907059 at 20ms. Plots show the brightnesses obtained from the convergence on the temperature profile (blue line) compared to the experimental ones (black circles).

ping method described in section 4.3 can be applied whenever a map of magnetic topology is available.

6.3.1. *Two foil* simulation results

In this paragraph some examples of temperature profiles obtained with the *two foil simulation* method are shown. Such profiles are then remapped in the helical flux coordinate. Moreover, at the end of the paragraph, an artificial case is discussed; the aim of this example is to determine the theoretical limits of this technique.

The first example presented is relative to the shot 1070829100 at 26ms. The obtained temperatures are plotted in figure 6.12 as a function of the impact parameter. According to paragraph 2.3, these four profiles describe the maximum temperatures visible from the four probes of tomography diagnostic. Notice that the profiles shown in figure 6.3, originated from the double color tomography, are collected at the same instant and they reproduce the sections passing through the center of the plasma and facing the four tomography probes. This permits a rough comparison with the profiles in figure 6.12: in this specific case the temperatures estimated with the new approach present smaller oscillations than those obtained with the two color tomography.

The magnetic topology of the plasma for this case is that of figure 6.6(a), and thus temperature profiles can be remapped with the method described in paragraph 4.3. The results of such an operation are shown in figure 6.13 in which the temperatures of the four arrays are shown as a function of the flux surface coordinate ρ. The plot shows that at small values of ρ the four arrays have similar T_e but from $\rho \sim 0.4$ the profiles spread out. Furthermore, over that value of ρ, temperatures drop toward 0eV revealing possible problems with their estimations.

Unfortunately at that time there was not a Thomson Scattering profile. In order to have a comparison between the TS and *two foils simulation* another shot has been chosen (shot 1060907059 at 20ms, this shot has the same filter thickness of the previous one). For this shot the flux surfaces reconstruction is not available, so, instead of the real radial flux coordinate, circles gradually shifted from the plasma center to the edge have been used. The contour of these pseudo flux coordinate is shown in figure 6.10(a). Figure 6.14 shows the temperature profiles mapped on the pseudo flux coordinate: the simulated two foils profiles are the colored lines (black identifies array 1, red array 2, green array 3 and blue array 4) while TS profile is shown with the orange dots. The simulated two foils temperatures are well mapped by the pseudo flux coordinate, even if some problems can be recognized at the edge, where the four profiles broaden out. This may be linked to the parameters used to build the pseudo flux coordinate map and thus it can be avoided with a more careful choice.

Concerning the TS profile there are evident oscillations that make the comparison quite difficult, anyway the T_e from the SXR data seems systematically lower

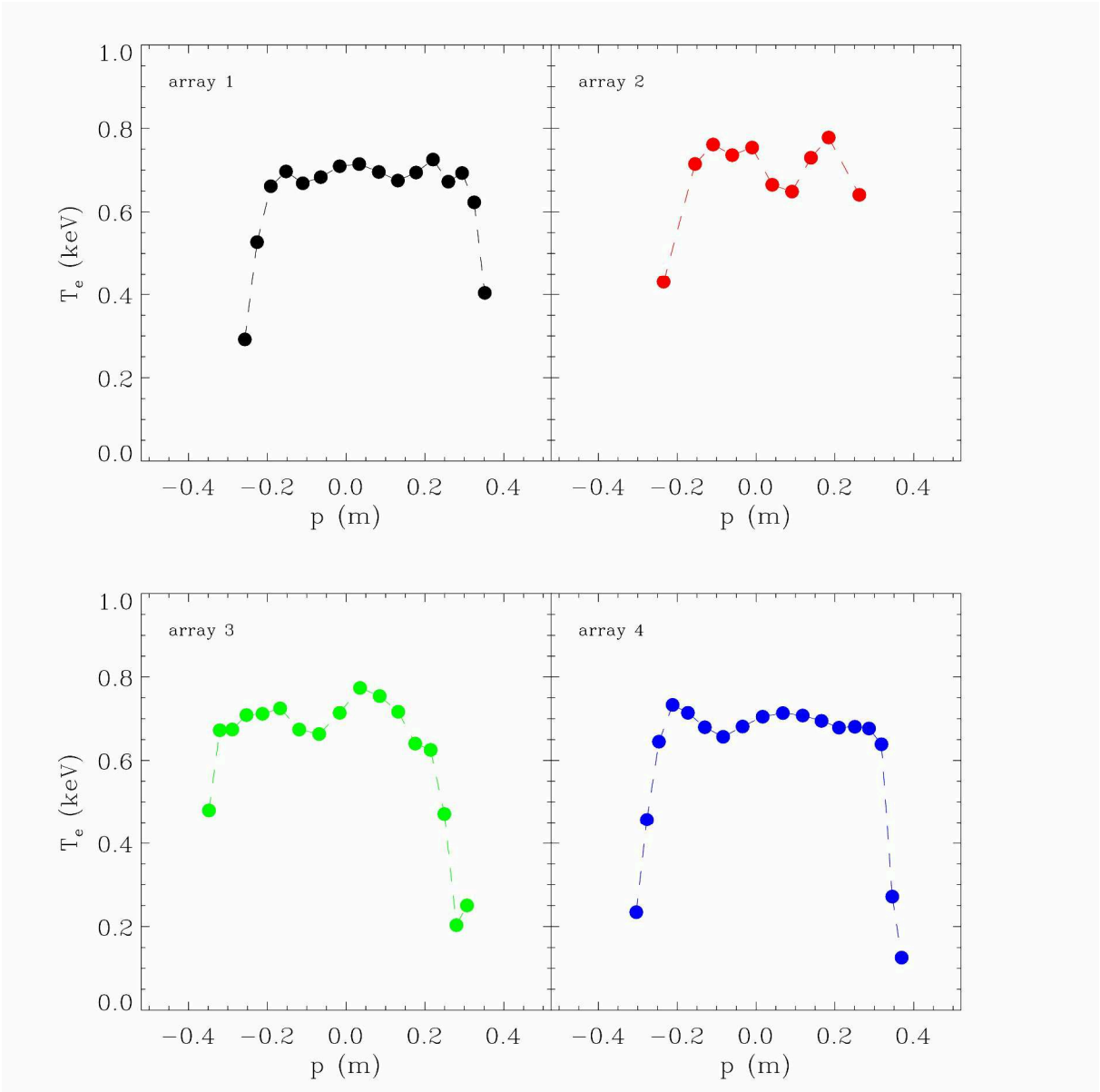

Figure 6.12: *Two foil simulation* applied at the shot 1070829100 at 26ms. Plots show the temperatures estimated with the *two foil simulation* as a function of the corresponding impact parameters. Colors identify the four probes: array 1 is in black, array 2 in red, array 3 in green and array 4 in blue.

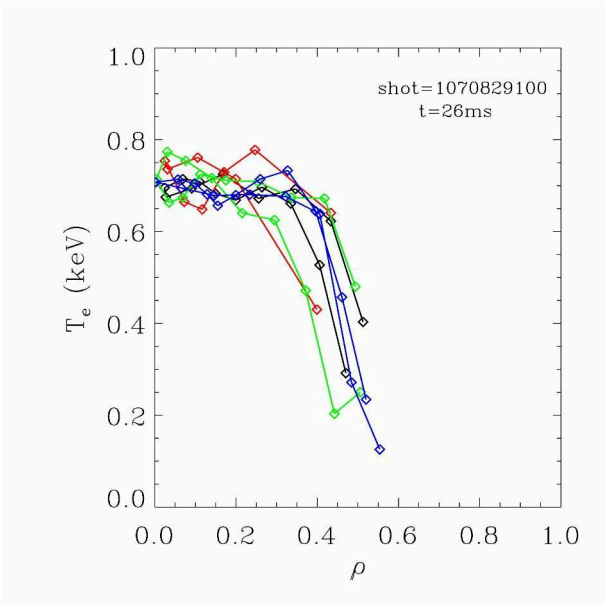

Figure 6.13: Temperature obtained with the *two foil simulation* remapped in ρ. All the four arrays are reported and can be identified by the colors (black array 1, red array 2, green array 3 and blue array 4).

than the Thomson temperature. It should been considered that the TS laser pulse last only a fraction of microsecond and thus it may be not exactly remapped by the pseudo flux coordinate map; the latter should be used only if integration time in data collection is longer than the structure rotation period (as discussed in paragraph 6.2).

From figure 6.14 another problem arises: some probes present temperature divergences on the edge sight lines. This unphysical estimation often affects also the temperature contour obtained by the double color tomography; it may be due to large oscillations of R (the ratio of the two emissivity or brightness) when the thick filter signal is comparable to the noise level.

To test capabilities and limits of the *two foil simulation* method all features of the plasma should be known. In fact the direct knowledge of temperature profile and plasma topology allows to check the accuracy of the reconstructed temperature profile provided by the *two foil simulation*. In the following analysis, the knowledge of the exact plasma condition relies on using a artificial set of data instead of the experimental ones. It includes density and temperature profiles and the topology of plasma: figure 6.15 shows the temperature profile, figure 6.10(a) the plasma topology while the density has been chosen to be constant on all of the poloidal section with value of $1 \cdot 10^{19} \mathrm{m}^{-3}$.

To simulate the SXR data collected by tomography, plasma emissivity on the entire poloidal section is computed with the bremsstrahlung approximation (see formula 4.10); then a numerical integration, along each line of sight (detailed ex-

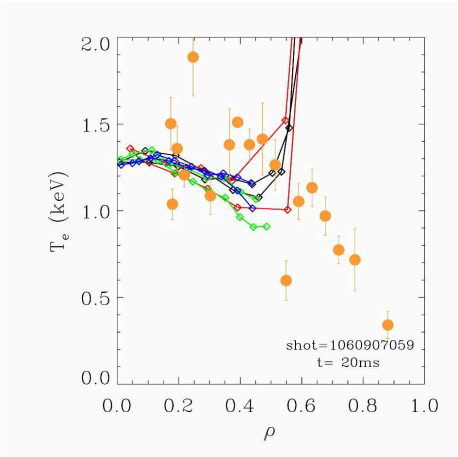

Figure 6.14: Plot of T_e mapped as function of ρ. Temperatures are estimated with the *two foil simulation* in shot 1060907059 at 20ms. Colors identifies the four probes (black probe 1, red probe 2, green probe 3 and blue probe 4). Orange dots are the temperatures obtained with Thomson Scattering.

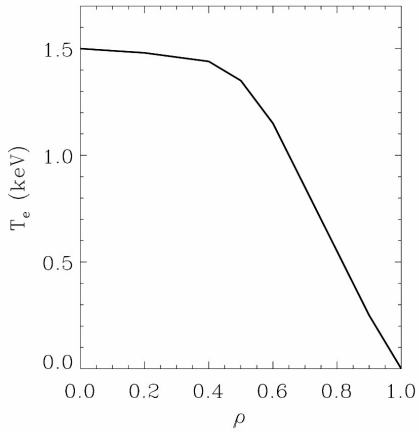

Figure 6.15: Test of the *two foil simulation* reliability. This plot shows the model temperature used to simulate the emissivity for both the filters thicknesses.

planation in paragraph 4.2.1), simulates the brightnesses.

The brightnesses captured with the tomography device from the plasma in such conditions are simulated using the numerical integration already used in paragraph 6.2. In the following analysis such brightnesses will be considered as real *experimental* data and thus the two foil simulation method will be applied in the same way.

The resulting temperatures, remapped on ρ, are shown in figure 6.16 together the starting temperature profile. The plot highlights some problems on the external lines of sight (high impact parameter): the higher the distance from the center, the higher the temperature oscillations about the theoretical value. Oscillations grow up to the divergence (at $\rho \sim 0.5$) on arrays 1 and 2. Consequently these errors are not originated by the noise of the data, as supposed in the example reported in 6.14, but they have the same origin of those met in the temperature contour obtained with the double color tomography, i.e. the bad matching of two emissivity inversions. Despite that, the new technique seems able to provide a reliable estimation of the core temperature.

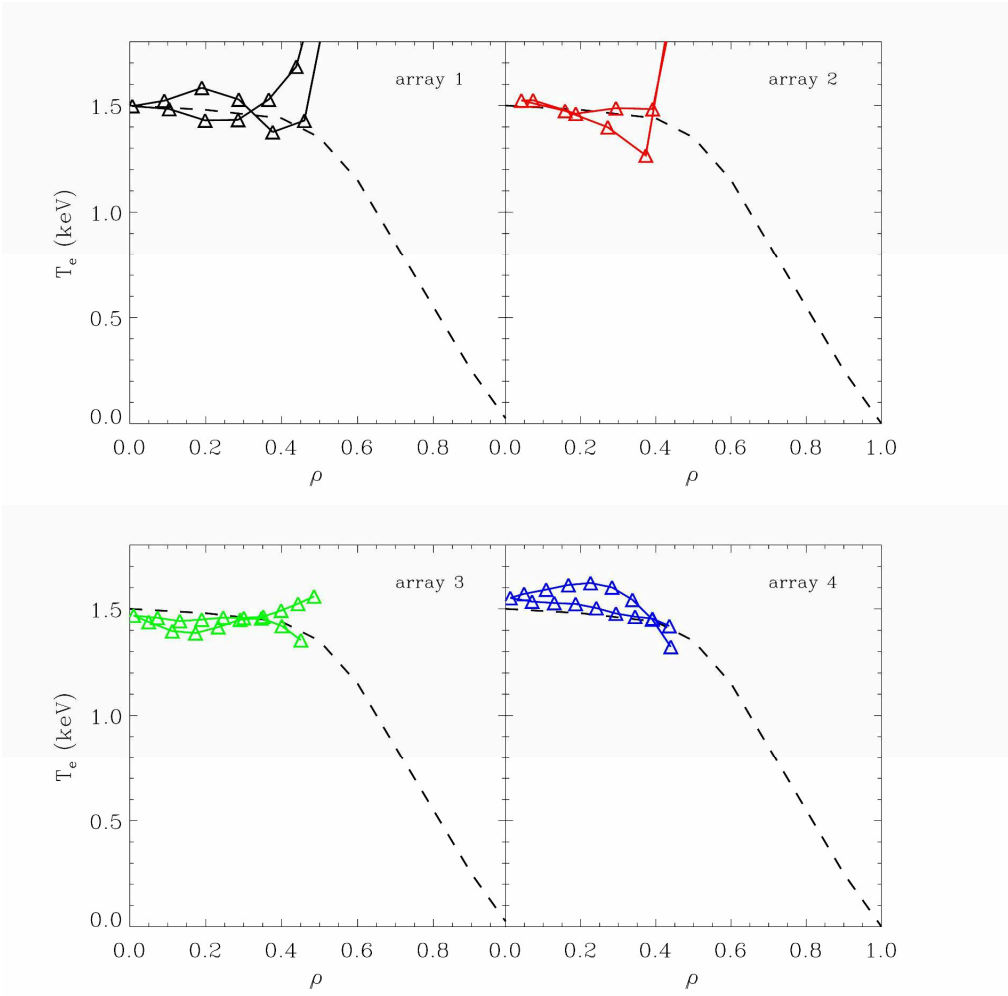

Figure 6.16: Test of the *two foil simulation* reliability. These plots show the estimation of temperatures performed with the *two foil simulation* for all the four probes (in clockwise order: array 1, 2, 4 and 3), temperature profiles are remapped in ρ. Dashed lines indicate the model temperature profile.

CHAPTER 7

Summary and conclusions

Nuclear fusion has been studied for a long time in various forms since it has been conceived as one of the most interesting alternatives to the traditional sources for electric energy generation. Currently, two concurrent ways to achieve the energy production by nuclear fusion are pursued. One is based on inertial confinement of pulsed and dense plasmas, the other exploits hot plasmas magnetically confined in continuous operations. Considering magnetic confined plasma, three families of experiments was selected during the years: tokamak, stellarator and RFP (all characterized by a toroidal plasma). At the present, the best performances are obtained with the tokamak configuration: this is why it has been selected for the fusion experiment ITER (International Thermonuclear Experimental Reactor), under construction in France. In addition, two alternative approaches are studied: the stellarator and the RFP. The first is motivated by its potential steady state capabilities, while the RFP is studied because of its intrinsic low applied field approach, which potentially makes its technology easier.

Concerning the RFP configuration the interest has risen when high plasma current operations have achieved the so-called QSH regimes (or helical regimes). These regimes involve new states in which the magnetic chaos, usually required for the discharge maintenance, results mitigated. The reduction of magnetic chaos is the most important requirement to prevent high energy losses and to reach reactor relevant performance. For this reason the characterization of helical states is of primary importance.

During my research activity I have studied for the first time the thermal dynamics features of such regimes. In order to obtain the necessary informations I have analyzed the data coming from the fast thermal diagnostics that are based on the soft x-ray detection. Such diagnostics derive the plasma emissivity (SXR tomography) or determine the highest temperature along a line of sight (diagnostic based on the two foil technique).

At the very beginning of my research activity I analyzed the data coming from a fan of lines of sight with two foil capability during the helical states; the aim was to

investigate the presence of temperature gradients in the core of the plasma column with a sufficiently high time resolution (see chapter 3). Within its limits (related to the simplified interpretation of the data and to the diagnostic resolution in time and space), the analysis showed that the scaling properties of transport were different from the theoretical expectations. In particular, the magnitude of the transport barrier was weakly correlated to the amplitudes of the secondary magnetic modes. Moreover a different behavior was noticed between the interval in which the dominant magnetic mode was rising from the one in which the dominant mode was still constant at a saturated level.

The most important part of my work is reported in chapter 4 where new methods for data analysis have been developed. These methods allowed to improve concerning the interpretation of SXR measurements in QSH regimes. In particular, a new algorithm for the tomography inversion has been developed, in addiction to another one for the interpretation of temperature profiles provided by two foil devices. The novelty is the integration between the thermal and the magnetic data.

The new tomographic method is based on the hypothesis that the topology of emissivity is strictly connected to the magnetic one, namely the plasma emissivity depends on the radial helical flux coordinate (ρ). Once the topology of the plasma is computed with the code called SHEq, a preliminary emissivity profile ($\epsilon(\rho)$) is used to simulate the diagnostic data. Thanks to an iterative process, the emissivity profile is modified to make simulated and experimental data converge.

The other algorithm reported in chapter 4 has been developped for a better understanding of temperature profiles coming from two foil diagnostics. Such a numerical procedure assumes that the electron temperature, detected from the diagnostic, is located on the flux surface tangential to the line of sight. This hypothesis is justified considering that T_e usually grows monotonically from the edge to the center of the plasma. Thanks to this remapping code, temperature profiles and hence gradient estimations are more precise and correctly interpreted.

The remapping method has been applied to experimental data in chapter 5. The results obtained can be summarized as:

- Strong differences have been recognized between phases in which the dominant mode is still rising (*rising* phases) and those in which dominant mode is saturated (*flattop* phases).

- *Rising* phases have values of ∇T_e higher than *flattop* ones.

- During the *rising* phase, dimensions of the region inside to the Internal Transport Barrier are correlated to the dominant magnetic mode, according to previous numerical simulation.

- The found experimental evidence of transitory nature of QSH regimes from the thermal point of view even during stationary QSH phases.

This thesis reports also my activity at MST (chapter 6). It was focused on the development and adaptation of analysis methods realized for RFX-mod diagnostics, to those in MST. In fact tomography devices, in MST and RFX-mod, have different features: MST tomography have two filter thicknesses (one in RFX-mod) and it can supply two tomographic inversions. For this reason, and because the experiment did not have two foil diagnostics for fast temperature sampling, the aim of the activity was changed, and the adapted algorithm was used to estimate the temperature profile rather than the emissivity one. Finally, another algorithm for MST diagnostics was developed. This procedure is called *two foil simulation* and it can be considered as an evolution of the *two color tomography*. The essential point of this method is to get brightnesses of two different filters on every line of sight of the existing SXR device, then temperature is estimated using the standard procedure adopted for two foil diagnostics. Since all the lines of sight of tomography have just one filter thickness, missing brightnesses are simulated a posteriori, from the tomographic inversion. *Two foil simulation* capabilities was tested: it resulted that, although external lines of sight could diverge, central temperature estimations were reliable enough.

Bibliography

[1] R. J. Goldston and P. H. Rutherford. *Introduction to Plasma Physics*. CRC Press, 1995.

[2] G. Spizzo. *Thermal Properties of Improved Confinement Regimes in RFX*. PhD thesis, 2000.

[3] F. F. Chen. *Introduction to Plasma Physics and Controlled Fusion*. Plenum Press, New York, 1984.

[4] R. Balescu. *Equilibrium and nonequilibrium statistical mechanics*. J. Wiley and sons, New York, 1975.

[5] J. Wesson. *Tokamaks*. Clarendon Press, Oxford, second edition, 1997.

[6] F. Troyon et al. *Plasma Phys. Control. Fusion*, 26(209), 1984. doi: 10.1088/0741-3335/26/1A/319.

[7] L.A. Artsimovich. Tokamak devices. *Nucl. Fusion*, 12(215), 1972. doi: 10.1088/0029-5515/12/2/012.

[8] J. D. Strachan et al. Deuterium and tritium experiments on tftr. *Plasma Phys. Control. Fusion*, 36(B3), 1994. doi: 10.1088/0741-3335/36/12B/001.

[9] L. Wegener. Status of wendelstein 7-x construction. *Fusion Engineering and Design*, 84(2-6):106 – 112, 2009. ISSN 0920-3796. doi: 10.1016/j.fusengdes.2009.01.106. URL http://www.sciencedirect.com/science/article/pii/S0920379609001264.

[10] B. Coppi, A. Airoldi, F. Bombarda, G. Cenacchi, P. Detragiache, and L.E. Sugiyama. Optimal regimes for ignition and the ignitor experiment. *Nuclear Fusion*, 41(9):1253, 2001. doi: 10.1088/0029-5515/41/9/314. URL http://stacks.iop.org/0029-5515/41/i=9/a=314.

[11] K. Miyamoto. *Plasma physics for nuclear fusion*. MIT press, 1989.

[12] A. Fassina. *Thermal transport characterization of RFP plasmas from electron temperature data*. PhD thesis, 2010.

[13] M. Gobbin. *Numerical study of magnetic topology and test particle transport in the Reversed Field Pinch and in the Tokamak*. PhD thesis, 2008.

[14] J. P. Freidberg. *Ideal magnetohydrodynamics*. Plenum Press, New York, NY, 1987.

[15] H. Grad and H. Rubin. Hydromagnetic equilibria and force-free fields. In *Proceedings of the Second United Nation International Conference on the Peaceful uses of Atomic Energy*, volume 31, page 190, 1958.

[16] V.D. Shafranov. On magnetohydrodynamical equilibrium configurations. *Soviet Phys. JETP*, 6:545, 1958.

[17] P. Piovesan. *Experimental MHD study of enhanced confinement Reversed Field Pinch Plasmas*. PhD thesis, 2004.

[18] J.W. Connor, T. Fukuda, X. Garbet, C. Gormezano, V. Mukhovatov, M. Wakatani, the ITB Database Group, the ITPA Topical Group on Transport, and Internal Barrier Physics. A review of internal transport barrier physics for steady-state operation of tokamaks. *Nuclear Fusion*, 44(4):R1, 2004. doi: 10.1088/0029-5515/44/4/R01. URL http://stacks.iop.org/0029-5515/44/i=4/a=R01.

[19] M. Kruskal and J. L. Tuck. The instability of a pinched fluid with a longitudinal magnetic field. *Proceedings of the Royal Society of London. Series A. Mathematical and Physical Sciences*, 245(1241):222–237, 1958. doi: 10.1098/rspa.1958.0079. URL http://rspa.royalsocietypublishing.org/content/245/1241/222.abstract.

[20] T. J. M. Boyd and J. J. Sanderson. *The physics of plasmas*. Cambridge university press, 2003.

[21] F. Bonomo. *Experimental Measurements of Soft X-Ray Emissivity Distribution and Electron Temperature Profile in Reversed Field Pinch Plasmas*. PhD thesis, 2008.

[22] T. M. Biewer, C. B. Forest, J. K. Anderson, G. Fiksel, B. Hudson, S. C. Prager, J. S. Sarff, J. C. Wright, D. L. Brower, W. X. Ding, and S. D. Terry. Electron heat transport measured in a stochastic magnetic field. *Phys. Rev. Lett.*, 91:045004, Jul 2003. doi: 10.1103/PhysRevLett.91.045004. URL http://link.aps.org/doi/10.1103/PhysRevLett.91.045004.

[23] S. Ortolani and D. D. Schnack. *The Magnetohydrodynamics of Plasma Relaxation*. World Scientific, 1993.

[24] A. B. Rechester and M. N. Rosenbluth. Electron heat transport in a tokamak with destroyed magnetic surfaces. *Phys. Rev. Letters*, 40(1), 1978.

[25] R. Fitzpatrick. Formation and locking of the "slinky mode" in reversed-field pinches. *Physics of plasmas*, 6(4), 1999.

[26] R. Fitzpatrick and P. Zanca. Phase-locking of tearing modes in the reversed field experiment. *Physics of Plasmas*, 9(6):2707–2724, 2002. doi: 10.1063/1.1481057. URL http://link.aip.org/link/?PHP/9/2707/1.

[27] V. Antoni, D. Merlin, S. Ortolani, and R. Paccagnella. Mhd stability analysis of force-free reversed field pinch configurations. *Nucl. Fusion*, 26(1711), 1986.

[28] J. B. Taylor. Relaxation of toroidal plasma and generation of reverse magnetic fields. *Phys. Rev. Lett.*, 33:1139–1141, Nov 1974. doi: 10.1103/PhysRevLett.33.1139. URL http://link.aps.org/doi/10.1103/PhysRevLett.33.1139.

[29] S. Cappello et al. *Nucl. Fusion*, 36(571), 1996. doi: 10.1088/0029-5515/36/5/I05. URL http://iopscience.iop.org/0029-5515/36/5/I05.

[30] S. Cappello et al. Equilibrium and transport for quasi-helical reversed field pinches. *Nuclear Fusion*, 51(103012), 2011.

[31] R. B. White et al. Hamiltonian guiding center drift orbit calculation for plasmas of arbitrary cross section. *Physics of Fluids*, 27(10):2455–2467, 1984. doi: 10.1063/1.864527. URL http://link.aip.org/link/?PFL/27/2455/1.

[32] R. Lorenzini et al. Self-organized helical equilibria as a new paradigm for ohmically heatd fusion plasmas. *Nature phys.*, 5(570), 2009.

[33] L. Frassinetti et al. Heat diffusivity model and temperature simulations in rfx-mod. *Nuclear Fusion*, 48(045007), 2008.

[34] S. R. Hudson and J. Breslau. Temperature contours and ghost surfaces for chaotic magnetic fields. *Phys. Rev. Lett.*, 100:095001, Mar 2008. doi: 10.1103/PhysRevLett.100.095001. URL http://link.aps.org/doi/10.1103/PhysRevLett.100.095001.

[35] W. Horton. Drift waves and transport. *Rev. Mod. Phys.*, 71:735–778, Apr 1999. doi: 10.1103/RevModPhys.71.735. URL http://link.aps.org/doi/10.1103/RevModPhys.71.735.

[36] S. C. Guo et al. *Phys. Plasmas*, 15(122510), 2008.

[37] B.B. Kadomtsev and O.P. Pogutse. Trapped particles in toroidal magnetic systems. *Nuclear Fusion*, 11(1):67, 1971. doi: 10.1088/0029-5515/11/1/010. URL http://stacks.iop.org/0029-5515/11/i=1/a=010.

[38] S. C. Guo, I. Predebon, and Z. R. Wang. Effect of trapped electrons on itg modes and occurrence of tem instabilities in rfp plasmas. In *37th EPS Conference on Plasma Physics*, volume 34, 2010.

[39] C. L. Chang, J. F. Drake, N. T. Gladd, and C. S. Liu. Unstable dissipative drift modes in a sheared magnetic field. *Physics of Fluids*, 23(10):1998–2006, 1980. doi: 10.1063/1.862876. URL http://link.aip.org/link/?PFL/23/1998/1.

[40] I. Predebon et al. *Phys. Rev. Lett.*, 105(195001), 2010.

[41] F. Sattin et al. Microturbolence studies in rfx-mod. *Journal of Physics*, 260 (012018), 2010.

[42] P. Innocente et al. Plasma performance and scaling laws in the rfx-mod reversed-field pinch experiment. *Nucl. Fusion*, 49(115022), 2009.

[43] G Rostagni. Rfx: an expected step in rfp research. *Fusion Engineering and Design*, 25(4):301 – 313, 1995. ISSN 0920-3796. doi: 10.1016/0920-3796(94)00362-B. URL http://www.sciencedirect.com/science/article/pii/092037969400362B.

[44] S. Martini et al. Active mhd control at high currents in rfx-mod. *Nucl. Fusion*, 47:783–791, 2007.

[45] L. Marrelli, P. Zanca, et al. Magnetic self organization, mhd active control and confinement in rfx-mod. *Plasma Phys. Control. Fusion*, 49.

[46] P. Franz et al. Soft x ray tomographic imaging in the rfx reversed field pinch. *Nucl. Fusion*, 41(695), 2001.

[47] A. M. Cormack. Representation of a function by its line integrals, with some radiological applications. *Journal of Applied Physics*, 34(9):2722–2727, 1963. doi: 10.1063/1.1729798. URL http://link.aip.org/link/?JAP/34/2722/1.

[48] A. M. Cormack. Representation of a function by its line integrals, with some radiological applications. ii. *Journal of Applied Physics*, 35(10):2908–2913, 1964. doi: 10.1063/1.1713127. URL http://link.aip.org/link/?JAP/35/2908/1.

[49] E. T. Jaynes. Information theory and statistical mechanics. *Phys. Rev.*, 106: 620–630, May 1957. doi: 10.1103/PhysRev.106.620. URL http://link.aps.org/doi/10.1103/PhysRev.106.620.

[50] E. T. Jaynes. Information theory and statistical mechanics. ii. *Phys. Rev.*, 108: 171–190, Oct 1957. doi: 10.1103/PhysRev.108.171. URL http://link.aps.org/doi/10.1103/PhysRev.108.171.

[51] L. Marrelli, P. Martin, A. Murari, and G. Spizzo. Total radiation losses and emissivity profiles in rfx. *Nucl. Fusion*, 38(649), 1998. doi: 10.1088/0029-5515/38/5/301. URL http://iopscience.iop.org/0029-5515/38/5/301.

[52] F. C. Jahoda, E. M. Little, W. E. Quinn, G. A. Sawyer, and T. F. Stratton. Continuum radiation in the x ray and visible regions from a magnetically compressed plasma (scylla). *Phys. Rev.*, 119:843–856, Aug 1960. doi: 10.1103/PhysRev.119.843. URL http://link.aps.org/doi/10.1103/PhysRev.119.843.

[53] J. Kiraly et al. Multichord time resolved electron temperature measurements by the x-ray absorber foil method on tftr. *Nuclear Fusion*, 27(3):397, 1987. URL http://stacks.iop.org/0029-5515/27/i=3/a=005.

[54] A. Murari, P. Franz, L. Zabeo, R. Bartiromo, L. Carraro, G. Gadani, L. Marrelli, P. Martin, R. Pasqualotto, and M. Valisa. An optimized multifoil soft x-ray spectrometer for the determination of the electron temperature with high time resolution. *Review of Scientific Instruments*, 70(1):581–585, 1999. doi: 10.1063/1.1149342. URL http://link.aip.org/link/?RSI/70/581/1.

[55] F. Bonomo, P. Franz, A. Murari, G. Gadani, A. Alfier, and R. Pasqualotto. A multichord soft x-ray diagnostic for electron temperature profile measurements in rfx-mod. *Review of Scientific Instruments*, 77(10):10F313, 2006. doi: 10.1063/1.2219400. URL http://link.aip.org/link/?RSI/77/10F313/1.

[56] I. H. Hutchinson. *Principles of plasma diagnostics*. Cambridge University Press, first edition, 1987. p. 160.

[57] R. D. Gill et al. Soft x-ray measurements of the impurity density in dite. *Nucl. Fusion 19 1003*, 19(1003), 1979. doi: 10.1088/0029-5515/19/8/001. URL http://iopscience.iop.org/0029-5515/19/8/001.

[58] M Bagatin, A Buffa, et al. Rfx diagnostics. *Fusion Engineering and Design*, 25(4):425 – 460, 1995. ISSN 0920-3796. doi: 10.1016/0920-3796(94)00283-D. URL http://www.sciencedirect.com/science/article/pii/092037969400283D.

[59] P. Piovesan, M. Zuin, et al. Magnetic order and confinement improvement in high-current regimes of rfx-mod with mhd feedback control. *Nuclear Fusion*, 49(085036), 2009.

[60] P. Martin et al. Overview of rfx-mod results. *Nuclear Fusion*, 49(10):104019, 2009. URL http://stacks.iop.org/0029-5515/49/i=10/a=104019.

[61] L. Carraro et al. Improved confinement with internal electron transport barriers in rfx-mod. *Nuclear Fusion*, 49(055009), 2009.

[62] F. D'angelo and R. Paccagnella. *Phys. Plasmas*, 3, 1996. p. 118.

[63] B. Momo et al. Magnetic coordinate systems for helical shax states in reverse field pinch plasmas. *Plasma Phys. Control. Fusion*, 53(125004), 2011. doi: 10.1088/0741-3335/53/12/125004.

[64] W. D. D'haeseleer, W. N. G. Hitchon, W. I. van Rij, S. P. Hirshman, and J. L. Shohet. *Flux Co-ordinates and Magnetic Field Structure*. Springer, New York, 1991.

[65] M. E. Puiatti, M. Valisa, et al. Internal and external electron transport barriers in the tfx-mod reversed field pich. *Nuclear Fusion*, 51(073038), 2011.

[66] M. Gobbin et al. Vanishing magnetic shear and electron transport barriers in the rfx-mod reversed field pinch. *Phys. Rev. Lett.*, 106:025001, 2011.

[67] A. Fassina, P. Franz, et al. Electron temperature features of rfp dax states. In *53rd Annual Meeting of the APS Division of Plasma Physics*, volume 56. Bulletin of the American Physical Society, 2011. URL http://meetings.aps.org/link/BAPS.2011.DPP.PO4.14.

[68] X. Garbet et al. Profile stiffness and global confinement. *Plasma Phys. And Control. Fusion*, 46(1351), 2004. URL http://iopscience.iop.org/0741-3335/46/9/002/.

[69] B. A. Carreras et al. On the use of critical gradient models in fusion plasma transport studies. *Phys. Plasmas*, 13(062301), 2006.

[70] I. Predebon et al. On the mutual effect of ion temperature gradient instabilities and impurity peaking in the reversed field pinch. *Plasma Phys. Control. Fusion*, 53(125009), 2011.

[71] P. Scarin, N. Vianello, et al. Topology and transport in the edge region of rfx-mod helical regimes. *Nucl. Fusion*, 51(073002), 2011.

[72] S. C. Prager et al. Overview of results in the mst reversed field pinch experiment. *Nuclear Fusion*, 45(S276), 2005.

[73] J. S. Sarff, S. A. Hokin, H. Ji, S. C. Prager, and C. R. Sovinec. Fluctuation and transport reduction in a reversed field pinch by inductive poloidal current drive. *Phys. Rev. Lett.*, 72:3670–3673, Jun 1994. doi: 10.1103/PhysRevLett.72.3670. URL http://link.aps.org/doi/10.1103/PhysRevLett.72.3670.

[74] B. E. Chapman et al. Reduced edge instability and improved confinement in the mst reversed-field pinch. *Phys. Rev. Lett.*, 87:205001, Oct 2001. doi: 10.1103/PhysRevLett.87.205001. URL http://link.aps.org/doi/10.1103/PhysRevLett.87.205001.

[75] P. Franz, L. Marrelli, P. Piovesan, et al. Observations of multiple magnetic islands in the core of a reversed field pinch. *Phys. Rev. Lett.*, 92:125001, Mar 2004. doi: 10.1103/PhysRevLett.92.125001. URL http://link.aps.org/doi/10.1103/PhysRevLett.92.125001.

[76] P. Franz, L. Marrelli, P. Piovesan, I. Predebon, et al. Tomographic imaging of resistive mode dynamics in the madison symmetric torus reversed-field pinch. *Physics of Plasmas*, 13(1):012510, 2006. doi: 10.1063/1.2160519. URL http://link.aip.org/link/?PHP/13/012510/1.

[77] J. T. Chapman. *Spectroscopic measurement of the MHD dynamo in the MST Reversed Field Pinch*. PhD thesis, 1998.

[78] F. Auriemma, P. Zanca, et al. Magnetic reconstruction of nonaxisymmetric quasi-single-helicity configurations in the madison symmetric torus. *Plasma Phys. Control. Fusion*, 53(105006), 2011.

[79] P. Franz et al. Two-dimensional time resolved measurements of the electron temperature in mst. *Review of Sci. Instruments*, 77(10F318), 2006.

[80] J. A. Reusch, M. T. Borchardt, D. J. Den Hartog, A. F. Falkowski, D. J. Holly, R. O'Connell, and H. D. Stephens. Multipoint thomson scattering diagnostic for the madison symmetric torus reversed-field pinch. *Review of Scientific Instruments*, 79(10):10E733, 2008. doi: 10.1063/1.2956742. URL http://link.aip.org/link/?RSI/79/10E733/1.